Cell

Global genetic interaction network of a human cell maps conserved principles and informs functional interpretation of gene co-essentiality profiles

Graphical abstract

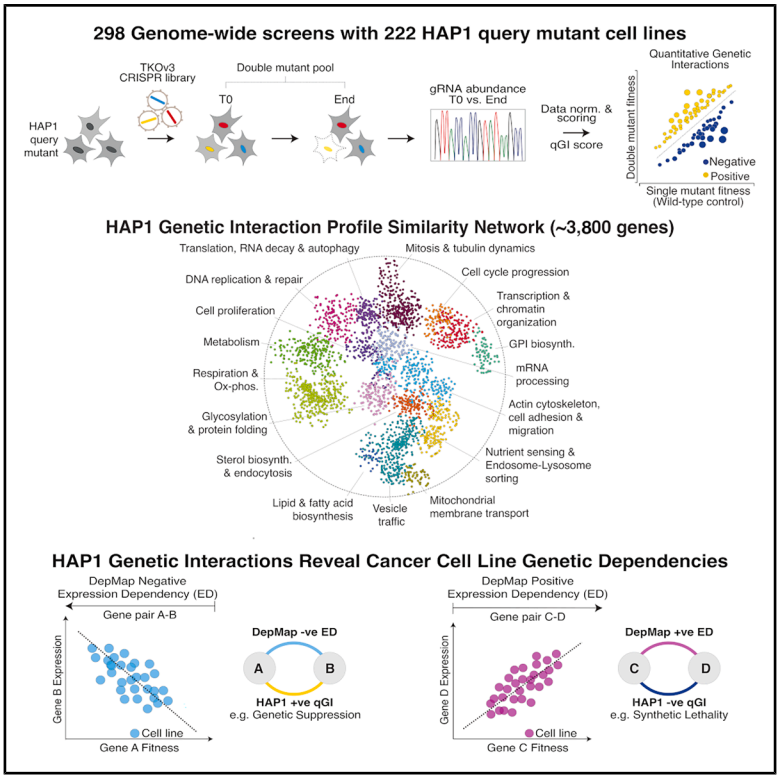

Highlights

- Genetic network maps ~89,000 interactions among ~4 million gene pairs in HAP1 human cells
- HAP1 genetic network reveals functional relationships among ~3,800 human genes
- Genetic network structure and topology are conserved from yeast to human cells
- Genetic interactions aid in the interpretation of DepMap cancer cell genetic dependencies

Authors

Maximilian Billmann, Michael Costanzo, Xiang Zhang, ..., Chad L. Myers, Jason Moffat, Charles Boone

Correspondence

brenda.andrews@utoronto.ca (B.A.), chadm@umn.edu (C.L.M.), jason.moffat@sickkids.ca (J.M.), charlie.boone@utoronto.ca (C.B.)

In brief

CRISPR perturbation of ~4 million gene pairs in human HAP1 cells maps ~89,000 genetic interactions, revealing a hierarchical network that links genes to complexes, pathways, and cellular processes and elucidates the genes underlying cancer cell genetic dependencies.

Billmann et al., 2026, Cell *189*, 1–24
June 11, 2026
https://doi.org/10.1016/j.cell.2026.03.044

CellPress

Please cite this article in press as: Billmann et al., Global genetic interaction network of a human cell maps conserved principles and informs functional interpretation of gene co-essentiality profiles, Cell (2026), https://doi.org/10.1016/j.cell.2026.03.044

Cell

CellPress
OPEN ACCESS

Article

Global genetic interaction network of a human cell maps conserved principles and informs functional interpretation of gene co-essentiality profiles

Maximilian Billmann,[1,2,22] Michael Costanzo,[3,22] Xiang Zhang,[1,22] Arshia Z. Hassan,[1,22] Mahfuzur Rahman,[1,22] Kevin R. Brown,[4,22] Katherine S. Chan,[4] Amy Hin Yan Tong,[3] Carles Pons,[5] Henry N. Ward,[1,6] Catherine Ross,[3] Jolanda van Leeuwen,[3] Michael Aregger,[3] Keith A. Lawson,[3,9] Barbara Mair,[3] Amy F. Roth,[7] Nesli E. Sen,[8] Duncan T. Forster,[3,9] Guihong Tan,[3] Patricia Mero,[4] Sanna N. Masud,[3,4,9] Yoonkyu Lee,[1,6] Magali Aguilera-Uribe,[4,9] Matej Ušaj,[3] Sylvia M.T. Almeida,[3,9] Kamaldeep Aulakh,[4] Urvi Bhojoo,[3,9] Saba Birkadze,[4,9] Nathaniel Budijono,[1] Xunhui Cai,[10] Joseph J. Caumanns,[3] Jordan J. Chalmers,[4,9] Megha Chandrashekhar,[3,9] Daniel Chang,[1] Ryan Climie,[3] Kuheli Dasgupta,[4,9] Adrian Drazic,[3,11] Jose I. Rojas Echenique,[3] Rafael Gacesa,[3] Adrian Granda Farias,[4,9] Andrea Habsid,[4]

(Author list continued on next page)

[1]Department of Computer Science and Engineering, University of Minnesota, Minneapolis, MN, USA
[2]Institute of Human Genetics, School of Medicine and University Hospital Bonn, University of Bonn, Bonn, Germany
[3]Donnelly Centre, University of Toronto, Toronto, ON, Canada
[4]Program in Genetics and Genome Biology, The Hospital for Sick Children, Toronto, ON, Canada
[5]Institute for Research in Biomedicine (IRB Barcelona), The Barcelona Institute for Science and Technology, Barcelona, Spain
[6]Graduate Program in Bioinformatics and Computational Biology (BICB), University of Minnesota, Minneapolis, MN, USA
[7]Department of Pharmacology, Wayne State University School of Medicine, Detroit, MI, USA
[8]Department of Molecular and Cellular Biology, University of Geneva, Geneva, Switzerland
[9]Department of Molecular Genetics, University of Toronto, Toronto, ON, Canada
[10]Institute of Pathology, Tongji Hospital, Tongji Medical College, Huazhong University of Science and Technology, Wuhan, China
[11]Department of Biomedicine, University of Bergen, Bergen, Norway
[12]Department of Surgery, McGill University, Cancer Research Program, Research Institute of McGill University Health Centre, Montreal, QC, Canada
[13]Institute for Biomedical Engineering, University of Toronto, Toronto, ON, Canada
[14]Department of Biochemistry, University of Toronto, Toronto, ON, Canada
[15]Department of Chemistry, The Scripps Research Institute, La Jolla, CA, USA
[16]Department of Biology, Stanford University, Stanford, CA, USA
[17]Department of Computational and Systems Biology, University of Pittsburgh School of Medicine, Pittsburgh, PA, USA

(Affiliations continued on next page)

SUMMARY

Deciphering how genes interact within human cells is essential for understanding their functional wiring and for developing targeted therapeutic strategies. In this study, we present a genome-scale map of genetic interactions in the human haploid cell line HAP1, based on CRISPR-based perturbation of ~4 million gene pairs. The resulting network comprises ~89,000 high-confidence gene-gene interactions, organizing genes into hierarchical modules corresponding to protein complexes and pathways, biological processes, and cellular compartments, mirroring principles observed in yeast and highlighting the functional architecture of a human cell. This large-scale genetic network complements the DepMap gene co-essentiality network by capturing unique functional information, uncovering roles of previously uncharacterized genes, and identifying molecular determinants of cancer-cell-line-specific genetic dependencies. This study presents a general data-driven strategy for systematically exploring the roles of genes and their functional connections in human cell lines.

INTRODUCTION

Genetic interactions identify functional connections between specific genes and their genetic modifiers, which impact the genotype-to-phenotype relationship.[1] Understanding the general principles of genetic networks in cells and organisms is critical for advancing precision medicine, as these networks influence disease manifestation by determining both its severity

CellPress
OPEN ACCESS

Cell
Article

Ira Horecka,[3,9] Kristin Kantautas,[3,9] Fenghu Ji,[10] Dae-Kyum Kim,[3,12] Seon Yong Lee,[4] Wendy Liang,[3] Hyobin Julianne Lim,[3,9] Kevin Lin,[1,6] Xueyibing Lu,[1] Michael Maier,[21] Babak Nami,[4] Allison Nixon,[3,9] Nicholas Mikolajewicz,[4] Milad Mokhtaridoost,[4] Lyudmila Nedyalkova,[3] Thomas Rohde,[2] Maria Sartori Rodrigues,[3] Martin Soste,[3] Eric Schultz,[1] Wen Wang,[1] Ashwin Seetharaman,[3] Ermira Shuteriqi,[3] Olga Sizova,[4] David Thomson Taylor,[4,13] Maria Tereshchenko,[14] David Tieu,[3,9] Jacob Turowec,[3] Tajinder Ubhi,[3,14] Sylvia Varland,[3,11] Kyle E. Wang,[3,9] Zi Yang Wang,[3,9] Jiarun Wei,[4,9] Yu-Xi Xiao,[4,9] Philipp G. Maass,[4,9] Bruno Reversade,[21] Grant W. Brown,[3,14] Benjamin F. Cravatt,[15] Scott J. Dixon,[16] Haley D.M. Wyatt,[14] Hannes L. Röst,[3] Frederick P. Roth,[3,17] Tian Xia,[18] Gary D. Bader,[3,9] Robbie Loewith,[8] Nicholas G. Davis,[7] Brenda Andrews,[3,9,*] Chad L. Myers,[1,6,*] Jason Moffat,[4,9,13,*] and Charles Boone[3,9,19,20,23,*]

[18]School of Software Engineering, Huazhong University of Science and Technology, Wuhan, China
[19]RIKEN Center for Sustainable Resource Science, Wako, Saitama 351-0198, Japan
[20]Canadian Institute for Advanced Research (CIFAR), Toronto, ON, Canada
[21]Genome Institute of Singapore (GIS), Agency for Science, Technology and Research (A*STAR), Singapore, Singapore
[22]These authors contributed equally
[23]Lead contact
*Correspondence: brenda.andrews@utoronto.ca (B.A.), chadm@umn.edu (C.L.M.), jason.moffat@sickkids.ca (J.M.), charlie.boone@utoronto.ca (C.B.)
https://doi.org/10.1016/j.cell.2026.03.044

(expressivity) and likelihood of occurrence (penetrance). Moreover, genetic interactions provide opportunities to uncover novel therapeutic strategies, including target identification for synthetic lethal cancer treatments or druggable suppressors of disease genes and their pathways.[1]

Negative genetic interactions, such as synthetic lethal or sick interactions, occur when a double mutant shows a fitness defect greater than the expected effect of the combined single mutants. Positive genetic interactions, including suppression interactions, are scored in double mutants that grow better than expected.[1] Systematic analysis in the budding yeast, *Saccharomyces cerevisiae*, mapped a global network of ~1,000,000 gene-gene interactions among its set of ~1,000 essential and ~5,000 nonessential genes.[2–5] Yeast genetic interactions connect functionally related genes, and network analysis of genetic interaction profile similarities clusters genes into an organized hierarchy of modules of increasing size corresponding to protein complexes or pathways, biological processes, and cellular compartments. The resultant global genetic interaction profile similarity network reveals the functional architecture of a cell.[5]

Genome-wide pooled CRISPR-knockout (KO) and gene trap mutagenesis screens have defined a core set of essential genes required for the proliferation of most human cell lines, as well as selectively essential genes that support the growth of specific cancer cell lines.[6–14] This forms the basis of gene-cell line networks, such as the Cancer Dependency Map (DepMap: depmap.org/portal),[10] which systematically identifies cancer cell-specific genetic vulnerabilities. Selectively essential genes are particularly relevant to our understanding of genetic interactions because their essential roles may depend on genome variation within a specific genetic background, potentially revealing synthetic lethal interactions that can be exploited for therapeutic intervention.[15–18] However, the genetic mechanisms underlying these dependencies are mostly unknown and are likely complex, involving multiple variants and other cell-line-specific factors.[1,19–21] Constructing a genetic interaction network in an isogenic cell line can help bridge this knowledge gap by identifying dependencies between specific pairs of genes.

The DepMap gene-cell line network can also be transformed into a gene-gene co-essentiality network, which connects gene pairs that are essential in overlapping subsets of cancer cell lines. Like the global yeast genetic interaction profile similarity,[5] the DepMap co-essentiality network provides a particularly powerful resource for inferring gene function.[22–26]

In addition to single gene perturbation analyses, combinatorial RNAi and CRISPR screens based on multiplexing short hairpin RNAs (shRNAs) and guide RNAs (gRNAs), respectively, have identified genetic interactions among subsets of human genes in a single cell line.[27–40] CRISPR interference (CRISPRi) generates knockdown phenotypes and has been applied on a large scale to map genetic interactions among thousands of gene pairs.[41,42] Similar methods promise to expand the scale and efficiency of genetic interaction screens in human cells.[34,43] Complementary approaches used genome-wide CRISPR-KO or gene trap mutagenesis methods to introduce secondary KO mutations into engineered cell lines, each carrying a stable "query" mutation of interest.[6,44–47] Collectively, these studies, along with the yeast genetic network, suggest that a genome-scale genetic network mapped in a single cell line should organize a large fraction of human genes into functional modules to map the functional architecture of a human cell.

Here, we report analysis of ~4,000,000 gene pairs to construct a genetic network consisting of 88,933 genetic interactions in the human haploid cell line, HAP1. Like the global yeast genetic interaction profile similarity network, the corresponding HAP1 network organizes human genes into hierarchical structured subsets of functional modules and provides a data-driven representation of human cell function that complements the DepMap co-essentiality network, revealing roles for previously uncharacterized genes and molecular factors underlying specific cancer cell line genetic dependencies. From a systematic comparative analysis, we conclude that the general principles and topology of genetic networks are conserved from yeast to human cells.

RESULTS

Genome-scale genetic interaction analysis in human HAP1 cells

To systematically map a reference human cell genetic network, we selected HAP1 as a model cell line because it lacks

aneuploidies and is amenable to loss-of-function (LOF) genetic screens.[6,45,46,48–50] Quantitative genetic interaction (qGI) analysis requires accurate single-mutant fitness phenotypes, which we generated by performing 39 genome-wide, pooled CRISPR-Cas9 KO screens with the Toronto KnockOut version 3 (TKOv3) gRNA library in HAP1 wild-type (WT) cells (Figure S1; Data S1 and S2; Document S1).[7,51] In total, we measured single mutant fitness for ~17,800 genes in two growth conditions and identified 1,524 genes (~15% of expressed genes) that were essential for HAP1 cell proliferation. The majority of HAP1 essential genes are core essential genes (Figure S2; Data S2; Document S1).[6–8,10] Consequently, they are required for the viability of most human cell lines and exhibit physiological and evolutionary properties commonly associated with essential genes identified in other human cell lines and model organisms (Figures S1 and S2; Data S2 and S3; Document S1).[6,7,52–56]

To quantify genetic interactions, we developed a qGI score that compares the abundance of TKOv3 gRNA barcodes (i.e., genomically integrated gRNA expression cassettes) in screens using HAP1 WT cells compared with congenic query mutant cells that carried a stable mutation in a gene of interest (Figure S3A).[45,46,52] gRNA barcode abundance in a query mutant cell line provides an estimate of double-mutant fitness (Figure S3A). Negative interactions identify genes with gRNA barcodes that show significantly decreased barcode abundance in a query mutant relative to WT, whereas positive interactions reflect genes with increased gRNA barcode abundance in a query mutant relative to WT (Figures S3A and S3B). We focused on functionally diverse genes that showed a range of gene expression levels and single mutant fitness defects in HAP1 cells (Figure S4) and constructed 222 query gene mutant cell lines, most of which carried a confirmed complete LOF allele. These query cell lines were used in 298 genome-wide CRISPR screens to score genetic interactions among 3,934,506 unique gene pairs (Data S1, S2, and S4).

Assessing qGI score quality

We performed several analyses to ensure reproducibility of our genetic interaction measurements.

(1) Seven different query genes were each screened 4–5 times and analyzed using a Markov chain Monte Carlo (MCMC) estimation approach[57] to estimate false negative and positive rates over a wide range of qGI score and false discovery rate (FDR) significance thresholds, which enable customized filtering of the complete dataset (Figure S5A; Data S5; Document S1).[52]

(2) Because specific query gene mutant alleles have the potential to influence genetic interaction profiles, we examined the robustness of our platform by performing independent replicates using the same query cell lines, allowing for accurate evaluation of our qGI scoring method, while also controlling for batch and experimental artifacts. In total, independent replicate screens were performed for 50 query genes (n = 2–5 screens/query cell line) (Figures S5B and S5C; Data S1), each using a different batch of a lentiviral pooled TKOv3 CRISPR library prepared over the course of the project, which translated to qGI scores for ~766,000 independent replicate gene pairs (Figures S3C, S5B, and S5C). qGI scores were reproducible, with the strongest correlation observed for query genes that showed higher numbers of genetic interactions (Figures S3C and S5C; Document S1). Importantly, replicate correlation increased substantially when comparisons were focused on genetic interactions that satisfied our defined qGI score and FDR significance thresholds, highlighting the effectiveness of our scoring method to identify high-confidence interactions (Figure S5C). Moreover, for a subset of query genes, we also performed screens using different clones (Figure S5D). While replicate correlation tended to be higher for screens performed using the same clone, we found that different LOF mutations in the same query gene (i.e., different clones) often generated overlapping genetic interaction profiles (Figure S5D). In addition, we examined replicate interactions in both rich and minimal medium and found that they were also highly correlated (Figure S5E), indicating that, like in yeast,[57] HAP1 genetic interactions were generally robust to environmental differences.

(3) Despite independent construction of query and library mutant alleles, we also observed agreement among reciprocal gene pairs (i.e., query A-library B versus query B-library A) (Figure S5F).

(4) As a consequence of our screening approach, a subset of positive interactions involved apparent "self" interactions, where a library gene was targeted in a query cell line already harboring a mutation in that same gene (Figure S5G). These cases are expected to score as positive interactions because additional CRISPR-mediated perturbation should not exacerbate the fitness defect of the query mutant cell line. This indicates that the cell line already carries a complete LOF allele of the targeted query gene, such that further disruption does not produce an additional fitness effect. The strength of positive self-interaction was inversely correlated with single mutant fitness, which is consistent with the expectation that further disruption of a fully inactivated gene has no additional impact (Figure S5G). This pattern supports the integrity of our HAP1 query mutant cell lines because ~94% of query genes (209/222) showed expected self-interactions. A minor subset of query genes (~6%, 13/222) exhibited unexpected self-interactions, suggesting that they carry partial LOF query gene alleles (Figure S5G).[58]

(5) Interactions for 5 query genes were recapitulated using an independent and nonoverlapping gRNA library, demonstrating that qGI scores were not driven by gRNA-specific phenotypes (Figure S5H; Data S6).

(6) We benchmarked negative interactions for the *PTAR1* query gene to those previously identified in a HAP1 retroviral gene trap-based screen (Figure S6; Data S7)[6] and found ~68% (40/59, $p < 7 \times 10^{-59}$, hypergeometric test) of previously reported interactions were also identified by our CRISPR screen (Figure S6A; Data S7).[6] *PTAR1* encodes a geranylgeranyl transferase (GGTase-III) that modifies and activates the Soluble NSF attachment protein receptor (SNARE) protein YKT6, which

Please cite this article in press as: Billmann et al., Global genetic interaction network of a human cell maps conserved principles and informs functional interpretation of gene co-essentiality profiles, Cell (2026), https://doi.org/10.1016/j.cell.2026.03.044

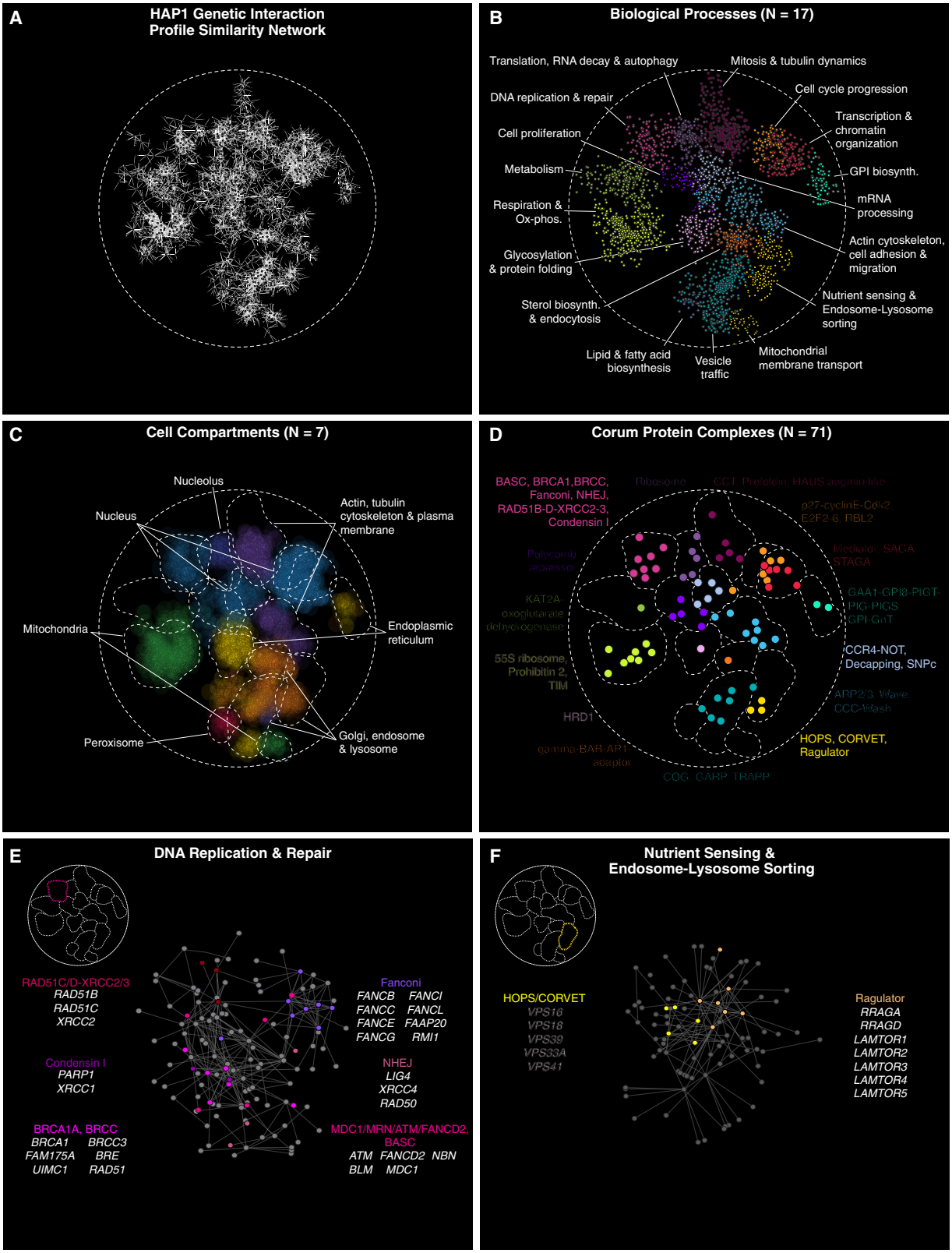

(legend on next page)

mediates membrane fusion during intracellular transport.[59] Notably, negative interactions uniquely identified by our study (~87%, 276/316) were enriched for genes involved in vesicle trafficking, suggesting that our CRISPR-KO approach is precise and sensitive (Figure S6B; Data S7).

We note that genetic interaction data generated in HAP1 cells exhibited similar quality and reproducibility to genetic interactions previously mapped in yeast.[4,5,60] Based on these analyses, we applied a standard threshold (|qGI| > 0.3 and FDR < 0.1) that optimized precision and recall of gene pairs co-annotated to the same Gene Ontology (GO) biological process term (Figure S5A; Data S4 and S5; Document S1) to generate a dataset of 88,933 genetic interactions, including 47,052 negative and 41,881 positive interactions. Correlation of replicate gene pairs supports the high quality of the dataset identified at this confidence threshold (r = 0.93) (Figure S5C), which forms the basis of all analyses in this study unless otherwise specified.

A functionally informative genetic interaction profile similarity network for a human cell

The genetic interaction profile of a gene represents its unique signature of negative and positive interactions, reflecting its biological function (Figures S3B–S3D, S7A, and S7B). For example, profiles for *FANCG*, *PDCD5*, and *VPS52* query genes mapped interactions with library genes that were consistent with known roles of these genes in DNA recombination, tubulin function, and vesicle trafficking, respectively (Figures S3B and S3C). Hierarchical clustering of the complete HAP1 genetic interaction dataset, based on 298 genome-wide screens, grouped together genes that shared similar interaction profiles, identifying subsets of genes that function together in the same bioprocess, pathway, or protein complex (Figure S8; Data S8). In total, we identified 412 clusters involving ~4,400 library genes, most (~93%, 384/412) of which were enriched for specific GO bioprocess terms that spanned diverse cellular functions (Figure S3D; Data S9).

We also used library gene interactions derived from the complete set of 298 screens to construct a genome-scale HAP1 genetic interaction profile similarity network (Figure 1; Data S10). Nodes in this network represent unique library genes, and edges connect gene pairs that share similar genetic interaction profiles (Figure 1A). The distance between connected gene pairs reflects their profile similarity. Proximally located genes share more similar patterns of genetic interactions, while genes positioned farther apart in the network display more divergent profiles (Figure 1A). The HAP1 network is relatively sparse because library gene profiles are based on genetic interactions with only 222 unique query genes. Nonetheless, ~74% (2,787/3,784) of genes on the network belonged to large, discernible network clusters. By applying spatial analysis of functional enrichment (SAFE),[61] with a GO bioprocess functional standard, we identified 17 densely connected network clusters, each enriched for related GO terms corresponding to a different bioprocess, such as DNA replication and repair or vesicle trafficking (Figure 1B; Data S11). Combining SAFE with a protein localization standard[62] highlighted seven larger network regions of neighboring bioprocess-enriched modules, each enriched for proteins localized to the same subcellular compartment (Figure 1C; Data S11). Nested within bioprocess-enriched network regions were smaller modules corresponding to 71 protein complexes (Figures 1D–1F; Data S11). Thus, the HAP1 genetic interaction profile similarity network exhibits a topology similar to the global yeast network,[4,5] revealing a functional hierarchy of human gene modules corresponding to protein complexes and pathways, biological processes, and cellular compartments. The complete dataset is provided in different formats (Data S4 and S8) and can also be accessed from our companion databases, https://thecellmap.org[63,64] or https://crisprdb.ccm.sickkids.ca/.

A genetic interaction profile similarity network provides a resource for annotating human gene function because a gene's location on the network connects it to specific biological functions.[5,60] Indeed, we linked 113 genes associated with relatively few citations and/or GO annotations to specific bioprocesses (Figures S9A and S9B; Data S12; Document S1). This general approach also facilitates functional characterization of different human gene datasets. For example, genes that confer sensitivity or resistance to a bioactive molecule cluster in distinct regions of the network, identifying the specific bioprocesses targeted by the compound and thus providing a strategy to predict the mode-of-action of novel bioactive compounds (Figure S9C; Data S13; Document S1).[67] Similarly, subsets of genes associated with shared disease traits or genome-wide association study (GWAS) phenotypes clustered together on the HAP1 genetic profile network, highlighting shared functional relationships among genes identified through statistical genetic analysis of disease cohort data (Figure S9D).

Figure 1. A genetic interaction profile similarity network for a human cell

(A) HAP1 genetic interaction network comprising 3,784 human genes (nodes). Gene pairs were connected by profile similarity (Pearson Correlation Coefficient [PCC] > 0.41) and graphed using the "yFiles Organic" network layout in Cytoscape (edges).[65] Genes sharing similar genetic interaction profiles are positioned near each other, whereas genes with less similar genetic interaction profiles are farther apart.

(B) HAP1 genetic interaction network annotated using SAFE[61] for Gene Ontology (GO) bioprocess terms.

(C) HAP1 genetic interaction network highlighting network regions that are enriched for proteins in the same cellular compartment. Node opacity reflects gene-level enrichment significance, with more enriched genes displayed more opaquely. Dashed lines represent network regions enriched for bioprocesses indicated in (B).

(D) HAP1 genetic interaction network annotated by highlighting CORUM protein complexes.[66] Nonredundant protein complexes were identified by assigning each gene to the largest complex it belongs to with >2 unique members. The centroid of the network positions of the genes annotated to a given protein complex was used to create the protein complex node. Nodes are colored according to the biological process-enriched region of the network to which they localized. Dashed lines indicate the network regions enriched for bioprocesses shown in (B).

(E and F) Genes belonging to the bioprocess-enriched network region highlighted in the inset were extracted from the HAP1 network, and genes (nodes) in the subnetworks were colored according to their CORUM protein complex annotation.

See also Figures S3, S7, S8, and S9.

Please cite this article in press as: Billmann et al., Global genetic interaction network of a human cell maps conserved principles and informs functional interpretation of gene co-essentiality profiles, Cell (2026), https://doi.org/10.1016/j.cell.2026.03.044

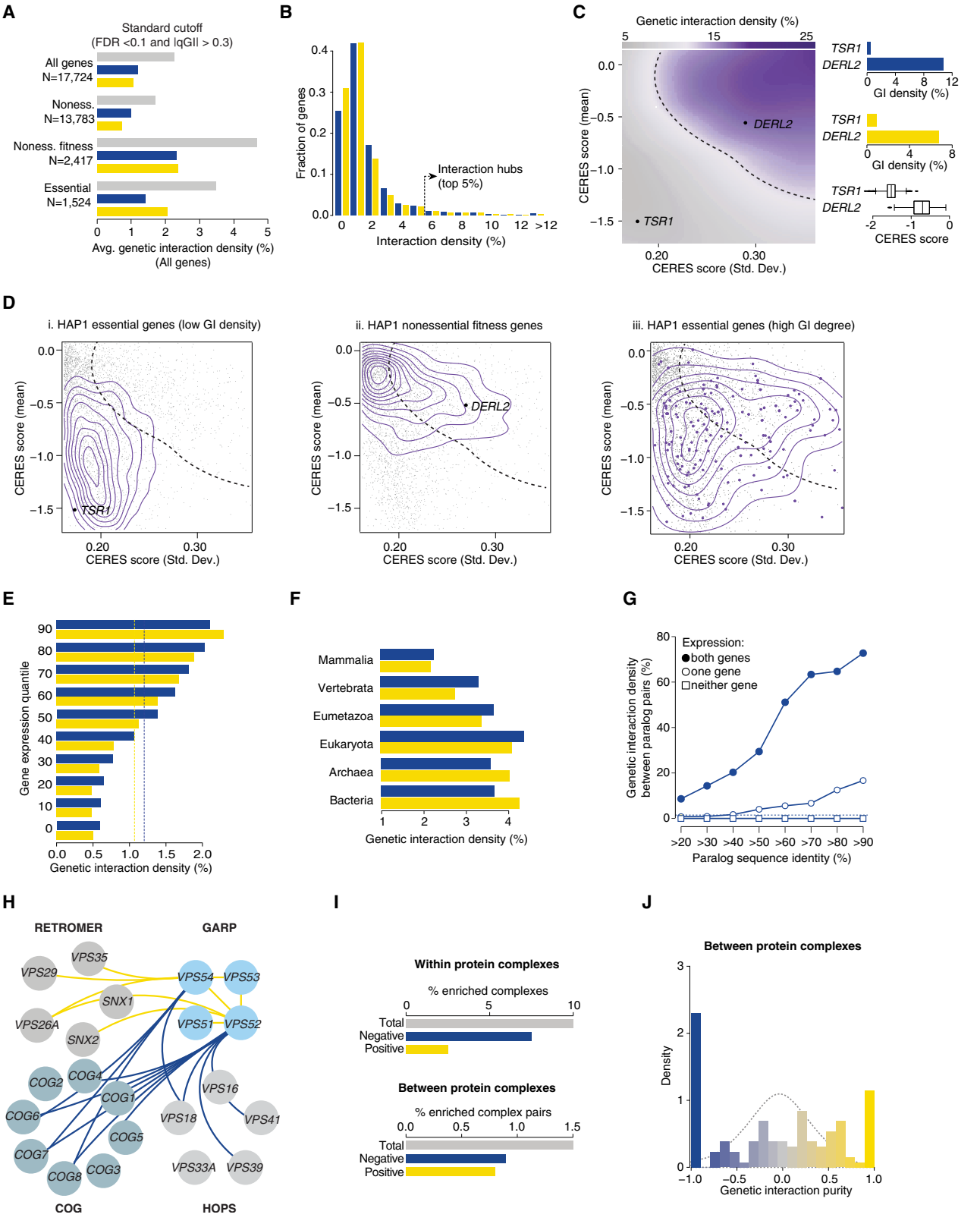

(legend on next page)

Please cite this article in press as: Billmann et al., Global genetic interaction network of a human cell maps conserved principles and informs functional interpretation of gene co-essentiality profiles, Cell (2026), https://doi.org/10.1016/j.cell.2026.03.044

Features of highly connected genetic network hubs

The nonredundant dataset, based on 222 unique query gene screens, was used to explore the functional distribution of genetic interactions. While the number of genetic interactions per library gene ranged between 0 and ~70, the average library gene interacted with ~2% of all query genes, exhibiting ~2–3 negative and ~2 positive interactions (Figures 2A and S10A; Data S14). Some genes participated in many interactions and serve as genetic network hubs. The top 5% most connected genes exhibited ~6-fold more interactions than the average gene (Figure 2B; Data S14). Although hub genes spanned various functions (Figures S10B–S10D), those involved in mitochondrial processes were among the most highly connected, exhibiting many interactions, especially positive interactions (Figures S7B and S10B–S10D; Data S14). In a previous study,[26] we identified experimental factors that can confound the scoring of mitochondrial gene co-essentiality profiles from DepMap data. Based on this analysis, we explored HAP1 genetic network properties using all available genes as well as a subset of data that excluded mitochondrial-related genes (Document S1).

Physiological and evolutionary properties characteristic of yeast genetic network hub genes were also associated with highly connected human genes in the HAP1 genetic network (Figures 2A–2G, S10, and S11).[4,5,69] For example, genetic interaction density (i.e., interactions/gene pairs tested) was related to single mutant fitness in HAP1 cells (Figures 2A, S10E, and S11). Nonessential genes with fitness defects showed ~2-fold more interactions relative to the average library gene, and the number of interactions was positively correlated with the severity of the library gene KO fitness defect (Figures 2A, S10A, and S10E).

Genetic interaction density was also correlated to gene fitness phenotypes measured across the DepMap panel of cancer cell lines (Figures 2C and S11). DepMap core essential genes showed fewer genetic interactions, while selectively essential genes exhibited higher genetic interaction density (Figures 2C and S11). Among HAP1 essential genes, most (~78%, 1,188/1,524) had average or below average network connectivity (Data S14) and were more likely to be classified as DepMap core essential genes (Figure 2D). However, a subset of HAP1 essential genes (~22%, 336/1,524) exhibited above-average interaction density and were more likely to be selectively essential, displaying variable fitness defects across the panel of DepMap cancer lines (Figures 2D and S10F; Data S14; Document S1). Thus, DepMap fitness metrics are predictive of genetic connectivity in the HAP1 network, which in turn can help distinguish core from selectively essential genes in the DepMap co-essentiality network.

Gene expression levels in HAP1 and other cancer cell lines were also positively correlated with genetic network connectivity (Figures 2E and S11). The most highly expressed genes in HAP1 cells exhibited ~2-fold more interactions compared with the average gene, while genes ranked in the bottom 40% by expression level had fewer interactions, as did genes with variable expression across different cell lines (Figures 2E and S11). Moreover, essential genes and nonessential gene mutants associated with fitness phenotypes were significantly enriched at common trans-chromosomal contact regions (binomial testing essential genes $p < 1.6 \times 10^{-21}$; nonessential genes $p < 2.67 \times 10^{-15}$),[70] indicating that these genes cluster in transcriptionally active regions of human genome topology (Figure S12A;

Figure 2. Genetic interaction density analysis

(A) Bar chart showing genetic interaction density (observed interactions/total gene pairs screened) for library genes by category (all genes, nonessential [Noness.], nonessential with fitness phenotypes [noness. fitness], and essential) at the indicated standard confidence threshold. Negative (blue), positive (yellow), and total (gray) interaction densities, along with the number of genes in each category, are indicated.

(B) Density distribution of negative (blue) and positive (yellow) interactions, highlighting the top 5% of genes with the highest interaction density.

(C) Genetic interaction density heatmap visualized as a function of a gene's single mutant standard deviation in the DepMap dataset (*x* axis, CERES score std. deviation) and the single mutant mean phenotype (*y* axis, mean CERES score). Darker purple represents increased total genetic interaction density (positive and negative interactions) in the HAP1 GI network. Right bar plots show positive and negative density and CERES score means for genes *TSR1* and *DERL2*. The dotted line indicates the boundary between high and low genetic interaction density.

(D) The distribution of genes belonging to each gene set is plotted as a function of a gene's single mutant standard deviation (*x* axis, CERES score std. deviation) and mean phenotype (*y* axis, mean CERES score) in the DepMap dataset. Plots show (i) HAP1 essential genes with the lowest 50% GI density, (ii) HAP1 nonessential genes with significant fitness effects, and (iii) HAP1 essential genes within the top 20% total interaction density. The contour lines reflect the density of the corresponding gene sets in this two-dimensional space. The dotted line indicates the boundary between high and low genetic interaction density as defined in (C). Gray nodes represent library genes with at least 1 genetic interaction ($|qGI| > 0.3$, FDR < 0.1). The purple nodes indicate HAP1 essential gene hubs. *TSR1* and *DERL2* are highlighted on the plots as (i) and (ii), respectively.

(E) The average negative (blue) and positive (yellow) interaction density for library genes as a function of expression in HAP1 cells, with dotted lines indicating background interaction densities across all tested library genes.

(F) The average negative (blue) and positive (yellow) interaction density for over 8,000 library genes, which exceed a defined expression threshold [$\log_2$(Transcripts Per Million [TPM] + 1) > 3] in HAP1 cells as a function of gene age, defined in Liebeskind et al.[68]

(G) Negative genetic interaction density among pairs of duplicated genes with increasing sequence identity (i.e., paralogs).

(H) Network of coherent negative (blue) or positive (yellow) genetic interactions among genes encoding members of the RETROMER, GARP, HOPS, and COG protein complexes. Node color indicates members of the same protein complex.

(I) Bar charts depicting the percentage of CORUM protein complexes whose members were enriched for any type of genetic interaction (gray), negative (blue), or positive (yellow) interactions with each other within (top) or between (bottom) protein complexes. Only single complexes and complex-complex pairs with at least 5 tested gene pairs were included in the analysis. Genes with mitochondrial-related functions were excluded from this analysis.

(J) Distribution of complex-complex pairs with respect to between-complex genetic interaction purity scores. A score of −1 indicates that genetic interactions occurring between a pair of protein complexes are exclusively composed of negative interactions, whereas a purity score of 1 indicates pairs of complexes connected strictly by positive interactions. The dotted gray line indicates the random expectation based on purity scores generated by sampling negative/positive interaction signs randomly according to a binomial distribution. Genes with mitochondrial-related functions were excluded from the analysis.

See also Figures S10, S12, and S13.

Please cite this article in press as: Billmann et al., Global genetic interaction network of a human cell maps conserved principles and informs functional interpretation of gene co-essentiality profiles, Cell (2026), https://doi.org/10.1016/j.cell.2026.03.044

Data S23). Genes that exhibited many genetic interactions also concentrate in these constitutive anchor regions,[70] further supporting a relationship between genetic interaction density and gene expression (Figure S12A). Thus, HAP1 genetic network hub genes tend to be highly and stably expressed across many different cell types.

Network hubs also tend to include older genes that are conserved across the phylogenetic tree, as well as genes that are less tolerant to mutation (Figures 2F and S11). In total, we identified over 30 gene features associated with genetic interaction density in HAP1 cells (Figure S11), which can be leveraged to develop predictive models for identifying hub genes likely to participate in extensive genetic interactions in other cell lines or model organisms.[69]

Genetic interactions involving duplicated genes

Due to intrinsic functional redundancy, duplicated genes generally showed fewer genetic interactions across the genome compared to other genes (Figures S12B and S12C). However, consistent with observations in yeast and other human cell lines,[34,71–77] paralog pairs expressed in HAP1 cells were often connected to each other by negative interactions but rarely by positive interactions (Figures 2G and S12D). Paralog pairs sharing ≥20% sequence identity were over 7-fold enriched for negative interactions (hypergeometric test, $p < 4.5 \times 10^{-30}$), and those sharing ≥90% identity showed over 60-fold enrichment (hypergeometric test, $p < 2.7 \times 10^{-16}$), whereas paralogs from larger gene families exhibited fewer interactions (Figures 2G and S12E).

We also observed an asymmetric pattern of interactions among paralog pairs, where one paralog exhibited significantly more negative interactions than its duplicate, often exceeding a 5-fold difference (Figure S12F). The observed asymmetry was greater than expected by chance ($p < 0.001$, empirical test), as previously shown in yeast,[71,72] suggesting that the paralog with more negative interactions may be under stronger evolutionary constraint.

Relating genetic and physical interactions

Gene pairs that are co-expressed and/or whose products physically interact, either as individual protein-protein interactions (PPIs), as part of protein complexes (co-complex), or as part of biological pathways (co-pathway), overlapped significantly with genetic interactions. For example, gene pairs whose products share a PPI were ∼3-fold enriched for negative interactions and ∼2-fold enriched for positive interactions (Figure S13A). While negative interactions involving either nonessential or essential genes overlapped PPIs to a similar extent, the overlap between PPIs and positive interactions depended on gene essentiality (Figure S13A). Similar to yeast,[5,78] positive interactions between nonessential genes overlapped significantly with PPIs, reflecting that simultaneous perturbation of two genes encoding members of the same nonessential pathway or protein complex, such as the Golgi-Associated Retrograde Protein (GARP) complex, does not further enhance the fitness defect associated with the corresponding single mutants (Figures 2H and S13A). Mitochondrial genes participated in many positive genetic interactions with each other, and while most functional trends were not impacted, an enrichment for positive interactions connecting essential genes whose protein products physically interact was observed when mitochondrial genes were included in the analysis, but a similar pattern was not observed when mitochondrial genes were excluded (Figure S13A).

We also examined negative and positive interactions among members of 40 protein complexes that were represented as both library and query genes (Data S15).[66] About 10% of complexes were enriched for within-complex interactions, representing ∼5-fold higher interaction density compared with the average gene (Figures 2I and S13B). Additionally, many pairs of complexes (∼1.5%, 124/8,250) were enriched for between-complex interactions (Figures 2I and S13B; Data S15). Genetic interactions that occur within a complex or between pairs of complexes were strongly biased for a single type of genetic interaction, either negative or positive (Figures 2J and S13B; Data S15). For example, negative interactions linked the GARP complex to the Conserved Oligomeric Golgi (COG) and Homotypic Fusion and Protein Sorting (HOPS) complexes involved in vesicle trafficking,[79] while positive interactions connected GARP to the RETROMER complex, suggesting shared roles in retrograde transport (Figure 2H).[80] In total, we identified 45 complex pairs connected exclusively by either negative or positive interactions, reflecting a highly organized and coherent network structure resembling the yeast genetic network (Figures 2H, 2J, and S13B; Data S15).[5]

Functional distribution of negative genetic interactions

Most negative interactions occurred between gene pairs annotated to the same GO bioprocess term, with the interaction density increasing with functional specificity of modules defined by the profile similarity network (Figures 3A and S14A–S14C; Data S16). For example, we observed strong negative interactions between the query gene *PELO*, which encodes a component of the PELO-HBS1L no-GO mRNA decay pathway, and library genes encoding all members of the SKI mRNA surveillance complex (i.e., *SKIC2/SKIV2L*, *SKIC3/TTC37*, *SKIC8/WDR61*, *FOCAD*, and *AVEN*) (Figure S14D). A reciprocal screen using a *SKIC2* query mutant cell line identified negative interactions with *PELO* and *HBS1L*, confirming a genetic relationship between these related functional modules (Figure S14D; Data S24). Notably, we also reproduced the negative interaction between *PELO* and *SKIC2* in a HC3716 liver cell line (Figure S14E), supporting the conservation of genetic interactions across different human cell lines and confirming a recently identified synthetic relationship between the SKI complex and the no-GO mRNA decay pathway in cancer.[81,82] Overall, ∼33% of negatively interacting gene pairs shared a functional relationship, such as localization to the same cellular compartment, involvement in the same bioprocess, or membership in the same pathway or complex (Figures 3B, S14B, and S14C).

The qGI score also provided a quantitative indicator of functional relatedness, as stronger negative interaction scores were associated with gene pairs that shared closer functional relationships. For example, gene pairs within the same pathway or complex tended to show the strongest negative interactions, followed by pairs in the same bioprocess, and then those that shared the same subcellular localization (Figures 3C and S14C).

Please cite this article in press as: Billmann et al., Global genetic interaction network of a human cell maps conserved principles and informs functional interpretation of gene co-essentiality profiles, Cell (2026), https://doi.org/10.1016/j.cell.2026.03.044

CellPress
OPEN ACCESS

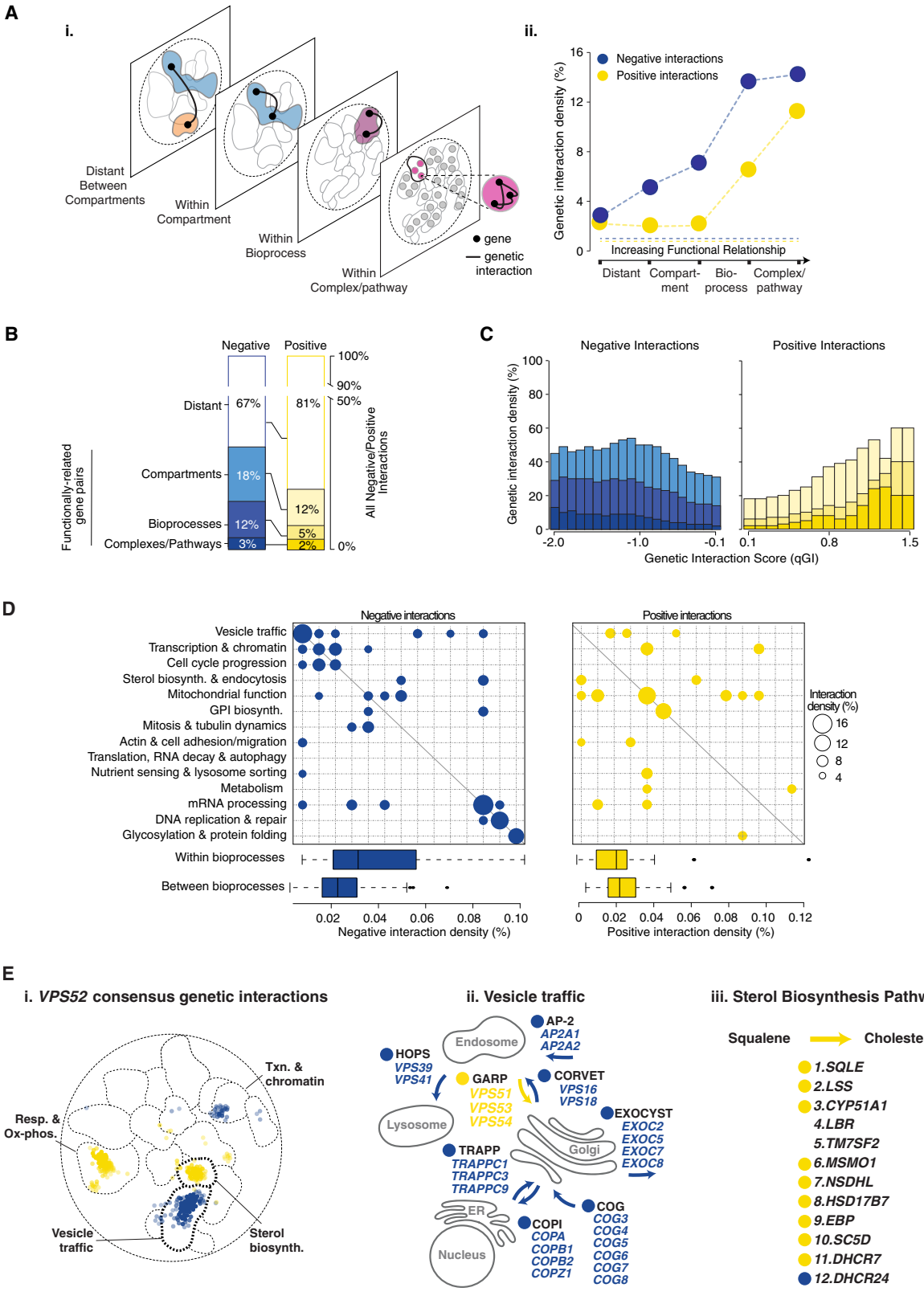

(legend on next page)

Please cite this article in press as: Billmann et al., Global genetic interaction network of a human cell maps conserved principles and informs functional interpretation of gene co-essentiality profiles, Cell (2026), https://doi.org/10.1016/j.cell.2026.03.044

We further analyzed connections within and between bioprocess-enriched modules. Negative interactions were enriched both within individual bioprocesses and between distinct bioprocess clusters, with stronger enrichment observed within the same bioprocess (Figure 3D, on diagonal versus off diagonal; Data S16). Although overall connectivity was relatively sparse, the pattern of negative interactions among human bioprocesses resembled that of the global yeast network when restricted to an equivalent number of query genes (Figure S14F).[5] These findings further highlight the conserved architecture of genetic networks.

Functional distribution of positive genetic interactions

The highest positive interaction density and strongest positive qGI scores were observed among genes in the same pathway or complex (Figures 3A, 3C, and S14A–S14C; Data S16). Notably, gene pairs involved in mitochondrial- or Glycosylphosphatidylinositol (GPI) biosynthesis-related roles were enriched for positive interactions (Figure 3D, on diagonal). However, only ~19% of positive interaction gene pairs were functionally related as defined by the HAP1 genetic profile similarity network (Figures 3B and S14C; Data S16), indicating that most positive interactions connected genes from different bioprocesses, a pattern also observed in yeast (Figures 3D and S14F, off diagonal).[5]

For example, while negative interactions for the *VPS52* query gene were enriched for related vesicle trafficking genes (~3-fold, FDR < 5.3×10^{-43}, hypergeometric test, BH-corrected), its positive interactions were enriched for genes involved in sterol biosynthesis (~3-fold, FDR < 2.4×10^{-18}, hypergeometric test, Benjamini-Hochberg [BH]-corrected) (Figure 3E). Studies in yeast, mouse, and human cells showed that GARP complex function is connected to cholesterol homeostasis.[83–85] GARP mediates sorting and localization of NPC2, a protein critical for lysosomal cholesterol export.[86,87] NPC2 is missorted in GARP-deficient mutants, leading to accumulation of cholesterol,[84] a hallmark of Niemann-Pick type C disease, a neurodegenerative disorder caused by mutations in *NPC2*.[86,87] Consistent with these findings, *VPS52* exhibited strong positive interactions with genes in the cholesterol biosynthetic pathway genes (Figure 3E), most of which we classified as suppression interactions because the relative double-mutant fitness was greater than the fitness of the *VPS52* query mutant (Figures 4A and S15A; Data S17). Similar suppression interactions were observed for *VPS54* (Figure S15A; Data S17), suggesting that GARP-associated fitness defects may result from toxic accumulation of cholesterol, which can be mitigated by reducing cholesterol biosynthesis.

Additionally, GARP mutant fitness defects were suppressed by disrupting sphingolipid biosynthesis genes (Figures 4A and S15B; Data S17). Mutations in *VPS53* and *VPS54* have been linked to cerebello-cerebral atrophy type 2 and ALS (amyotrophic lateral sclerosis), respectively.[88–90] Both neurodegenerative disorders are characterized by cellular accumulation of sphingolipid intermediates, and, accordingly, inhibition of sphingolipid biosynthesis rescues mutant phenotypes in relevant disease models.[83,85]

Systematic analysis of positive genetic suppression interactions

Extreme positive genetic interactions classified as suppression often provide mechanistic insight into gene function (Figures 4A and S15A–S15C; Data S17).[91,92] Our genetic suppression analysis in HAP1 cells previously uncovered novel functional insights into protein acetylation (Figures 4A and S15C).[45] More recently, we showed that LOF mutations in *ABHD18*, encoding a novel component of cardiolipin biosynthesis, rescued the fitness defect of HAP1 cells carrying a LOF mutation in *TAFAZZIN*, a disease gene linked to Barth Syndrome, and this suppression interaction was validated in both cell line and mouse disease models (Figures 4A and S15C).[93] To systematically assess the prevalence of suppression interactions, we compared double and single mutant fitness for all gene pairs connected by positive interactions in the HAP1 genetic network. Approximately 4% (1,843/41,881) of positive interactions were classified as potential suppression interactions, where the fitness of the double mutant exceeded that of the most severely affected single mutant (Figures S15A–S15C; Data S17). Consistent with findings in yeast[91,92] and reported human gene suppression interactions,[94] our set of HAP1 suppression interactions was more functionally informative than positive interactions overall, capturing ~2-fold more gene pairs annotated to the same GO biological process compared with positive interactions that were not classified as suppression (Figure S15D).

Figure 3. Functional distribution of genetic interactions

(A) (i) Schematic of genetic interactions within the functional hierarchy of the HAP1 genetic interaction profile similarity network, showing genetic interactions that occur within the same complex/pathway, biological process, or cellular compartment, and distant interactions between compartments, as defined in Figure 1. (ii) Line graph showing the observed genetic interaction density for genes within the same hierarchy level for negative (blue) and positive (yellow) genetic interactions (|qGI| > 0.3, FDR < 0.1). Horizontal dashed line shows the background density of negative and positive interactions. Analysis includes ~1,600 genes with high-confidence genetic interaction profiles and excludes mitochondrial-related genes.

(B) Functional distribution of all negative (blue) and all positive (yellow) interactions (|qGI| > 0.3, FDR < 0.1) in the genetic network hierarchy. Genes with mitochondrial-related functions are excluded from this analysis.

(C) Fraction of negative (blue) and positive (yellow) interactions within specified qGI score ranges connecting genes within different functional levels. Different shades of blue and yellow correspond to levels of functional relatedness shown in (B). Analysis includes ~1,600 genes with high-confidence genetic interaction profiles, excluding mitochondrial-related genes.

(D) Network density of genetic interactions (|qGI| > 0.3, FDR < 0.1) within and across biological processes for the indicated enriched gene sets. Diagonal nodes represent interactions within bioprocesses, and off-diagonal nodes represent interactions between bioprocesses. Node size reflects the fraction of interacting gene pairs. The average density of negative and positive interactions observed within and between bioprocesses is shown in the boxplots.

(E) (i) Network map showing regions of the HAP1 profile similarity network enriched for genes with negative (blue) or positive (yellow) consensus genetic interactions with a *VPS52* query gene (n = 5 biological replicates). (ii) Genes encoding members of vesicle tethering complexes that show coherent genetic interactions with *VPS52*. (iii) Most genes with roles in the cholesterol biosynthesis pathway show positive interactions with the *VPS52* query gene.

See also Figure S14.

Please cite this article in press as: Billmann et al., Global genetic interaction network of a human cell maps conserved principles and informs functional interpretation of gene co-essentiality profiles, Cell (2026), https://doi.org/10.1016/j.cell.2026.03.044

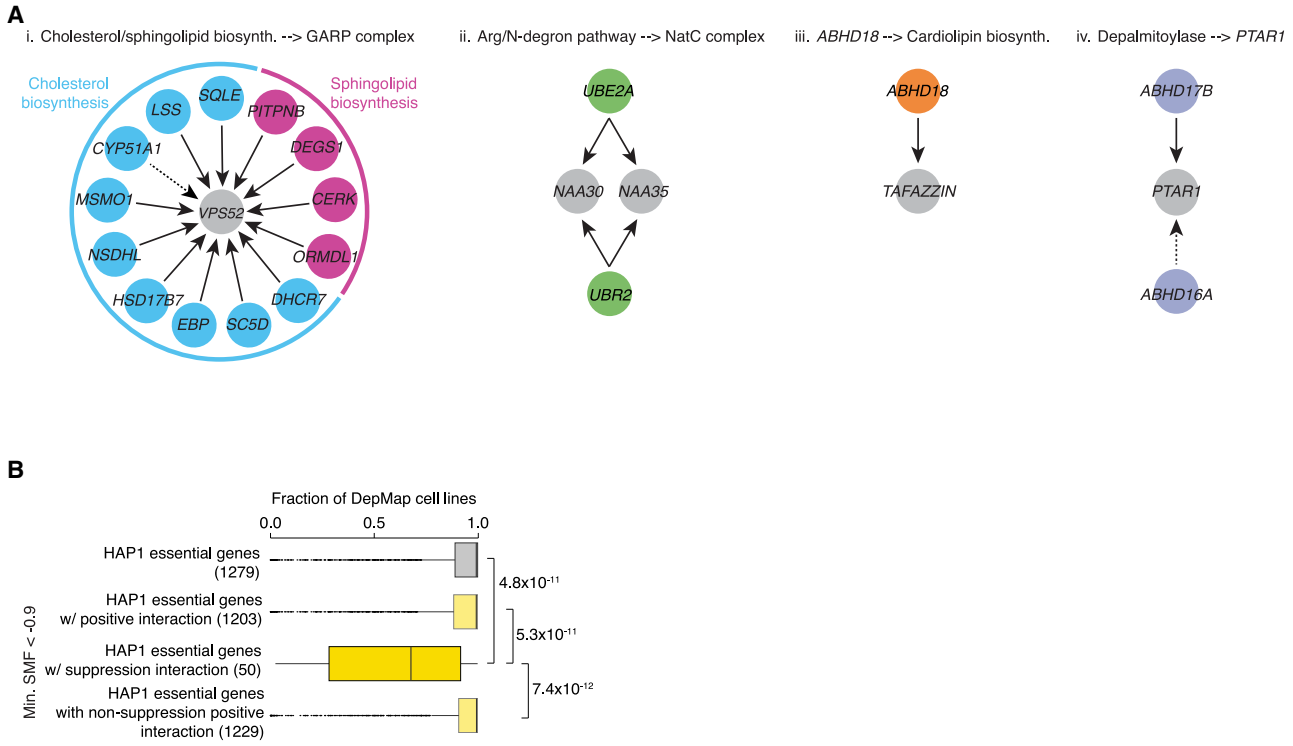

Figure 4. Genetic suppression interactions

(A) Specific examples of genetic suppression. Arrows indicate the direction of suppression. Gray nodes indicate genes whose mutant fitness phenotype is suppressed, and colored nodes represent suppressor genes. Dotted arrow indicates weak suppression interactions that did not satisfy a suppression score threshold (score > 0.5).

(B) Boxplot showing the mean percentage of DepMap cell lines that depend on the indicated groups of HAP1 essential genes for viability. Numbers of essential genes tested per group and significant differences in distributions of DepMap essential gene fraction between groups are indicated (*p* value, Wilcoxon rank-sum test). Genes with mitochondrial-related functions were excluded from this analysis.

See also Figure S15.

Approximately 17% of yeast essential genes can be rendered dispensable by spontaneous extragenic bypass suppressor mutations, and these genes are more likely to be nonessential across different yeast species compared with core essential genes.[91] In HAP1 cells, despite screening only 222 unique query genes, ~3% (50/1,524) of HAP1 essential library genes exhibited at least one potential bypass suppression interaction (Data S17). Notably, these genes tend to be essential in fewer DepMap cancer cell lines and are more likely to be classified as selective essential genes (Figures 4B and S15E).

Conservation of genetic network structure and topology

Genetic interactions appear to be broadly conserved at the level of network structure.[69,95–99] To investigate this conservation further, we compared genetic interaction density within and between bioprocess modules mapped by the yeast and HAP1 profile similarity networks. Remarkably, negative interaction density, both within individual bioprocesses and between related bioprocess pairs, was significantly correlated across species (Figure 5A; Data S18). For example, genes within the DNA replication and repair bioprocess show a relatively high density of interactions in yeast and human cells. Because there are relatively few orthologs represented in the yeast and HAP1 networks, these findings reflect deep conservation of network structure and topology despite divergence at the level of individual interactions.

By contrast, positive interaction density was not correlated between yeast and HAP1 networks (Figure S16A; Data S18). In yeast, positive interactions among essential genes often reflect broad regulatory mechanisms, such as mRNA degradation or protein turnover.[5] In HAP1 cells, positive interactions may also represent regulatory relationships specific to human cell proliferation. For instance, tumor suppressor genes showed a bias toward positive interactions (Figure S16B; Data S19), suggesting that their disruption enhances cell proliferation in many query mutant cell lines. Genes involved in mTOR signaling served as positive interaction hubs, highlighting how disruption of central regulatory pathways can influence numerous genes (Figure S10D; Data S14). Notably, HAP1 genetic interaction profiles identified several query cell lines with distinct dependencies on either mTORC1 or mTORC2 pathways, which we validated by monitoring mTORC1 and mTORC2 activity in several query cell lines (Figure S17; Document S1).

Of the ~4 million gene pairs tested in HAP1 cells, only 146,664 (~4%) have corresponding yeast orthologs (Figure 5B; Data S20). Nevertheless, conserved gene pairs with negative interactions in HAP1 cells were more likely to show negative

Please cite this article in press as: Billmann et al., Global genetic interaction network of a human cell maps conserved principles and informs functional interpretation of gene co-essentiality profiles, Cell (2026), https://doi.org/10.1016/j.cell.2026.03.044

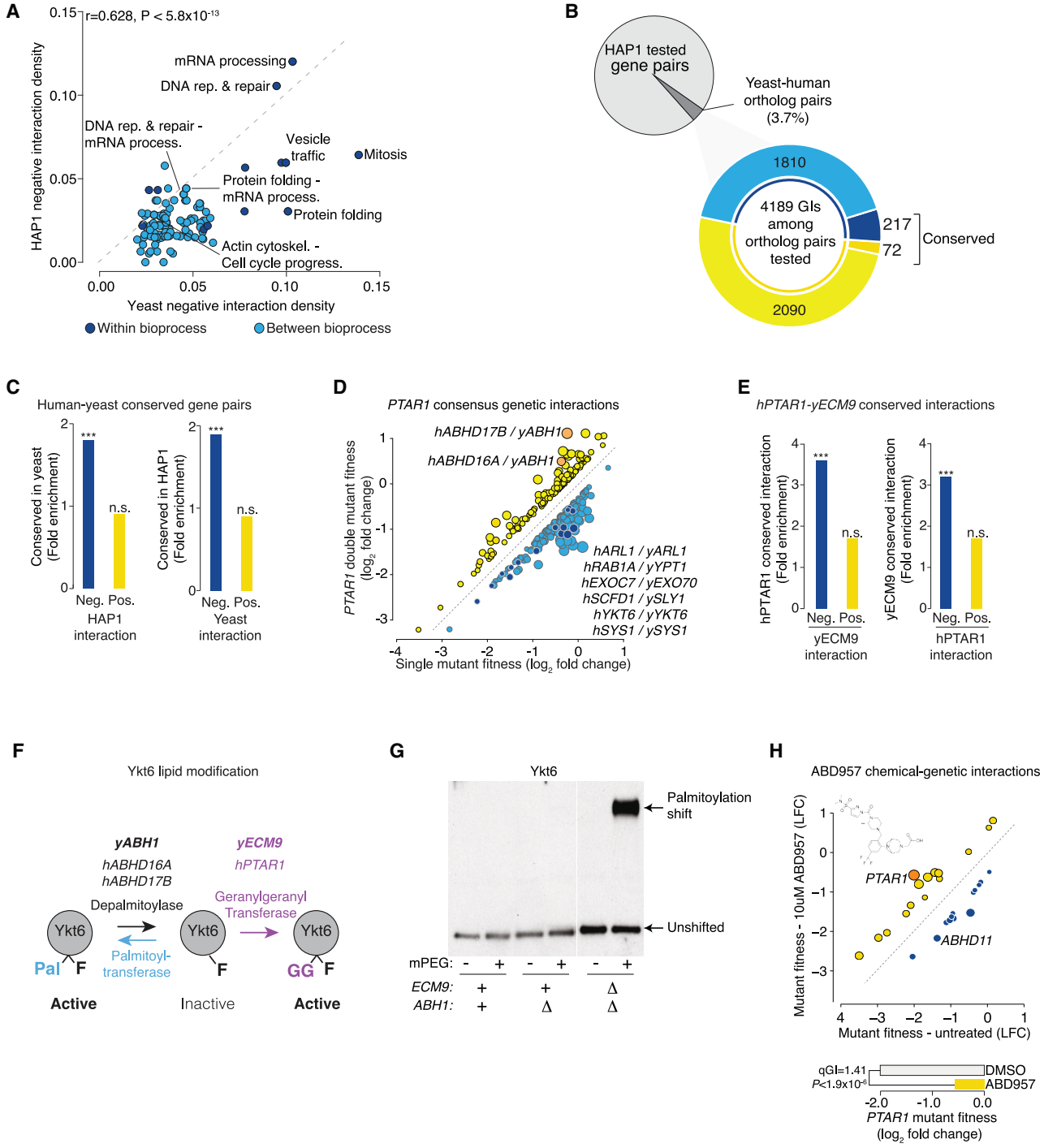

Figure 5. Genetic interaction conservation

(A) Scatterplot comparing human (qGI < −0.3, FDR < 0.1) and yeast (Synthetic Genetic Array [SGA] score < −0.08, $p < 0.05$) negative interaction densities within bioprocesses (dark blue) and between pairs of bioprocesses (light blue).

(B) Pie chart shows the fraction of conserved gene pairs tested in HAP1, while the donut plot summarizes negative and positive interactions in HAP1 among conserved gene pairs. Dark blue and dark yellow represent conserved negative and positive interactions, while light blue and light yellow indicate interactions found only in HAP1.

(C) Bar graph illustrating enrichment for negative (blue) and positive (yellow) interactions in yeast among conserved gene pairs that showed a negative or positive genetic interaction in HAP1 cells (left). Bar graph illustrating enrichment for negative (blue) and positive (yellow) interactions in HAP1 cells among conserved gene pairs that showed a negative or positive genetic interaction in yeast (right). ***$p < 10^{-6}$, Fisher's exact test. n.s. denotes not significant.

(legend continued on next page)

interactions in yeast and vice versa (Figures 5C, S18A, and S18B). Gene pairs with roles in vesicle trafficking, mitosis, and DNA replication and repair were enriched for conserved negative interactions (Figure S18C). Overall, a modest fraction of genetic interactions (~7%, 289/4,189) among conserved gene pairs in HAP1 were also observed in yeast. Negative genetic interactions were significantly conserved, while orthology was not predictive of positive interactions (Figures 5B, 5C, S18A, and S18B; Data S20). This contrasts with genetic network structure and topology, which appear to be highly conserved across species.

Functional insights from comparative analysis of yeast and human genetic interaction profiles

Although most genetic interactions identified in HAP1 cells were unique to human genes, some human genes shared overlapping genetic interaction profiles with their corresponding yeast ortholog (Figure S19A). For example, human *PTAR1* interactions mapped in HAP1 cells overlapped significantly with those of yeast *YKT6*, a conserved SNARE protein (Figure S19B). PTAR1 forms a heterodimeric GGTase-III complex with RABGGTB to activate target proteins, including YKT6.[59,100–102] Sequence conservation and functional analyses identified a previously uncharacterized yeast essential gene, *ECM9*, as a distant ortholog of *PTAR1* (Figures S19C and S19D; Document S1).[103,104] We screened a temperature-sensitive *ECM9* query mutant allele to identify negative interactions enriched for vesicle trafficking genes that overlapped significantly with the negative interaction profile of *PTAR1* (Figures 5D, 5E, S19E, and S19F; Data S20).

Although positive interaction overlap was not significant (Figures 5E and S19F), some *ECM9*- and *PTAR1*-positive interactions were conserved and biologically informative. In particular, *PTAR1* query mutant fitness defects were suppressed by LOF mutations in *ABHD16A* or *ABHD17B*, which encode depalmitoylase enzymes (Figures 4A, 5D, and S15C; Data S17 and S20).[105] Analogously, we previously showed that the lethality of an *ECM9* deletion mutant is suppressed by disruption of yeast *ABH1* (*YNL320W*), which also encodes a putative depalmitoylase.[91,103] Expression of human *ABHD16A*, *ABHD17B*, or related gene family members rescued the bypass suppression phenotype of an *ecm9Δ abh1Δ* yeast double mutant, suggesting that these human abhydrolase genes act as functional orthologs of yeast *ABH1* (Figure S19G).

GGTase-III modifies mono-farnesylated yeast Ykt6 (yYkt6) and human YKT6 (hYKT6) to produce a dual-prenylated, active SNARE.[59,102,106] Our results imply that in the absence of GGTase-III, farnesylated yYkt6/hYKT6 can instead be palmitoylated, generating an alternative dual lipid-modified and active SNARE. Mutations in depalmitoylases, such as yeast *ABH1* or human *ABHD16A* or *ABHD17B*, which negatively regulate palmitoylation, may promote yYkt6/hYKT6 activation (Figure 5F). Indeed, yeast Ykt6 was palmitoylated in an *ecm9Δ abh1Δ* double mutant but not in *abh1Δ* single mutant or WT cells (Figure 5G). Moreover, a chemical-genetic screen in HAP1 cells with ABD957, a small molecule inhibitor of the *ABHD17* family of depalmitoylases, identified a strong positive chemical-genetic interaction with a HAP1 *PTAR1* query mutant cell line, suggesting that chemical inhibition of *ABHD17B* enzyme activity suppresses the fitness defect associated with a *PTAR1* mutant (Figure 5H; Data S13).[107]

These findings were further supported by the DepMap dataset because cancer cell lines that are more dependent on *PTAR1* for growth tend to express *YKT6* at lower levels, consistent with the *PTAR1-YKT6* negative interaction in HAP1 cells and suggesting a role for PTAR1 as a YKT6 activator (Figure 6A). Conversely, *PTAR1*-dependent cell lines often expressed higher *ABHD16A* levels, consistent with a *PTAR1-ABHD16A* positive interaction in HAP1 cells and suggesting that ABHD16A antagonizes PTAR1 function (Figure 6A). *YKT6* and *ABHD16A* expression levels were the strongest predictors of *PTAR1* dependency across DepMap cancer cell lines (DepMap: depmap.org/portal).

Deciphering molecular mechanisms underlying cancer cell line genetic dependencies

To systematically examine the relationship between DepMap cancer cell line genetic dependencies and HAP1 genetic interactions, we developed an expression dependency (ED) score, which quantifies the correlation between gene expression and LOF fitness phenotypes (Data S21). A negative ED score indicates that the fitness associated with LOF of gene A is more detrimental when gene B is highly expressed, while a positive ED score suggests that LOF of gene C is less detrimental when gene D is highly expressed (Figure 6B).

We computed ED scores for ~4 million gene pairs tested for genetic interactions in HAP1 cells to identify ~218,000 significant negative ED gene pairs and ~247,000 significant positive ED gene pairs ($|ED| > 0.1$, $p < 0.01$) (Figures 6B and S20A; Data S21). Notably, ~1% of negative ED gene pairs (~2,600) were enriched for HAP1-positive genetic interactions (1.2-fold, $p < 4.7 \times 10^{-22}$, hypergeometric test) (Figures 6B and S20A; Data S21), including *PTAR1-ABHD16A* and *TAFAZZIN-ABHD18* genetic suppression interactions (Figures 6A, 6C, S15C, and S20B; Data S21).[93] We also noticed that the *TP53*

(D) Consensus genetic interactions for *PTAR1*. Mean negative (blue) and positive (yellow) qGI scores ($|qGI| > 0.3$ and FDR < 0.1) based on genetic interactions from 4 independent *PTAR1* genome-wide screens are shown. Conserved negative (dark blue) and positive (orange) genetic interactions identified in HAP1 and yeast screens using human *PTAR1* and yeast *ECM9* orthologous query genes are shown, and specific examples of conserved interactions are indicated.
(E) Bar graphs illustrating enrichment for *PTAR1* negative (blue) and positive (yellow) genetic interactions in HAP1 cells among conserved gene pairs that showed a negative or positive genetic interaction with yeast *ECM9*, and vice versa. ***$p < 10^{-5}$, Fisher's exact test.
(F) Schematic model for dual lipid modification-dependent activation of Ykt6.
(G) Immunoblot for Ykt6 palmitoylation assessed by mPEG replacement chemistry using protein extracts from the three indicated yeast strains.
(H) Chemical-genetic interaction profile mapped for the depalmitoylase inhibitor ABD957. Negative (blue) and positive (yellow) chemical-genetic interactions that satisfied a standard confidence threshold are shown, with select genes highlighted. The chemical structure of ABD957 is shown. Bar graph shows *PTAR1* mutant fitness in ABD957 and DMSO conditions.
See also Figures S16, S17, S18, and S19.

Please cite this article in press as: Billmann et al., Global genetic interaction network of a human cell maps conserved principles and informs functional interpretation of gene co-essentiality profiles, Cell (2026), https://doi.org/10.1016/j.cell.2026.03.044

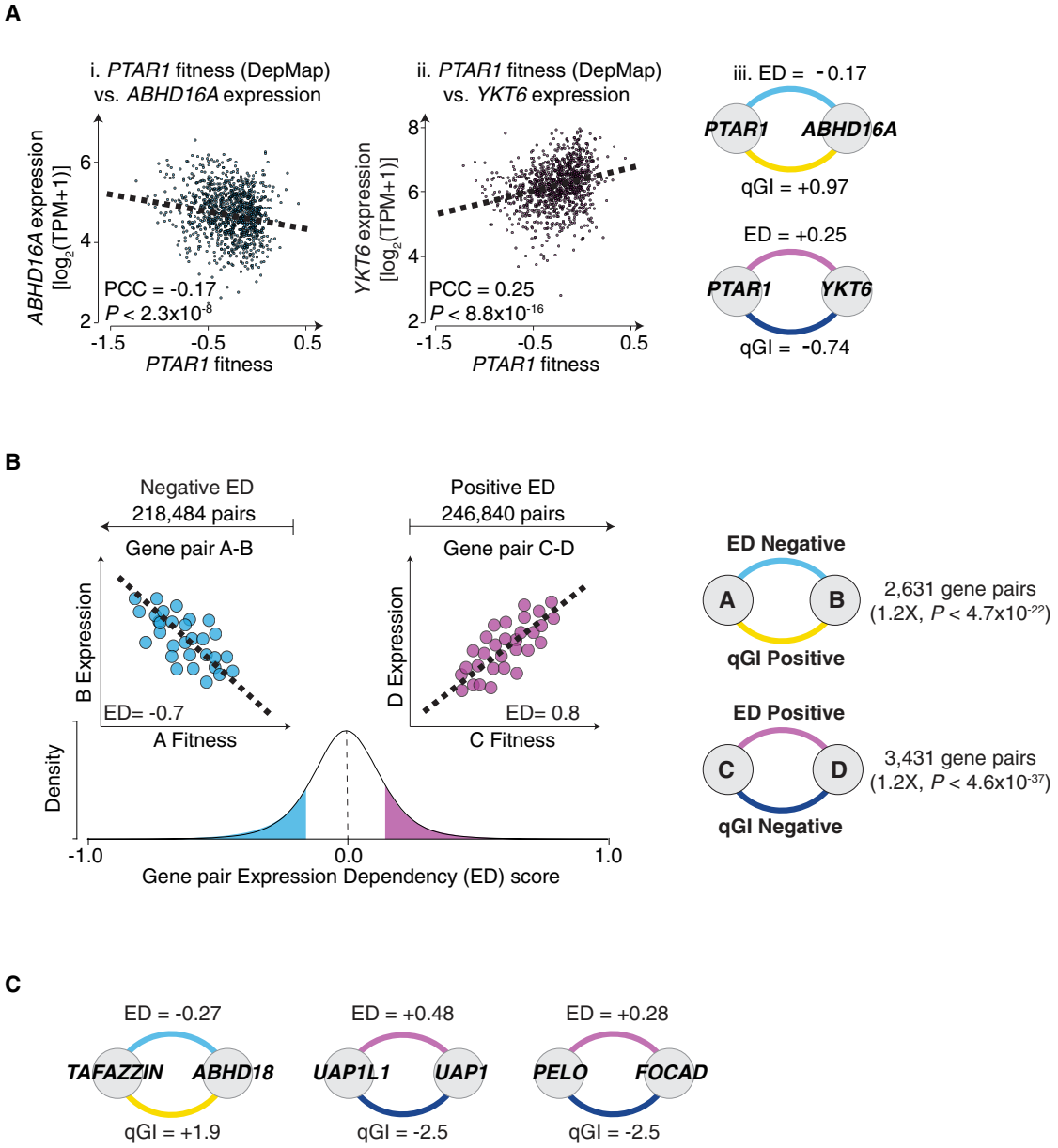

Figure 6. Relationship between DepMap cancer cell line ED and HAP1 genetic interactions

(A) Scatterplots illustrating the relationship between *PTAR1* mutant fitness and expression of either (i) *ABHD16A* or (ii) *YKT6* across DepMap cancer cell lines (Wald test on slope derived from linear regression). (iii) The *PTAR1-ABHD16A* gene pair shows a negative expression dependency (ED) score and a positive genetic interaction score (qGI). The *PTAR1-YKT6* gene pair shows a positive ED score and a negative qGI score.

(B) Schematic illustrating the distribution of ED scores for all gene pairs tested in this study and the overlap between ED and qGI scores. Overlap between ED scores and qGI scores is indicated (Hypergeometric test).

(C) Selected examples of specific gene pairs that exhibited significant ED-qGI combinations.

See also Figure S20.

tumor suppressor gene followed this pattern with numerous other genes (Data S21), many of which showed higher rates of co-mutation with *TP53* in tumors, suggesting that their disruption may enhance *TP53*-associated cancer phenotypes (Figure S20C).

Approximately 1% of positive ED gene pairs (~3,400) were enriched for HAP1 negative interactions (1.2-fold, $p < 4.6 \times 10^{-37}$, hypergeometric test) and often involved duplicated genes (Figures 6B and S20A; Data S21). Gene pairs with positive DepMap ED and HAP1 negative qGI scores were over 100-fold more enriched for paralogs compared with gene pairs with a positive ED score alone, highlighting the ability of paralogs to functionally compensate for one another, such as *UAP1* and *UAP1L1* glycosylation genes (Figures 6C, S20A, and S20B).[108,109] The

Please cite this article in press as: Billmann et al., Global genetic interaction network of a human cell maps conserved principles and informs functional interpretation of gene co-essentiality profiles, Cell (2026), https://doi.org/10.1016/j.cell.2026.03.044

CellPress
OPEN ACCESS

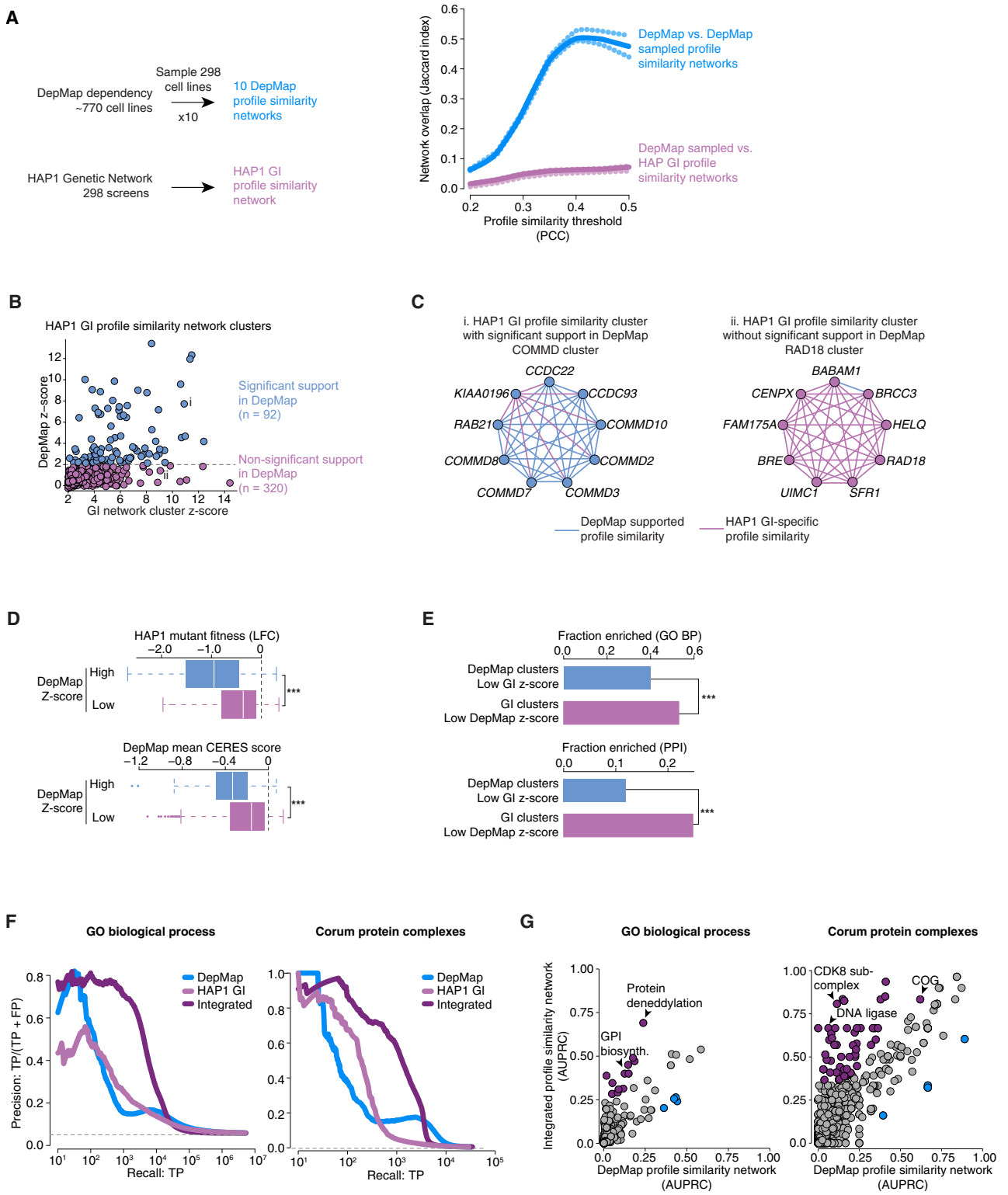

Figure 7. An integrated functional network based on genetic interaction and co-essentiality profiles

(A) Comparison of the overlap between correlated gene pairs in the complete HAP1 genetic interaction profile similarity and DepMap co-essentiality sampled networks. Co-essentiality networks were constructed by selecting non-overlapping random samples of 298 screens from the DepMap dataset (20Q2). This was repeated to generate 10 co-essentiality networks. Network overlap was assessed by computing Jaccard indices at increasing network similarity thresholds

(legend continued on next page)

Please cite this article in press as: Billmann et al., Global genetic interaction network of a human cell maps conserved principles and informs functional interpretation of gene co-essentiality profiles, Cell (2026), https://doi.org/10.1016/j.cell.2026.03.044

PELO-FOCAD gene pair exhibited the same pattern, supporting recent studies that identified a synthetic lethal relationship between *PELO* and 9p21.3 deletions (Figures 6C and S20B).[81,82]

Integrating HAP1 genetic interaction profile similarity and DepMap co-essentiality networks

Like genetic profile similarity networks, the DepMap co-essentiality network identifies genes that work together in functional modules.[4,5,22,25] To compare functional content captured by HAP1 genetic interaction profiles and DepMap co-essentiality profiles on a similar scale, we constructed 10 DepMap co-essentiality subnetworks using 298 randomly sampled DepMap cell lines, matching the number of genome-wide screens used to map the HAP1 profile similarity network (Figure 7A). At stringent thresholds (PCC > 0.4), we observed a relatively high overlap (Jaccard index of ~0.5) between DepMap subnetworks, but low overlap with the HAP1 network, indicating that the DepMap co-essentiality and HAP1 genetic profile similarity networks largely capture orthogonal functional information (Figure 7A).

We identified 412 gene modules in the HAP1 genetic interaction profile similarity network (Figures S3D and S9A; Data S9). Of these, 22% (92/412) comprised functionally related genes that were significantly connected in the complete DepMap co-essentiality network and shared similar characteristics (Figures 7B, 7C, S21A, and S21B; Data S22).[110–112] However, most HAP1 network modules (~78%, 320/412) were not supported by strong evidence in the complete DepMap network and involved genes with more moderate fitness defects (Figures 7B–7D; Data S22). HAP1 network-specific modules were slightly more enriched for functionally related genes and PPIs than DepMap-specific modules (Figure 7E), suggesting that the HAP1 genetic network captures functional relationships among nonessential genes with more subtle fitness defects, perhaps because the phenotypic effect of their disruption can be detected more sensitively in the context of a single genetic background.

A reciprocal comparison showed that most of the ~1,100 modules derived from the complete DepMap co-essentiality network were unique to the DepMap network and involved genes with low expression and modest fitness effects in HAP1 cells (Figures S21C–S21E; Data S22). These findings show that the two networks capture complementary features of gene function. While DepMap modules highlight essential gene relationships across diverse genetic backgrounds, the HAP1 network uncovers gene-specific interactions in a single genetic background, which captures nonessential genes with subtle fitness effects.

We combined a novel method for processing CRISPR screen data, Onion normalization,[113] with a deep learning-based approach for network integration, BIONIC,[114] to generate an integrated network based on the HAP1 genetic interaction profile similarity and DepMap co-essentiality input networks. In the resulting integrated network, functionally related gene pairs with roles in the same GO-annotated bioprocess or whose products interact physically were connected more frequently than in either input network alone (Figures 7F and S21F). Furthermore, modules derived from the integrated network identified new functions and protein complexes that were not represented in the individual input network (Figures 7G and S21G; Data S22). Thus, integrating data derived from our HAP1 genetic interaction profile similarity network with the DepMap co-essentiality network provides a more comprehensive view of human gene function.

DISCUSSION

A systematic genetic interaction map for a HAP1 human cell line uncovers fundamental principles of cellular organization and reveals conserved network features that transcend species. Integrating this map with existing datasets like the DepMap cancer cell line co-essentiality network, we provide a rich framework for understanding gene function, disease gene modifiers, and therapeutic vulnerabilities.

Our findings show experimental evidence that the overall structure of genetic interaction networks is conserved from yeast to human cells, which should enable predictive modeling of genetic interactions, identification of network hubs, and efficient,

(Pearson's correlation coefficient thresholds). The same procedure was used to measure the similarity of each DepMap co-essentiality network to the HAP1 genetic interaction profile similarity network. Continuous lines represent the mean Jaccard index of the DepMap-DepMap network comparisons (blue) and the DepMap-GI network comparisons (purple). The dotted lines represent the quartiles of Jaccard indices.

(B) Scatterplot of *Z* scores for modules or gene clusters identified from the genetic interaction profile similarity network. Modules with significant similarity in the DepMap co-essentiality network (blue) and modules without significant similarity (purple) are plotted. The gray dashed line indicates the *Z* score threshold for DepMap co-essentiality network similarity. (i) and (ii) indicate example modules highlighted in (C).

(C) Examples of modules derived from the genetic interaction profile similarity network.

(D) Boxplots of mean fitness in HAP1 cells and fitness in DepMap cancer cell lines for genes in significant modules that also share similar co-essentiality profiles (blue bars) or do not have strongly correlated co-essentiality profiles (purple bars). ***$p < 10^{-6}$ (Wilcoxon rank-sum test).

(E) Bar plot illustrating the fraction of network modules enriched for GO-Biological Process (BP) terms (hypergeometric test, Benjamini-Hochberg-corrected FDR < 0.2) or PPIs (hypergeometric test, Benjamini-Hochberg-corrected FDR < 0.05). Modules uniquely identified by genetic interaction network profiles (GI clusters, low DepMap *Z* score; GI module *Z* score > 2 and DepMap module *Z* score < 2) are indicated in purple. Modules specifically identified in the DepMap co-essentiality network (DepMap clusters, low GI *Z* score, GI module *Z* score < 2, and DepMap module *Z* score > 2) are indicated in blue.

(F) Precision-recall plots for genes exhibiting similar DepMap co-essentiality profiles (blue), genetic interaction profiles (light purple), or profiles from the integrated network. True positives (TPs) involve gene pairs co-annotated to a gold standard set of GO-BP terms (left panel) or gene pairs encoding members of the same CORUM protein complex (right panel). Dashed line represents background co-annotation rates. Genes annotated with a mitochondrial-related function were excluded because profile similarity profiles tend to be dominated by mitochondrial genes.[26] The same precision-recall analysis based on all genes, including mitochondrial genes, is shown in Figure S21F.

(G) Comparison of individual GO-BPs or CORUM protein complexes captured by the DepMAP co-essentiality network and the integrated network. Nodes above (purple) or below (blue) the diagonal indicate better performance by the integrated or DepMap networks, respectively. Performance is based on AUPRC (area under a precision-recall curve) values computed per GO-BP process or CORUM complex.

See also Figure S21.

large-scale genetic interaction analysis across different cell lines and model organisms.[69] As demonstrated with the global yeast genetic network,[5,57,71,115] the HAP1 genetic network should also serve as a reference for exploring higher-order interactions involving more than two genes, as well as allele-, cell line-, and condition-specific genetic interactions.

Genetic interactions highlight the potential to modulate the phenotypic consequences of genetic variation. We identified ~1,500 genes that are individually essential for HAP1 cell fitness. Based on our mapping of ~89,000 genetic interactions in HAP1 cells, we estimate that a global HAP1 genetic network may encompass ~1.4 million gene-gene interactions, including ~85,000 extreme negative synthetic lethal interactions and ~45,000 extreme positive suppressor interactions (see STAR Methods). The prevalence of genetic interactions in HAP1 cells is relevant to human disease and population genetics, where most phenotypes reflect quantitative traits shaped by individual genetic backgrounds. Even Mendelian disorders show variable disease phenotypes due to genetic modifiers that enhance or suppress a disease mutation.[116] Our HAP1 genetic network identified over 1,000 HAP1 synthetic lethal interactions involving more than 350 nonessential disease genes annotated in the OMIM database (Figure S22),[117] offering insights into potential disease gene modifiers and opportunities for variant effect mapping.[118] Approximately 9% (~287/3,341) of synthetic lethal interactions involved LOF mutations in known tumor suppressor genes (Figure S22)[119] that can be explored for potential targeted cancer therapy.[15,120–123]

In rare cases, healthy individuals can harbor mutations that normally cause severe Mendelian diseases. This resilience may be associated with modifiers that suppress the effects of a disease gene.[124] In total, we mapped ~1,800 suppression interactions in HAP1 cells, including ~600 suppression interactions involving an OMIM-associated disease gene (Figure S22).

The DepMap project catalogs gene dependencies across hundreds of cancer cell lines to generate a gene-cell line dataset,[7–11,53] which complements our gene-gene HAP1 genetic interaction network. DepMap fitness metrics were predictive of HAP1 genetic interaction network connectivity, suggesting that these data can guide query gene or cell line selection for efficient genetic interaction mapping. Although DepMap genetic perturbation analyses identify single gene fitness phenotypes across genetically diverse cancer cell lines, this approach does not directly identify genetic interactions between specific gene pairs. For high-frequency mutations or expression effects, interactions can sometimes be inferred through analysis of recurrent dependencies,[11] but the sensitivity of such analyses is limited by the number of relevant cell lines. We demonstrated that combining gene expression and single gene genetic dependency data from DepMap with HAP1 genetic interactions can identify molecular mechanisms underlying cell line-specific phenotypes (Figures 5F and 6A). This data integration infers gene pairs that would likely display either positive or negative genetic interactions of various strengths across diverse genetic backgrounds (Figures 6 and S20). For example, we identified gene pairs with negative DepMap ED and positive HAP1 qGI scores that may prioritize suppressors of disease gene phenotypes (Figure 6).[93] Indeed, ~36% (641/1,764) of unique library genes among pairs with negative ED and positive qGI scores are annotated to an OMIM disease term. Conversely, gene pairs with positive ED and negative qGI scores identified cancer-relevant synthetic lethal/sick gene pairs that may be exploited to develop new therapeutic strategies (Figures 6C and S20C).[81,82]

Complex diseases often result from combinations of detrimental variants in multiple genes, and different combinations of variants can lead to the same disease.[125–134] The conserved and modular topology of genetic networks, where coherent sets of negative or positive interactions connect functional modules, provides a framework to map the genetic architecture of inherited phenotypes.[135,136] Functional modules provide prior knowledge that can reduce the statistical burden in disease association studies.[135,136] The HAP1 genetic network presents an unbiased resource to identify functional modules and their genetic wiring. Extensive mapping of genetic networks across diverse human cell lines should provide a powerful approach for assigning most human genes into functional modules, thus providing a critical resource for exploring genetic interactions in population-scale biobank datasets, which link genome sequences to a wide range of phenotypes, including human diseases.[5,137–139]

Limitations of the study

This work focused on constructing a systematic, large-scale genetic interaction network involving predominantly nonessential genes in a single human cell line. Previous analyses in yeast showed that essential genes participate in ~5 times more interactions than nonessential genes, and their interaction profiles are rich in functional information, forming the central core of the yeast genetic profile similarity network.[5] Our ability to score genetic interactions for HAP1 essential genes was primarily limited to disrupting a subset of highly expressed library genes and/or those encoding stable or abundant proteins, which likely decay more slowly over the course of a screen (Figure S10F).[26] Thus, extending this approach to query cell lines that stably express hypomorphic alleles of essential genes should yield informative genetic interaction profiles for human essential genes.[140] To date, we have assayed <5% of all possible HAP1 gene pairs. Thus, a comprehensive HAP1 GI network has the potential to generate a high-resolution map of human gene function. Moreover, genome-scale analysis in additional cell lines will be highly valuable, as genetic interactions and their biological consequences can depend on genetic background, epigenetic context, and lineage-specific regulatory networks. Each tissue or cell type would likely reveal unique genetic interactions not captured in a single cell line. Large-scale application of combinatorial CRISPR libraries, designed to simultaneously inactivate pairs of genes, also promises to expand genome-wide genetic interaction analysis to include essential genes across diverse cell lines.[34,42,43] By contrast, the DepMap co-essentiality network appears to be approaching saturation in functional information (Figure 7A). Our HAP1 genetic interaction network provides a valuable reference, underscoring the potential for genetic interaction analysis to generate new insights into gene function and the genotype-phenotype relationship.

RESOURCE AVAILABILITY

Lead contact

Requests for further information and resources should be directed to the lead contact, Charles Boone (charlie.boone@utoronto.ca).

Materials availability

All material and data are described and/or available as supplemental information. The TKOv3 CRISPR library is available from Addgene (catalog no. 90294). HAP1 query mutant cell lines constructed "in house" or purchased from Horizon Discovery (https://horizondiscovery.com) are indicated in Data S1. HAP1 query mutant cell lines constructed in house are available upon request and without restriction.

Data and code availability

All primary data and data from associated analyses are available from https://boonelab.ccbr.utoronto.ca/supplement/billmanncostanzo2026/ and also deposited on Mendeley at https://doi.org/10.17632/bpcpfns6vb.1. All data are publicly available as of the date of publication. The HAP1 genetic interaction dataset can also be accessed and visualized through our companion databases: https://thecellmap.org[63,64] or https://crisprdb.ccm.sickkids.ca/.

All original code has been deposited at Zenodo and is publicly available at https://doi.org/10.5281/zenodo.15320010 as of the date of publication.

ACKNOWLEDGMENTS

We especially thank Jasper Rine for interpreting the yeast *ECM9* genetic suppression interactions. We also thank The Centre for Applied Genomics at SickKids Hospital and the Donnelly Sequencing Centre for assistance with sequencing. Finally, B.A., C.B., M. Costanzo, and C.L.M. thank David Botstein for his pioneering work in genetics and genomics, fueled by his boundless enthusiasm for rigorous science, which profoundly shaped our exploration of genetic networks. This work was supported by National Institutes of Health grants R01HG00583 (B.A., C.B., and C.L.M.), R01HG005084 (C.L.M.), and T32GM008347 (H.N.W.); Canadian Institutes of Health Research grants PJT-180285 (C.B.), PJT-GMX-463531 and MOP_142735 (J.M.), and PJT 173542 (P.G.M.); Ontario Research Fund grants RE09-011 and RE011-006 (B.A., C.B., and J.M.); Canadian Foundation for Innovation grant 39977 (C.B., J.M., and B.A.); McLaughlin Centre Accelerator grants MC-2022-02 and MC-2024-08-02 (B.A., C.B., and J.M.); NSERC Discovery Grant RGPIN-2020-04180 (P.G.M.); National Science Foundation grant MCB1818293 (C.L.M.); German Research Foundation grant DFG Bi 2086/1-1 (M.B.); NIH/NCI Ruth L. Kirschstein National Research F30 Award 5F30CA257227 (K.L.); and U. Minnesota Doctoral Dissertation Fellowship (H.N.W., A.Z.H., and Y.L.). J.M. was a Tier 2 Canadian Research Chair in Functional Genetics and is the GlaxoSmithKline Chair in Genetics & Genome Biology at the Hospital for Sick Children and the University of Toronto. B.A. holds a Tier 1 Canada Research Chair in Systematic Genetics & Cell Biology. C.B. is the Banting & Best Distinguished Scholar and a CIFAR Fellow in the Fungal Kingdom: Threats & Opportunities program.

AUTHOR CONTRIBUTIONS

Conceptualization, B.A., C.B., M. Costanzo, J.M., and C.L.M.; methodology (cell line construction, analysis, and screening), K.S.C., A.H.Y.T., J.v.L., M.A., K.A.L., B.M., P.M., S.N.M., M.A.U., S.M.T.A., K.A., U.B., S.B., X.C., J.J. Caumanns, M. Chandrashekhar, R.C., K.D., A.D., R.G., A.G.F., A.H., K.K., F.J., S.Y.L., W.L., H.J.L., B.N., A.N., N.M., L.N., M.S.R., M.S., A.S., E. Shuteriqi, O.S., D.T.T., M.T., D.T., J.T., S.V., K.E.W., Z.Y.W., J.W., Y.X.X., S.J.D., H.D.M.W., and T.X.; methodology (qGI score development), M.B., M.R., H.N.W., X.Z., A.Z.H., M. Costanzo, and C.L.M.; investigation (network analysis), M.B., M. Costanzo, X.Z., A.Z.H., M.R., K.R.B., C.P., H.N.W., C.R., D.T.F., Y.L., M.U., N.B., D.C., I.H., K.L., X.L., T.R., E. Schultz, W.W., H.L.R., and G.D.B.; investigation (follow-up biology), C.B., A.F.R., N.E.S., G.T., J.J. Chalmers, J.I.R.E., D.K.K., M. Maier, M. Mokhtaridoost, T.U., P.G.M., B.R., G.W.B., B.F.C., F.P.R., R.L., N.G.D., S.Y.L., and M. Costanzo; visualization, M.B., M. Costanzo, A.Z.H., C.R., M.R., H.N.W., and X.Z.; funding acquisition, B.A., C.B., J.M., and C.L.M.; supervision, B.A., C.B., J.M., and C.L.M.; writing—original draft, M. Costanzo, C.B., and C.L.M.

DECLARATION OF INTERESTS

The authors declare no competing interests.

STAR★METHODS

Detailed methods are provided in the online version of this paper and include the following:

- KEY RESOURCES TABLE
- EXPERIMENTAL MODEL AND STUDY PARTICIPANT DETAILS
  - Human Cell lines
  - *Saccharomyces cerevisiae* strains
- METHOD DETAILS
  - General information about the datasets
  - TKOv3 library, query mutant cell lines and genome-wide CRISPR screens
  - HAP1 single mutant fitness effects and essential genes
  - A quantitative genetic interaction (qGI) score
  - Estimating reproducibility of genetic interactions
  - Validating genetic interactions with an independent gRNA library
  - Hierarchical clustering of HAP1 genetic interaction profiles
  - Constructing a genetic interaction profile similarity network
  - Using the HAP1 interaction profile similarity network to annotate function
  - Genetic interaction degree and network density analysis
  - Genetic interactions involving paralogs
  - Overlap of genetic interactions with other genomic datasets
  - Precision-recall analysis
  - Genetic interactions within and between protein complexes
  - A genetic interaction profile similarity-derived functional hierarchy
  - Genetic Suppression Analysis
  - Genetic interaction conservation
  - Follow-up Experiments
  - Analysis of genetic interactions underlying cancer gene dependencies
- COMPARING GENETIC INTERACTION AND CO-ESSENTIALITY NETWORKS
  - Jaccard network overlap analysis
- ESTIMATING SIZE OF A COMPLETE HAP1 GENETIC INTERACTION NETWORK
  - Total number of genetic interactions
  - Extreme synthetic lethal and suppressor interactions
- QUANTIFICATION AND STATISTICAL ANALYSIS
- ADDITIONAL RESOURCES

SUPPLEMENTAL INFORMATION

Supplemental information can be found online at https://doi.org/10.1016/j.cell.2026.03.044.

Received: November 25, 2025
Revised: January 29, 2026
Accepted: March 24, 2026

REFERENCES

1. Costanzo, M., Kuzmin, E., van Leeuwen, J., Mair, B., Moffat, J., Boone, C., and Andrews, B. (2019). Global Genetic Networks and the Genotype-to-Phenotype Relationship. Cell *177*, 85–100. https://doi.org/10.1016/j.cell.2019.01.033.

2. Tong, A.H., Evangelista, M., Parsons, A.B., Xu, H., Bader, G.D., Pagé, N., Robinson, M., Raghibizadeh, S., Hogue, C.W., Bussey, H., et al. (2001). Systematic genetic analysis with ordered arrays of yeast deletion mutants. Science *294*, 2364–2368. https://doi.org/10.1126/science.1065810.

3. Tong, A.H.Y., Lesage, G., Bader, G.D., Ding, H., Xu, H., Xin, X., Young, J., Berriz, G.F., Brost, R.L., Chang, M., et al. (2004). Global mapping of the yeast genetic interaction network. Science *303*, 808–813. https://doi.org/10.1126/science.1091317.

4. Costanzo, M., Baryshnikova, A., Bellay, J., Kim, Y., Spear, E.D., Sevier, C.S., Ding, H., Koh, J.L.Y., Toufighi, K., Mostafavi, S., et al. (2010). The genetic landscape of a cell. Science *327*, 425–431. https://doi.org/10.1126/science.1180823.

5. Costanzo, M., VanderSluis, B., Koch, E.N., Baryshnikova, A., Pons, C., Tan, G., Wang, W., Usaj, M., Hanchard, J., Lee, S.D., et al. (2016). A global genetic interaction network maps a wiring diagram of cellular function. Science *353*, aaf1420. https://doi.org/10.1126/science.aaf1420.

6. Blomen, V.A., Májek, P., Jae, L.T., Bigenzahn, J.W., Nieuwenhuis, J., Staring, J., Sacco, R., van Diemen, F.R., Olk, N., Stukalov, A., et al. (2015). Gene essentiality and synthetic lethality in haploid human cells. Science *350*, 1092–1096. https://doi.org/10.1126/science.aac7557.

7. Hart, T., Chandrashekhar, M., Aregger, M., Steinhart, Z., Brown, K.R., MacLeod, G., Mis, M., Zimmermann, M., Fradet-Turcotte, A., Sun, S., et al. (2015). High-Resolution CRISPR Screens Reveal Fitness Genes and Genotype-Specific Cancer Liabilities. Cell *163*, 1515–1526. https://doi.org/10.1016/j.cell.2015.11.015.

8. Wang, T., Birsoy, K., Hughes, N.W., Krupczak, K.M., Post, Y., Wei, J.J., Lander, E.S., and Sabatini, D.M. (2015). Identification and characterization of essential genes in the human genome. Science *350*, 1096–1101. https://doi.org/10.1126/science.aac7041.

9. Broad, D. (2018) DepMap Achilles 18Q4 Public. https://doi.org/10.6084/m9.figshare.7270880.v1.

10. Tsherniak, A., Vazquez, F., Montgomery, P.G., Weir, B.A., Kryukov, G., Cowley, G.S., Gill, S., Harrington, W.F., Pantel, S., Krill-Burger, J.M., et al. (2017). Defining a Cancer Dependency Map. Cell *170*, 564–576.e16. https://doi.org/10.1016/j.cell.2017.06.010.

11. Rauscher, B., Heigwer, F., Henkel, L., Hielscher, T., Voloshanenko, O., and Boutros, M. (2018). Toward an integrated map of genetic interactions in cancer cells. Mol. Syst. Biol. *14*, e7656. https://doi.org/10.15252/msb.20177656.

12. Meyers, R.M., Bryan, J.G., McFarland, J.M., Weir, B.A., Sizemore, A.E., Xu, H., Dharia, N.V., Montgomery, P.G., Cowley, G.S., Pantel, S., et al. (2017). Computational correction of copy number effect improves specificity of CRISPR-Cas9 essentiality screens in cancer cells. Nat. Genet. *49*, 1779–1784. https://doi.org/10.1038/ng.3984.

13. Dempster, J.M., Boyle, I., Vazquez, F., Root, D.E., Boehm, J.S., Hahn, W.C., Tsherniak, A., and McFarland, J.M. (2021). Chronos: a cell population dynamics model of CRISPR experiments that improves inference of gene fitness effects. Genome Biol. *22*, 343. https://doi.org/10.1186/s13059-021-02540-7.

14. Pacini, C., Duncan, E., Gonçalves, E., Gilbert, J., Bhosle, S., Horswell, S., Karakoc, E., Lightfoot, H., Curry, E., Muyas, F., et al. (2024). A comprehensive clinically informed map of dependencies in cancer cells and framework for target prioritization. Cancer Cell *42*, 301–316.e9. https://doi.org/10.1016/j.ccell.2023.12.016.

15. Hartwell, L.H., Szankasi, P., Roberts, C.J., Murray, A.W., and Friend, S.H. (1997). Integrating genetic approaches into the discovery of anticancer drugs. Science *278*, 1064–1068. https://doi.org/10.1126/science.278.5340.1064.

16. Lord, C.J., Quinn, N., and Ryan, C.J. (2020). Integrative analysis of large-scale loss-of-function screens identifies robust cancer-associated genetic interactions. eLife *9*. https://doi.org/10.7554/eLife.58925.

17. Behan, F.M., Iorio, F., Picco, G., Gonçalves, E., Beaver, C.M., Migliardi, G., Santos, R., Rao, Y., Sassi, F., Pinnelli, M., et al. (2019). Prioritization of cancer therapeutic targets using CRISPR-Cas9 screens. Nature *568*, 511–516. https://doi.org/10.1038/s41586-019-1103-9.

18. McDonald, E.R., 3rd, de Weck, A., Schlabach, M.R., Billy, E., Mavrakis, K.J., Hoffman, G.R., Belur, D., Castelletti, D., Frias, E., Gampa, K., et al. (2017). Project DRIVE: A Compendium of Cancer Dependencies and Synthetic Lethal Relationships Uncovered by Large-Scale, Deep RNAi Screening. Cell *170*, 577–592.e10. https://doi.org/10.1016/j.cell.2017.07.005.

19. Dowell, R.D., Ryan, O., Jansen, A., Cheung, D., Agarwala, S., Danford, T., Bernstein, D.A., Rolfe, P.A., Heisler, L.E., Chin, B., et al. (2010). Genotype to phenotype: a complex problem. Science *328*, 469. https://doi.org/10.1126/science.1189015.

20. Hou, J., Tan, G., Fink, G.R., Andrews, B.J., and Boone, C. (2019). Complex modifier landscape underlying genetic background effects. Proc. Natl. Acad. Sci. USA *116*, 5045–5054. https://doi.org/10.1073/pnas.1820915116.

21. Edwards, M.D., Symbor-Nagrabska, A., Dollard, L., Gifford, D.K., and Fink, G.R. (2014). Interactions between chromosomal and nonchromosomal elements reveal missing heritability. Proc. Natl. Acad. Sci. USA *111*, 7719–7722. https://doi.org/10.1073/pnas.1407126111.

22. Wainberg, M., Kamber, R.A., Balsubramani, A., Meyers, R.M., Sinnott-Armstrong, N., Hornburg, D., Jiang, L., Chan, J., Jian, R., Gu, M., et al. (2021). A genome-wide atlas of co-essential modules assigns function to uncharacterized genes. Nat. Genet. *53*, 638–649. https://doi.org/10.1038/s41588-021-00840-z.

23. Kim, E., Dede, M., Lenoir, W.F., Wang, G., Srinivasan, S., Colic, M., and Hart, T. (2019). A network of human functional gene interactions from knockout fitness screens in cancer cells. Life Sci. Alliance *2*, e201800278. https://doi.org/10.26508/lsa.201800278.

24. Boyle, E.A., Pritchard, J.K., and Greenleaf, W.J. (2018). High-resolution mapping of cancer cell networks using co-functional interactions. Mol. Syst. Biol. *14*, e8594. https://doi.org/10.15252/msb.20188594.

25. Pan, J., Meyers, R.M., Michel, B.C., Mashtalir, N., Sizemore, A.E., Wells, J.N., Cassel, S.H., Vazquez, F., Weir, B.A., Hahn, W.C., et al. (2018). Interrogation of Mammalian Protein Complex Structure, Function, and Membership Using Genome-Scale Fitness Screens. Cell Syst. *6*, 555–568.e7. https://doi.org/10.1016/j.cels.2018.04.011.

26. Rahman, M., Billmann, M., Costanzo, M., Aregger, M., Tong, A.H.Y., Chan, K., Ward, H.N., Brown, K.R., Andrews, B.J., Boone, C., et al. (2021). A method for benchmarking genetic screens reveals a predominant mitochondrial bias. Mol. Syst. Biol. *17*, e10013. https://doi.org/10.15252/msb.202010013.

27. Bassik, M.C., Kampmann, M., Lebbink, R.J., Wang, S., Hein, M.Y., Poser, I., Weibezahn, J., Horlbeck, M.A., Chen, S., Mann, M., et al. (2013). A systematic Mammalian genetic interaction map reveals pathways underlying ricin susceptibility. Cell *152*, 909–922. https://doi.org/10.1016/j.cell.2013.01.030.

28. Shen, J.P., Zhao, D., Sasik, R., Luebeck, J., Birmingham, A., Bojorquez-Gomez, A., Licon, K., Klepper, K., Pekin, D., Beckett, A.N., et al. (2017). Combinatorial CRISPR-Cas9 screens for de novo mapping of genetic interactions. Nat. Methods *14*, 573–576. https://doi.org/10.1038/nmeth.4225.

29. Najm, F.J., Strand, C., Donovan, K.F., Hegde, M., Sanson, K.R., Vaimberg, E.W., Sullender, M.E., Hartenian, E., Kalani, Z., Fusi, N., et al. (2018). Orthologous CRISPR-Cas9 enzymes for combinatorial genetic screens. Nat. Biotechnol. *36*, 179–189. https://doi.org/10.1038/nbt.4048.

30. Han, K., Jeng, E.E., Hess, G.T., Morgens, D.W., Li, A., and Bassik, M.C. (2017). Synergistic drug combinations for cancer identified in a CRISPR screen for pairwise genetic interactions. Nat. Biotechnol. *35*, 463–474. https://doi.org/10.1038/nbt.3834.

31. Du, D., Roguev, A., Gordon, D.E., Chen, M., Chen, S.H., Shales, M., Shen, J.P., Ideker, T., Mali, P., Qi, L.S., et al. (2017). Genetic interaction mapping in mammalian cells using CRISPR interference. Nat. Methods *14*, 577–580. https://doi.org/10.1038/nmeth.4286.

32. Boettcher, M., Tian, R., Blau, J.A., Markegard, E., Wagner, R.T., Wu, D., Mo, X., Biton, A., Zaitlen, N., Fu, H., et al. (2018). Dual gene activation and knockout screen reveals directional dependencies in genetic networks. Nat. Biotechnol. *36*, 170–178. https://doi.org/10.1038/nbt.4062.

33. Wong, A.S.L., Choi, G.C.G., Cui, C.H., Pregernig, G., Milani, P., Adam, M., Perli, S.D., Kazer, S.W., Gaillard, A., Hermann, M., et al. (2016). Multiplexed barcoded CRISPR-Cas9 screening enabled by CombiGEM. Proc. Natl. Acad. Sci. USA *113*, 2544–2549. https://doi.org/10.1073/pnas.1517883113.

34. Esmaeili Anvar, N., Lin, C., Ma, X., Wilson, L.L., Steger, R., Sangree, A.K., Colic, M., Wang, S.H., Doench, J.G., and Hart, T. (2024). Efficient gene knockout and genetic interaction screening using the in4mer CRISPR/Cas12a multiplex knockout platform. Nat. Commun. *15*, 3577. https://doi.org/10.1038/s41467-024-47795-3.

35. Gonatopoulos-Pournatzis, T., Aregger, M., Brown, K.R., Farhangmehr, S., Braunschweig, U., Ward, H.N., Ha, K.C.H., Weiss, A., Billmann, M., Durbic, T., et al. (2020). Genetic interaction mapping and exon-resolution functional genomics with a hybrid Cas9-Cas12a platform. Nat. Biotechnol. *38*, 638–648. https://doi.org/10.1038/s41587-020-0437-z.

36. DeWeirdt, P.C., Sanson, K.R., Sangree, A.K., Hegde, M., Hanna, R.E., Feeley, M.N., Griffith, A.L., Teng, T., Borys, S.M., Strand, C., et al. (2021). Optimization of AsCas12a for combinatorial genetic screens in human cells. Nat. Biotechnol. *39*, 94–104. https://doi.org/10.1038/s41587-020-0600-6.

37. DeWeirdt, P.C., Sangree, A.K., Hanna, R.E., Sanson, K.R., Hegde, M., Strand, C., Persky, N.S., and Doench, J.G. (2020). Genetic screens in isogenic mammalian cell lines without single cell cloning. Nat. Commun. *11*, 752. https://doi.org/10.1038/s41467-020-14620-6.

38. Shalem, O., Sanjana, N.E., Hartenian, E., Shi, X., Scott, D.A., Mikkelson, T., Heckl, D., Ebert, B.L., Root, D.E., Doench, J.G., et al. (2013). Genome-Scale CRISPR-Cas9 Knockout Screening in Human Cells. Science *343*, 84–87. https://doi.org/10.1126/science.1247005.

39. Thompson, N.A., Ranzani, M., van der Weyden, L., Iyer, V., Offord, V., Droop, A., Behan, F., Gonçalves, E., Speak, A., Iorio, F., et al. (2021). Combinatorial CRISPR screen identifies fitness effects of gene paralogues. Nat. Commun. *12*, 1302. https://doi.org/10.1038/s41467-021-21478-9.

40. Wolf, G., Leippe, P., Onstein, S., Goldmann, U., Frommelt, F., Teoh, S.T., Girardi, E., Wiedmer, T., and Superti-Furga, G. (2025). The genetic interaction map of the human solute carrier superfamily. Mol. Syst. Biol. *21*, 531–559. https://doi.org/10.1038/s44320-025-00105-5.

41. Fielden, J., Siegner, S.M., Gallagher, D.N., Schröder, M.S., Dello Stritto, M.R., Lam, S., Kobel, L., Schlapansky, M.F., Jackson, S.P., Cejka, P., et al. (2025). Comprehensive interrogation of synthetic lethality in the DNA damage response. Nature *640*, 1093–1102. https://doi.org/10.1038/s41586-025-08815-4.

42. Horlbeck, M.A., Xu, A., Wang, M., Bennett, N.K., Park, C.Y., Bogdanoff, D., Adamson, B., Chow, E.D., Kampmann, M., Peterson, T.R., et al. (2018). Mapping the Genetic Landscape of Human Cells. Cell *174*, 953–967.e22. https://doi.org/10.1016/j.cell.2018.06.010.

43. Burgold, T., Karakoc, E., Gonçalves, E., Dwane, L., Barrio-Hernandez, I., Silva, R.O., Souster, E., Sharma, M., Beck, A., Koh, G., et al. (2025). Genetic interaction library screening with a next-generation dual guide CRISPR system. Nat. Commun. *17*, 561. https://doi.org/10.1038/s41467-025-67256-9.

44. Vizeacoumar, F.J., Arnold, R., Vizeacoumar, F.S., Chandrashekhar, M., Buzina, A., Young, J.T.F., Kwan, J.H.M., Sayad, A., Mero, P., Lawo, S., et al. (2013). A negative genetic interaction map in isogenic cancer cell lines reveals cancer cell vulnerabilities. Mol. Syst. Biol. *9*, 696. https://doi.org/10.1038/msb.2013.54.

45. Varland, S., Silva, R.D., Kjosås, I., Faustino, A., Bogaert, A., Billmann, M., Boukhatmi, H., Kellen, B., Costanzo, M., Drazic, A., et al. (2023). N-terminal acetylation shields proteins from degradation and promotes age-dependent motility and longevity. Nat. Commun. *14*, 6774. https://doi.org/10.1038/s41467-023-42342-y.

46. Aregger, M., Lawson, K.A., Billmann, M., Costanzo, M., Tong, A.H.Y., Chan, K., Rahman, M., Brown, K.R., Ross, C., Usaj, M., et al. (2020). Systematic mapping of genetic interactions for de novo fatty acid synthesis identifies C12orf49 as a regulator of lipid metabolism. Nat. Metab. *2*, 499–513. https://doi.org/10.1038/s42255-020-0211-z.

47. Stok, C., Tsaridou, S., van den Tempel, N., Everts, M., Wierenga, E., Bakker, F.J., Kok, Y., Alves, I.T., Jae, L.T., Raas, M.W.D., et al. (2023). FIRRM/C1orf112 is synthetic lethal with PICH and mediates RAD51 dynamics. Cell Rep. *42*, 112668. https://doi.org/10.1016/j.celrep.2023.112668.

48. Bürckstümmer, T., Banning, C., Hainzl, P., Schobesberger, R., Kerzendorfer, C., Pauler, F.M., Chen, D., Them, N., Schischlik, F., Rebsamen, M., et al. (2013). A reversible gene trap collection empowers haploid genetics in human cells. Nat. Methods *10*, 965–971. https://doi.org/10.1038/nmeth.2609.

49. Essletzbichler, P., Konopka, T., Santoro, F., Chen, D., Gapp, B.V., Kralovics, R., Brummelkamp, T.R., Nijman, S.M.B., and Bürckstümmer, T. (2014). Megabase-scale deletion using CRISPR/Cas9 to generate a fully haploid human cell line. Genome Res. *24*, 2059–2065. https://doi.org/10.1101/gr.177220.114.

50. Carette, J.E., Guimaraes, C.P., Varadarajan, M., Park, A.S., Wuethrich, I., Godarova, A., Kotecki, M., Cochran, B.H., Spooner, E., Ploegh, H.L., et al. (2009). Haploid genetic screens in human cells identify host factors used by pathogens. Science *326*, 1231–1235. https://doi.org/10.1126/science.1178955.

51. Hart, T., Tong, A.H.Y., Chan, K., Van Leeuwen, J., Seetharaman, A., Aregger, M., Chandrashekhar, M., Hustedt, N., Seth, S., Noonan, A., et al. (2017). Evaluation and Design of Genome-Wide CRISPR/SpCas9 Knockout Screens. G3 (Bethesda) *7*, 2719–2727. https://doi.org/10.1534/g3.117.041277.

52. Billmann, M., Costanzo, M., Rahman, M., Chan, K., Yan Tong, A.H., Ward, H.N., Hassan, A.Z., Zhang, X., Brown, K.R., Rohde, T., et al. (2026). Quantitative analysis of genetic interactions in human cells from genome-wide CRISPR-Cas9 screens. Preprint at bioRxiv. https://doi.org/10.1101/2025.06.30.662330.

53. Wang, T., Yu, H., Hughes, N.W., Liu, B., Kendirli, A., Klein, K., Chen, W.W., Lander, E.S., and Sabatini, D.M. (2017). Gene Essentiality Profiling Reveals Gene Networks and Synthetic Lethal Interactions with Oncogenic Ras. Cell *168*, 890–903.e15. https://doi.org/10.1016/j.cell.2017.01.013.

54. Winzeler, E.A., Shoemaker, D.D., Astromoff, A., Liang, H., Anderson, K., Andre, B., Bangham, R., Benito, R., Boeke, J.D., Bussey, H., et al. (1999). Functional characterization of the S. cerevisiae genome by gene deletion and parallel analysis. Science *285*, 901–906. https://doi.org/10.1126/science.285.5429.901.

55. Hirsh, A.E., and Fraser, H.B. (2001). Protein dispensability and rate of evolution. Nature *411*, 1046–1049. https://doi.org/10.1038/35082561.

56. Kim, D.U., Hayles, J., Kim, D., Wood, V., Park, H.O., Won, M., Yoo, H.S., Duhig, T., Nam, M., Palmer, G., et al. (2010). Analysis of a genome-wide set of gene deletions in the fission yeast Schizosaccharomyces pombe. Nat. Biotechnol. *28*, 617–623. https://doi.org/10.1038/nbt.1628.

57. Costanzo, M., Hou, J., Messier, V., Nelson, J., Rahman, M., VanderSluis, B., Wang, W., Pons, C., Ross, C., Ušaj, M., et al. (2021). Environmental robustness of the global yeast genetic interaction network. Science *372*, eabf8424. https://doi.org/10.1126/science.abf8424.

58. Smits, A.H., Ziebell, F., Joberty, G., Zinn, N., Mueller, W.F., Clauder-Münster, S., Eberhard, D., Fälth Savitski, M., Grandi, P., Jakob, P., et al. (2019). Biological plasticity rescues target activity in CRISPR knock

outs. Nat. Methods *16*, 1087–1093. https://doi.org/10.1038/s41592-019-0614-5.

59. Shirakawa, R., Goto-Ito, S., Goto, K., Wakayama, S., Kubo, H., Sakata, N., Trinh, D.A., Yamagata, A., Sato, Y., Masumoto, H., et al. (2020). A SNARE geranylgeranyltransferase essential for the organization of the Golgi apparatus. EMBO J. *39*, e104120. https://doi.org/10.15252/embj.2019104120.

60. Baryshnikova, A., Costanzo, M., Kim, Y., Ding, H., Koh, J., Toufighi, K., Youn, J.Y., Ou, J., San Luis, B.J., Bandyopadhyay, S., et al. (2010). Quantitative analysis of fitness and genetic interactions in yeast on a genome scale. Nat. Methods *7*, 1017–1024. https://doi.org/10.1038/nmeth.1534.

61. Baryshnikova, A. (2016). Systematic Functional Annotation and Visualization of Biological Networks. Cell Syst. *2*, 412–421. https://doi.org/10.1016/j.cels.2016.04.014.

62. Binder, J.X., Pletscher-Frankild, S., Tsafou, K., Stolte, C., O'Donoghue, S.I., Schneider, R., and Jensen, L.J. (2014). COMPARTMENTS: unification and visualization of protein subcellular localization evidence. Database (Oxford) *2014*, bau012. https://doi.org/10.1093/database/bau012.

63. Usaj, M., Tan, Y., Wang, W., VanderSluis, B., Zou, A., Myers, C.L., Costanzo, M., Andrews, B., and Boone, C. (2017). TheCellMap.org: A Web-Accessible Database for Visualizing and Mining the Global Yeast Genetic Interaction Network. G3 (Bethesda) *7*, 1539–1549. https://doi.org/10.1534/g3.117.040220.

64. Horecka, I., Ušaj, M., Masinas, M.P.D., Ward, H.N., Zhang, X., Hassan, A.Z., Billmann, M., Röst, H.L., Myers, C.L., Costanzo, M., Andrews, B., Boone, C. (2026). Expanding TheCellMap.org to visualize a genome-scale genetic interaction network for a human cell line. Preprint at bioRxiv. https://doi.org/10.64898/2026.03.16.712129.

65. Shannon, P., Markiel, A., Ozier, O., Baliga, N.S., Wang, J.T., Ramage, D., Amin, N., Schwikowski, B., and Ideker, T. (2003). Cytoscape: a software environment for integrated models of biomolecular interaction networks. Genome Res. *13*, 2498–2504. https://doi.org/10.1101/gr.1239303.

66. Tsitsiridis, G., Steinkamp, R., Giurgiu, M., Brauner, B., Fobo, G., Frishman, G., Montrone, C., and Ruepp, A. (2023). CORUM: the comprehensive resource of mammalian protein complexes–2022. Nucleic Acids Res. *51*, D539–D545. https://doi.org/10.1093/nar/gkac1015.

67. Piotrowski, J.S., Li, S.C., Deshpande, R., Simpkins, S.W., Nelson, J., Yashiroda, Y., Barber, J.M., Safizadeh, H., Wilson, E., Okada, H., et al. (2017). Functional annotation of chemical libraries across diverse biological processes. Nat. Chem. Biol. *13*, 982–993. https://doi.org/10.1038/nchembio.2436.

68. Liebeskind, B.J., McWhite, C.D., and Marcotte, E.M. (2016). Towards Consensus Gene Ages. Genome Biol. Evol. *8*, 1812–1823. https://doi.org/10.1093/gbe/evw113.

69. Koch, E.N., Costanzo, M., Bellay, J., Deshpande, R., Chatfield-Reed, K., Chua, G., D'Urso, G., Andrews, B.J., Boone, C., and Myers, C.L. (2012). Conserved rules govern genetic interaction degree across species. Genome Biol. *13*, R57. https://doi.org/10.1186/gb-2012-13-7-r57.

70. Mokhtaridoost, M., Chalmers, J.J., Soleimanpoor, M., McMurray, B.J., Lato, D.F., Nguyen, S.C., Musienko, V., Nash, J.O., Espeso-Gil, S., Ahmed, S., et al. (2024). Inter-chromosomal contacts demarcate genome topology along a spatial gradient. Nat. Commun. *15*, 9813. https://doi.org/10.1038/s41467-024-53983-y.

71. Kuzmin, E., VanderSluis, B., Nguyen Ba, A.N., Wang, W., Koch, E.N., Usaj, M., Khmelinskii, A., Usaj, M.M., van Leeuwen, J., Kraus, O., et al. (2020). Exploring whole-genome duplicate gene retention with complex genetic interaction analysis. Science *368*, eaaz5667. https://doi.org/10.1126/science.aaz5667.

72. VanderSluis, B., Bellay, J., Musso, G., Costanzo, M., Papp, B., Vizeacoumar, F.J., Baryshnikova, A., Andrews, B., Boone, C., and Myers, C.L. (2010). Genetic interactions reveal the evolutionary trajectories of duplicate genes. Mol. Syst. Biol. *6*, 429. https://doi.org/10.1038/msb.2010.82.

73. Musso, G., Costanzo, M., Huangfu, M., Smith, A.M., Paw, J., San Luis, B.J., Boone, C., Giaever, G., Nislow, C., Emili, A., et al. (2008). The extensive and condition-dependent nature of epistasis among whole-genome duplicates in yeast. Genome Res. *18*, 1092–1099. https://doi.org/10.1101/gr.076174.108.

74. Dean, E.J., Davis, J.C., Davis, R.W., and Petrov, D.A. (2008). Pervasive and persistent redundancy among duplicated genes in yeast. PLoS Genet. *4*, e1000113. https://doi.org/10.1371/journal.pgen.1000113.

75. DeLuna, A., Vetsigian, K., Shoresh, N., Hegreness, M., Colón-González, M., Chao, S., and Kishony, R. (2008). Exposing the fitness contribution of duplicated genes. Nat. Genet. *40*, 676–681. https://doi.org/10.1038/ng.123.

76. De Kegel, B., and Ryan, C.J. (2019). Paralog buffering contributes to the variable essentiality of genes in cancer cell lines. PLoS Genet. *15*, e1008466. https://doi.org/10.1371/journal.pgen.1008466.

77. Flister, M.J., Verduzco, D., Petiwala, S., Carneiro-Lobo, T.C., Ghekas, C., Shi, X., Lu, C., and Dezso, Z. (2025). Genetic Mapping and predictive modeling of paralog synthetic lethality. Cell Rep. *44*, 116512. https://doi.org/10.1016/j.celrep.2025.116512.

78. VanderSluis, B., Costanzo, M., Billmann, M., Ward, H.N., Myers, C.L., Andrews, B.J., and Boone, C. (2018). Integrating genetic and protein-protein interaction networks maps a functional wiring diagram of a cell. Curr. Opin. Microbiol. *45*, 170–179. https://doi.org/10.1016/j.mib.2018.06.004.

79. Yu, I.M., and Hughson, F.M. (2010). Tethering factors as organizers of intracellular vesicular traffic. Annu. Rev. Cell Dev. Biol. *26*, 137–156. https://doi.org/10.1146/annurev.cellbio.042308.113327.

80. Carosi, J.M., Denton, D., Kumar, S., and Sargeant, T.J. (2023). Receptor Recycling by Retromer. Mol. Cell. Biol. *43*, 317–334. https://doi.org/10.1080/10985549.2023.2222053.

81. Prindle, V., Richardson, A.E., Sher, K.R., Kongpachith, S., Kentala, K., Petiwala, S., Cheng, D., Widomski, D., Le, P., Torrent, M., et al. (2025). Synthetic lethality of mRNA quality control complexes in cancer. Nature *638*, 1095–1103. https://doi.org/10.1038/s41586-024-08398-6.

82. Borck, P.C., Boyle, I., Jankovic, K., Bick, N., Foster, K., Lau, A.C., Parker-Burns, L.I., Lubicki, D.A., Li, T., Borah, A.A., et al. (2025). SKI complex loss renders 9p21.3-deleted or MSI-H cancers dependent on PELO. Nature *638*, 1104–1111. https://doi.org/10.1038/s41586-024-08509-3.

83. Fröhlich, F., Petit, C., Kory, N., Christiano, R., Hannibal-Bach, H.K., Graham, M., Liu, X., Ejsing, C.S., Farese, R.V., and Walther, T.C. (2015). The GARP complex is required for cellular sphingolipid homeostasis. eLife *4*. https://doi.org/10.7554/eLife.08712.

84. Wei, J., Zhang, Y.Y., Luo, J., Wang, J.Q., Zhou, Y.X., Miao, H.H., Shi, X.J., Qu, Y.X., Xu, J., Li, B.L., et al. (2017). The GARP Complex Is Involved in Intracellular Cholesterol Transport via Targeting NPC2 to Lysosomes. Cell Rep. *19*, 2823–2835. https://doi.org/10.1016/j.celrep.2017.06.012.

85. Petit, C.S., Lee, J.J., Boland, S., Swarup, S., Christiano, R., Lai, Z.W., Mejhert, N., Elliott, S.D., McFall, D., Haque, S., et al. (2020). Inhibition of sphingolipid synthesis improves outcomes and survival in GARP mutant wobbler mice, a model of motor neuron degeneration. Proc. Natl. Acad. Sci. USA *117*, 10565–10574. https://doi.org/10.1073/pnas.1913956117.

86. Vanier, M.T., and Millat, G. (2003). Niemann-Pick disease type C. Clin. Genet. *64*, 269–281. https://doi.org/10.1034/j.1399-0004.2003.00147.x.

87. Vanier, M.T. (2010). Niemann-Pick disease type C. Orphanet J. Rare Dis. *5*, 16. https://doi.org/10.1186/1750-1172-5-16.

88. Gershlick, D.C., Ishida, M., Jones, J.R., Bellomo, A., Bonifacino, J.S., and Everman, D.B. (2019). A neurodevelopmental disorder caused by mutations in the VPS51 subunit of the GARP and EARP complexes. Hum. Mol. Genet. *28*, 1548–1560. https://doi.org/10.1093/hmg/ddy423.

89. Feinstein, M., Flusser, H., Lerman-Sagie, T., Ben-Zeev, B., Lev, D., Agamy, O., Cohen, I., Kadir, R., Sivan, S., Leshinsky-Silver, E., et al. (2014). VPS53 mutations cause progressive cerebello-cerebral atrophy

type 2 (PCCA2). J. Med. Genet. *51*, 303–308. https://doi.org/10.1136/jmedgenet-2013-101823.

90. Pérez-Victoria, F.J., Abascal-Palacios, G., Tascón, I., Kajava, A., Magadán, J.G., Pioro, E.P., Bonifacino, J.S., and Hierro, A. (2010). Structural basis for the wobbler mouse neurodegenerative disorder caused by mutation in the Vps54 subunit of the GARP complex. Proc. Natl. Acad. Sci. USA *107*, 12860–12865. https://doi.org/10.1073/pnas.1004756107.
91. van Leeuwen, J., Pons, C., Tan, G., Wang, Z.Y., Hou, J., Weile, J., Gebbia, M., Liang, W., Shuteriqi, E., Li, Z., et al. (2020). Systematic analysis of bypass suppression of essential genes. Mol. Syst. Biol. *16*, e9828. https://doi.org/10.15252/msb.20209828.
92. van Leeuwen, J., Pons, C., Mellor, J.C., Yamaguchi, T.N., Friesen, H., Koschwanez, J., Ušaj, M.M., Pechlaner, M., Takar, M., Ušaj, M., et al. (2016). Exploring genetic suppression interactions on a global scale. Science *354*, aag0839. https://doi.org/10.1126/science.aag0839.
93. Masud, S.N., Srivastava, A., Mero, P., Echezarreta, V.S., Anderson, E., van Buren, L., Wei, J., Taylor, D.T., Farias, A.G., Mikolajewicz, N., et al. (2025). Genetic suppression features ABHD18 as a Barth syndrome therapeutic target. Nature *645*, 1029–1038. https://doi.org/10.1038/s41586-025-09373-5.
94. Ünlü, B., Pons, C., Ho, U.L., Batté, A., Aloy, P., and van Leeuwen, J. (2023). Global analysis of suppressor mutations that rescue human genetic defects. Genome Med. *15*, 78. https://doi.org/10.1186/s13073-023-01232-0.
95. Zinman, G.E., Zhong, S., and Bar-Joseph, Z. (2011). Biological interaction networks are conserved at the module level. BMC Syst. Biol. *5*, 134. https://doi.org/10.1186/1752-0509-5-134.
96. Dixon, S.J., Fedyshyn, Y., Koh, J.L.Y., Prasad, T.S.K., Chahwan, C., Chua, G., Toufighi, K., Baryshnikova, A., Hayles, J., Hoe, K.L., et al. (2008). Significant conservation of synthetic lethal genetic interaction networks between distantly related eukaryotes. Proc. Natl. Acad. Sci. USA *105*, 16653–16658. https://doi.org/10.1073/pnas.0806261105.
97. Frost, A., Elgort, M.G., Brandman, O., Ives, C., Collins, S.R., Miller-Vedam, L., Weibezahn, J., Hein, M.Y., Poser, I., Mann, M., et al. (2012). Functional repurposing revealed by comparing S. pombe and S. cerevisiae genetic interactions. Cell *149*, 1339–1352. https://doi.org/10.1016/j.cell.2012.04.028.
98. Ryan, C.J., Roguev, A., Patrick, K., Xu, J., Jahari, H., Tong, Z., Beltrao, P., Shales, M., Qu, H., Collins, S.R., et al. (2012). Hierarchical modularity and the evolution of genetic interactomes across species. Mol. Cell *46*, 691–704. https://doi.org/10.1016/j.molcel.2012.05.028.
99. Kapitzky, L., Beltrao, P., Berens, T.J., Gassner, N., Zhou, C., Wüster, A., Wu, J., Babu, M.M., Elledge, S.J., Toczyski, D., et al. (2010). Cross-species chemogenomic profiling reveals evolutionarily conserved drug mode of action. Mol. Syst. Biol. *6*, 451. https://doi.org/10.1038/msb.2010.107.
100. Kuchay, S., Wang, H., Marzio, A., Jain, K., Homer, H., Fehrenbacher, N., Philips, M.R., Zheng, N., and Pagano, M. (2019). GGTase3 is a newly identified geranylgeranyltransferase targeting a ubiquitin ligase. Nat. Struct. Mol. Biol. *26*, 628–636. https://doi.org/10.1038/s41594-019-0249-3.
101. Sakata, N., Shirakawa, R., Goto, K., Trinh, D.A., and Horiuchi, H. (2021). Double prenylation of SNARE protein Ykt6 is required for lysosomal hydrolase trafficking. J. Biochem. *169*, 363–370. https://doi.org/10.1093/jb/mvaa111.
102. Tateishi, M., Goto, K., Hishinuma, E., Matsukawa, N., Kishimoto, T., Tanaka, K., Horiuchi, H., Fukasawa, M., and Shirakawa, R. (2025). Double prenylation of budding yeast Ykt6 regulates cell wall integrity and autophagy. J. Biol. Chem. *301*, 108384. https://doi.org/10.1016/j.jbc.2025.108384.
103. Hu, Y., Flockhart, I., Vinayagam, A., Bergwitz, C., Berger, B., Perrimon, N., and Mohr, S.E. (2011). An integrative approach to ortholog prediction for disease-focused and other functional studies. BMC Bioinform. *12*, 357. https://doi.org/10.1186/1471-2105-12-357.
104. Thomas, P.D., Ebert, D., Muruganujan, A., Mushayahama, T., Albou, L.P., and Mi, H. (2022). PANTHER: Making genome-scale phylogenetics accessible to all. Protein Sci. *31*, 8–22. https://doi.org/10.1002/pro.4218.
105. Lin, D.T.S., and Conibear, E. (2015). ABHD17 proteins are novel protein depalmitoylases that regulate N-Ras palmitate turnover and subcellular localization. eLife *4*, e11306. https://doi.org/10.7554/eLife.11306.
106. Roth, A.F., and Davis, N.G. (2020). Geranylgeranyl generosity: a new prenyl-transferase gives a fat to a SNARE protein. EMBO J. *39*, e104744. https://doi.org/10.15252/embj.2020104744.
107. Remsberg, J.R., Suciu, R.M., Zambetti, N.A., Hanigan, T.W., Firestone, A.J., Inguva, A., Long, A., Ngo, N., Lum, K.M., Henry, C.L., et al. (2021). ABHD17 regulation of plasma membrane palmitoylation and N-Ras-dependent cancer growth. Nat. Chem. Biol. *17*, 856–864. https://doi.org/10.1038/s41589-021-00785-8.
108. Lai, C.Y., Liu, H., Tin, K.X., Huang, Y., Yeh, K.H., Peng, H.W., Chen, H.D., He, J.Y., Chiang, Y.J., Liu, C.S., et al. (2019). Identification of UAP1L1 as a critical factor for protein O-GlcNAcylation and cell proliferation in human hepatoma cells. Oncogene *38*, 317–331. https://doi.org/10.1038/s41388-018-0442-6.
109. Mio, T., Yabe, T., Arisawa, M., and Yamada-Okabe, H. (1998). The eukaryotic UDP-N-acetylglucosamine pyrophosphorylases. Gene cloning, protein expression, and catalytic mechanism. J. Biol. Chem. *273*, 14392–14397. https://doi.org/10.1074/jbc.273.23.14392.
110. Healy, M.D., Hospenthal, M.K., Hall, R.J., Chandra, M., Chilton, M., Tillu, V., Chen, K.E., Celligoi, D.J., McDonald, F.J., Cullen, P.J., et al. (2018). Structural insights into the architecture and membrane interactions of the conserved COMMD proteins. eLife *7*, e35898. https://doi.org/10.7554/eLife.35898.
111. Sternlicht, H., Farr, G.W., Sternlicht, M.L., Driscoll, J.K., Willison, K., and Yaffe, M.B. (1993). The t-complex polypeptide 1 complex is a chaperonin for tubulin and actin in vivo. Proc. Natl. Acad. Sci. USA *90*, 9422–9426. https://doi.org/10.1073/pnas.90.20.9422.
112. Tahmaz, I., Shahmoradi Ghahe, S., and Topf, U. (2021). Prefoldin Function in Cellular Protein Homeostasis and Human Diseases. Front. Cell Dev. Biol. *9*, 816214. https://doi.org/10.3389/fcell.2021.816214.
113. Hassan, A.Z., Ward, H.N., Rahman, M., Billmann, M., Lee, Y., and Myers, C.L. (2023). Dimensionality reduction methods for extracting functional networks from large-scale CRISPR screens. Mol. Syst. Biol. *19*, e11657. https://doi.org/10.15252/msb.202311657.
114. Forster, D.T., Li, S.C., Yashiroda, Y., Yoshimura, M., Li, Z., Isuhuaylas, L.A.V., Itto-Nakama, K., Yamanaka, D., Ohya, Y., Osada, H., et al. (2022). BIONIC: biological network integration using convolutions. Nat. Methods *19*, 1250–1261. https://doi.org/10.1038/s41592-022-01616-x.
115. Kuzmin, E., VanderSluis, B., Wang, W., Tan, G., Deshpande, R., Chen, Y., Usaj, M., Balint, A., Mattiazzi Usaj, M., van Leeuwen, J., et al. (2018). Systematic analysis of complex genetic interactions. Science *360*. https://doi.org/10.1126/science.aao1729.
116. Hartman, J.L.T., Garvik, B., and Hartwell, L. (2001). Principles for the buffering of genetic variation. Science *291*, 1001–1004. https://doi.org/10.1126/science.1056072.
117. Hamosh, A., Scott, A.F., Amberger, J.S., Bocchini, C.A., and McKusick, V.A. (2005). Online Mendelian Inheritance in Man (OMIM), a knowledgebase of human genes and genetic disorders. Nucleic Acids Res. *33*, D514–D517. https://doi.org/10.1093/nar/gki033.
118. Fowler, D.M., Adams, D.J., Gloyn, A.L., Hahn, W.C., Marks, D.S., Muffley, L.A., Neal, J.T., Roth, F.P., Rubin, A.F., Starita, L.M., et al. (2023). An Atlas of Variant Effects to understand the genome at nucleotide resolution. Genome Biol. *24*, 147. https://doi.org/10.1186/s13059-023-02986-x.
119. Sondka, Z., Dhir, N.B., Carvalho-Silva, D., Jupe, S., Madhumita, M., McLaren, K., Starkey, M., Ward, S., Wilding, J., Ahmed, M., et al. (2023). COSMIC: a curated database of somatic variants and clinical

data for cancer. Nucleic Acids Res. *52*, D1210–D1217. https://doi.org/10.1093/nar/gkad986.

120. Ashworth, A., and Lord, C.J. (2018). Synthetic lethal therapies for cancer: what's next after PARP inhibitors? Nat. Rev. Clin. Oncol. *15*, 564–576. https://doi.org/10.1038/s41571-018-0055-6.

121. Lord, C.J., and Ashworth, A. (2017). PARP inhibitors: Synthetic lethality in the clinic. Science *355*, 1152–1158. https://doi.org/10.1126/science.aam7344.

122. Setton, J., Zinda, M., Riaz, N., Durocher, D., Zimmermann, M., Koehler, M., Reis-Filho, J.S., and Powell, S.N. (2021). Synthetic Lethality in Cancer Therapeutics: The Next Generation. Cancer Discov. *11*, 1626–1635. https://doi.org/10.1158/2159-8290.CD-20-1503.

123. Previtali, V., Bagnolini, G., Ciamarone, A., Ferrandi, G., Rinaldi, F., Myers, S.H., Roberti, M., and Cavalli, A. (2024). New Horizons of Synthetic Lethality in Cancer: Current Development and Future Perspectives. J. Med. Chem. *67*, 11488–11521. https://doi.org/10.1021/acs.jmedchem.4c00113.

124. Chen, R., Shi, L., Hakenberg, J., Naughton, B., Sklar, P., Zhang, J., Zhou, H., Tian, L., Prakash, O., Lemire, M., et al. (2016). Analysis of 589,306 genomes identifies individuals resilient to severe Mendelian childhood diseases. Nat. Biotechnol. *34*, 531–538. https://doi.org/10.1038/nbt.3514.

125. Prabhu, S., and Pe'er, I. (2012). Ultrafast genome-wide scan for SNP-SNP interactions in common complex disease. Genome Res. *22*, 2230–2240. https://doi.org/10.1101/gr.137885.112.

126. Mamtani, M., Anaya, J.M., He, W., and Ahuja, S.K. (2010). Association of copy number variation in the FCGR3B gene with risk of autoimmune diseases. Genes Immun. *11*, 155–160. https://doi.org/10.1038/gene.2009.71.

127. Cordell, H.J. (2009). Detecting gene-gene interactions that underlie human diseases. Nat. Rev. Genet. *10*, 392–404. https://doi.org/10.1038/nrg2579.

128. Martin, M.P., Gao, X., Lee, J.H., Nelson, G.W., Detels, R., Goedert, J.J., Buchbinder, S., Hoots, K., Vlahov, D., Trowsdale, J., et al. (2002). Epistatic interaction between KIR3DS1 and HLA-B delays the progression to AIDS. Nat. Genet. *31*, 429–434. https://doi.org/10.1038/ng934.

129. Eichler, E.E., Flint, J., Gibson, G., Kong, A., Leal, S.M., Moore, J.H., and Nadeau, J.H. (2010). Missing heritability and strategies for finding the underlying causes of complex disease. Nat. Rev. Genet. *11*, 446–450. https://doi.org/10.1038/nrg2809.

130. Zuk, O., Hechter, E., Sunyaev, S.R., and Lander, E.S. (2012). The mystery of missing heritability: Genetic interactions create phantom heritability. Proc. Natl. Acad. Sci. USA *109*, 1193–1198. https://doi.org/10.1073/pnas.1119675109.

131. Greene, C.S., Penrod, N.M., Williams, S.M., and Moore, J.H. (2009). Failure to replicate a genetic association may provide important clues about genetic architecture. PLoS One *4*, e5639. https://doi.org/10.1371/journal.pone.0005639.

132. de Cid, R., Riveira-Munoz, E., Zeeuwen, P.L.J.M., Robarge, J., Liao, W., Dannhauser, E.N., Giardina, E., Stuart, P.E., Nair, R., Helms, C., et al. (2009). Deletion of the late cornified envelope LCE3B and LCE3C genes as a susceptibility factor for psoriasis. Nat. Genet. *41*, 211–215. https://doi.org/10.1038/ng.313.

133. Maher, B. (2008). Personal genomes: The case of the missing heritability. Nature *456*, 18–21. https://doi.org/10.1038/456018a.

134. Manolio, T.A., Collins, F.S., Cox, N.J., Goldstein, D.B., Hindorff, L.A., Hunter, D.J., McCarthy, M.I., Ramos, E.M., Cardon, L.R., Chakravarti, A., et al. (2009). Finding the missing heritability of complex diseases. Nature *461*, 747–753. https://doi.org/10.1038/nature08494.

135. Fang, G., Wang, W., Paunic, V., Heydari, H., Costanzo, M., Liu, X., Liu, X., VanderSluis, B., Oately, B., Steinbach, M., et al. (2019). Discovering genetic interactions bridging pathways in genome-wide association studies. Nat. Commun. *10*, 4274. https://doi.org/10.1038/s41467-019-12131-7.

136. Wang, W., Xu, Z.Z., Costanzo, M., Boone, C., Lange, C.A., and Myers, C.L. (2017). Pathway-based discovery of genetic interactions in breast cancer. PLoS Genet. *13*, e1006973. https://doi.org/10.1371/journal.pgen.1006973.

137. Ma, J., Yu, M.K., Fong, S., Ono, K., Sage, E., Demchak, B., Sharan, R., and Ideker, T. (2018). Using deep learning to model the hierarchical structure and function of a cell. Nat. Methods *15*, 290–298. https://doi.org/10.1038/nmeth.4627.

138. Gallagher, C.S., Ginsburg, G.S., and Musick, A. (2024). Biobanking with genetics shapes precision medicine and global health. Nat. Rev. Genet. *26*, 191–202. https://doi.org/10.1038/s41576-024-00794-y.

139. Lappalainen, T., Scott, A.J., Brandt, M., and Hall, I.M. (2019). Genomic Analysis in the Age of Human Genome Sequencing. Cell *177*, 70–84. https://doi.org/10.1016/j.cell.2019.02.032.

140. Targa, A., Larrimore, K.E., Wong, C.K., Chong, Y.L., Fung, R., Lee, J., Choi, H., and Rancati, G. (2021). Non-genetic and genetic rewiring underlie adaptation to hypomorphic alleles of an essential gene. EMBO J. *40*, e107839. https://doi.org/10.15252/embj.2021107839.

141. Van der Auwera, G.A., Carneiro, M.O., Hartl, C., Poplin, R., Del Angel, G., Levy-Moonshine, A., Jordan, T., Shakir, K., Roazen, D., Thibault, J., et al. (2013). From FastQ data to high confidence variant calls: the Genome Analysis Toolkit best practices pipeline. Curr. Protoc. Bioinform. *43*, 11.10.1–11.10.33. https://doi.org/10.1002/0471250953.bi1110s43.

142. Wang, K., Li, M., and Hakonarson, H. (2010). ANNOVAR: functional annotation of genetic variants from high-throughput sequencing data. Nucleic Acids Res. *38*, e164. https://doi.org/10.1093/nar/gkq603.

143. Dobin, A., and Gingeras, T.R. (2015). Mapping RNA-seq Reads with STAR. Curr. Protoc. Bioinform. *51*, 11.14.1–11.14.19. https://doi.org/10.1002/0471250953.bi1114s51.

144. Tong, A.H.Y., and Boone, C. (2006). Synthetic genetic array analysis in Saccharomyces cerevisiae. Methods Mol. Biol. *313*, 171–192. https://doi.org/10.1385/1-59259-958-3:171.

145. Rath, S., Sharma, R., Gupta, R., Ast, T., Chan, C., Durham, T.J., Goodman, R.P., Grabarek, Z., Haas, M.E., Hung, W.H.W., et al. (2021). MitoCarta3.0: an updated mitochondrial proteome now with sub-organelle localization and pathway annotations. Nucleic Acids Res. *49*, D1541–D1547. https://doi.org/10.1093/nar/gkaa1011.

146. Kanehisa, M., Furumichi, M., Tanabe, M., Sato, Y., and Morishima, K. (2017). KEGG: new perspectives on genomes, pathways, diseases and drugs. Nucleic Acids Res. *45*, D353–D361. https://doi.org/10.1093/nar/gkw1092.

147. Gillespie, M., Jassal, B., Stephan, R., Milacic, M., Rothfels, K., Senff-Ribeiro, A., Griss, J., Sevilla, C., Matthews, L., Gong, C., et al. (2022). The reactome pathway knowledgebase 2022. Nucleic Acids Res. *50*, D687–D692. https://doi.org/10.1093/nar/gkab1028.

148. Poplin, R., Ruano-Rubio, V., DePristo, M.A., Fennell, T.J., Carneiro, M.O., Van der Auwera, G.A., Kling, D.E., Gauthier, L.D., Levy-Moonshine, A., Roazen, D., et al. (2018). Scaling accurate genetic variant discovery to tens of thousands of samples. Preprint at bioRxiv. https://doi.org/10.1101/201178.

149. Hart, T., Brown, K.R., Sircoulomb, F., Rottapel, R., and Moffat, J. (2014). Measuring error rates in genomic perturbation screens: gold standards for human functional genomics. Mol. Syst. Biol. *10*, 733. https://doi.org/10.15252/msb.20145216.

150. Xiong, E.H., Zhang, X., Yan, H., Ward, H.N., Lin, Z.Y., Wong, C.J., Fu, C., Gingras, A.C., Noble, S.M., Robbins, N., et al. (2024). Functional genomic analysis of genes important for Candida albicans fitness in diverse environmental conditions. Cell Rep. *43*, 114601. https://doi.org/10.1016/j.celrep.2024.114601.

151. Eisen, M.B., Spellman, P.T., Brown, P.O., and Botstein, D. (1998). Cluster analysis and display of genome-wide expression patterns. Proc. Natl. Acad. Sci. USA *95*, 14863–14868. https://doi.org/10.1073/pnas.95.25.14863.

152. Smoot, M.E., Ono, K., Ruscheinski, J., Wang, P.L., and Ideker, T. (2011). Cytoscape 2.8: new features for data integration and network visualization. Bioinformatics *27*, 431–432. https://doi.org/10.1093/bioinformatics/btq675.

153. Masud, S.N., Chandrashekhar, M., Aregger, M., Tan, G., Zhang, X., Mero, P., Pirman, D.A., Zaslaver, O., Smolen, G.A., Lin, Z.Y., et al. (2022). Chemical genomics with pyrvinium identifies C1orf115 as a regulator of drug efflux. Nat. Chem. Biol. *18*, 1370–1379. https://doi.org/10.1038/s41589-022-01109-0.

154. Lin, K., Chang, Y.C., Billmann, M., Ward, H.N., Le, K., Hassan, A.Z., Bhojoo, U., Chan, K., Costanzo, M., Moffat, J., et al. (2024). A scalable platform for efficient CRISPR-Cas9 chemical-genetic screens of DNA damage-inducing compounds. Sci. Rep. *14*, 2508. https://doi.org/10.1038/s41598-024-51735-y.

155. Sollis, E., Mosaku, A., Abid, A., Buniello, A., Cerezo, M., Gil, L., Groza, T., Güneş, O., Hall, P., Hayhurst, J., et al. (2023). The NHGRI-EBI GWAS Catalog: knowledgebase and deposition resource. Nucleic Acids Res. *51*, D977–D985. https://doi.org/10.1093/nar/gkac1010.

156. Harrison, P.W., Amode, M.R., Austine-Orimoloye, O., Azov, A.G., Barba, M., Barnes, I., Becker, A., Bennett, R., Berry, A., Bhai, J., et al. (2024). Ensembl 2024. Nucleic Acids Res. *52*, D891–D899. https://doi.org/10.1093/nar/gkad1049.

157. Singh, P.P., and Isambert, H. (2020). OHNOLOGS v2: a comprehensive resource for the genes retained from whole genome duplication in vertebrates. Nucleic Acids Res. *48*, D724–D730. https://doi.org/10.1093/nar/gkz909.

158. Luck, K., Sheynkman, G.M., Zhang, I., and Vidal, M. (2017). Proteome-Scale Human Interactomics. Trends Biochem. Sci. *42*, 342–354. https://doi.org/10.1016/j.tibs.2017.02.006.

159. Huttlin, E.L., Bruckner, R.J., Navarrete-Perea, J., Cannon, J.R., Baltier, K., Gebreab, F., Gygi, M.P., Thornock, A., Zarraga, G., Tam, S., et al. (2021). Dual proteome-scale networks reveal cell-specific remodeling of the human interactome. Cell *184*, 3022–3040.e28. https://doi.org/10.1016/j.cell.2021.04.011.

160. Drew, K., Lee, C., Huizar, R.L., Tu, F., Borgeson, B., McWhite, C.D., Ma, Y., Wallingford, J.B., and Marcotte, E.M. (2017). Integration of over 9,000 mass spectrometry experiments builds a global map of human protein complexes. Mol. Syst. Biol. *13*, 932. https://doi.org/10.15252/msb.20167490.

161. Harris, M.A., Clark, J., Ireland, A., Lomax, J., Ashburner, M., Foulger, R., Eilbeck, K., Lewis, S., Marshall, B., Mungall, C., et al. (2004). The Gene Ontology (GO) database and informatics resource. Nucleic Acids Res. *32*, D258–D261. https://doi.org/10.1093/nar/gkh036.

162. Ghandi, M., Huang, F.W., Jané-Valbuena, J., Kryukov, G.V., Lo, C.C., McDonald, E.R., 3rd, Barretina, J., Gelfand, E.T., Bielski, C.M., Li, H., et al. (2019). Next-generation characterization of the Cancer Cell Line Encyclopedia. Nature *569*, 503–508. https://doi.org/10.1038/s41586-019-1186-3.

163. Liberzon, A., Subramanian, A., Pinchback, R., Thorvaldsdóttir, H., Tamayo, P., and Mesirov, J.P. (2011). Molecular signatures database (MSigDB) 3.0. Bioinformatics *27*, 1739–1740. https://doi.org/10.1093/bioinformatics/btr260.

164. Segrè, D., DeLuna, A., Church, G.M., and Kishony, R. (2004). Modular epistasis in yeast metabolism. Nat. Genet. *37*, 77–83. https://doi.org/10.1038/ng1489.

165. Yu, G., Wang, L.G., Han, Y., and He, Q.Y. (2012). clusterProfiler: an R package for comparing biological themes among gene clusters. Omics *16*, 284–287. https://doi.org/10.1089/omi.2011.0118.

166. Ashburner, M., Ball, C.A., Blake, J.A., Botstein, D., Butler, H., Cherry, J.M., Davis, A.P., Dolinski, K., Dwight, S.S., Eppig, J.T., et al. (2000). Gene ontology: tool for the unification of biology. The Gene Ontology Consortium. Nat. Genet. *25*, 25–29. https://doi.org/10.1038/75556.

167. Tonikian, R., Xin, X., Toret, C.P., Gfeller, D., Landgraf, C., Panni, S., Paoluzi, S., Castagnoli, L., Currell, B., Seshagiri, S., et al. (2009). Bayesian modeling of the yeast SH3 domain interactome predicts spatiotemporal dynamics of endocytosis proteins. PLoS Biol. *7*, e1000218. https://doi.org/10.1371/journal.pbio.1000218.

168. Kuzmin, E., Sharifpoor, S., Baryshnikova, A., Costanzo, M., Myers, C.L., Andrews, B.J., and Boone, C. (2014). Synthetic genetic array analysis for global mapping of genetic networks in yeast. Methods Mol. Biol. *1205*, 143–168. https://doi.org/10.1007/978-1-4939-1363-3_10.

169. Roth, A.F., Wan, J., Bailey, A.O., Sun, B., Kuchar, J.A., Green, W.N., Phinney, B.S., Yates, J.R., 3rd, and Davis, N.G. (2006). Global analysis of protein palmitoylation in yeast. Cell *125*, 1003–1013. https://doi.org/10.1016/j.cell.2006.03.042.

170. Wan, J., Roth, A.F., Bailey, A.O., and Davis, N.G. (2007). Palmitoylated proteins: purification and identification. Nat. Protoc. *2*, 1573–1584. https://doi.org/10.1038/nprot.2007.225.

171. Virtanen, P., Gommers, R., Oliphant, T.E., Haberland, M., Reddy, T., Cournapeau, D., Burovski, E., Peterson, P., Weckesser, W., Bright, J., et al. (2020). SciPy 1.0: fundamental algorithms for scientific computing in Python. Nat. Methods *17*, 261–272. https://doi.org/10.1038/s41592-019-0686-2.

172. Griss, J., Viteri, G., Sidiropoulos, K., Nguyen, V., Fabregat, A., and Hermjakob, H. (2020). ReactomeGSA - Efficient Multi-Omics Comparative Pathway Analysis. Mol. Cell. Proteomics *19*, 2115–2125. https://doi.org/10.1074/mcp.TIR120.002155.

173. Billmann, M., Ward, H.N., Aregger, M., Costanzo, M., Andrews, B.J., Boone, C., Moffat, J., and Myers, C.L. (2023). Reproducibility metrics for context-specific CRISPR screens. Cell Syst. *14*, 418–422.e2. https://doi.org/10.1016/j.cels.2023.04.003.

174. Mazouzi, A., Moser, S.C., Abascal, F., van den Broek, B., Del Castillo Velasco-Herrera, M., van der Heijden, I., Hekkelman, M., Drenth, A.P., van der Burg, E., Kroese, L.J., et al. (2023). FIRRM/C1orf112 mediates resolution of homologous recombination intermediates in response to DNA interstrand crosslinks. Sci. Adv. *9*, eadf4409. https://doi.org/10.1126/sciadv.adf4409.

175. Parsons, A.B., Brost, R.L., Ding, H., Li, Z., Zhang, C., Sheikh, B., Brown, G.W., Kane, P.M., Hughes, T.R., and Boone, C. (2004). Integration of chemical-genetic and genetic interaction data links bioactive compounds to cellular target pathways. Nat. Biotechnol. *22*, 62–69. https://doi.org/10.1038/nbt919.

176. Cheng, J., Xia, L., Hao, X., Gan, F., Bai, Y., Zhang, C., Mao, Y., Zhu, Y., Pu, Q., Park, D.W., et al. (2022). Targeting STT3A produces an anti-tumor effect in lung adenocarcinoma by blocking the MAPK and PI3K/AKT signaling pathway. Transl. Lung Cancer Res. *11*, 1089–1107. https://doi.org/10.21037/tlcr-22-396.

Please cite this article in press as: Billmann et al., Global genetic interaction network of a human cell maps conserved principles and informs functional interpretation of gene co-essentiality profiles, Cell (2026), https://doi.org/10.1016/j.cell.2026.03.044

CellPress
OPEN ACCESS

STAR★METHODS

KEY RESOURCES TABLE

REAGENT or RESOURCE	SOURCE	IDENTIFIER
Antibodies		
Phospho-S6 Ser240/244	Cell Signaling	Cat.#2215; RRID:AB_331682
S6 kinase	Cell Signaling	Cat.#2317; RRID:AB_2238583
Phospho-Akt Ser473	Cell Signaling	Cat.#4060; RRID:AB_2315049
Akt	Cell Signaling	Cat.#2920: RRDID:AB_1147620
Phospho-Akt Ser473 D7F10	Cell Signaling	Cat.#9018; RRID:AB_2629283
Phospho-p70 S6 kinase (Thr389)(108D2)	Cell Signaling	Cat.#9234; RRID:AB_2269803
p70 S6 kinase (49D7)	Cell Signaling	Cat.#2708; RRID_AB390722
Chemicals, peptides, and recombinant proteins		
NGI-1	Selleckchem	Cat.# S8750
ABD957	Remsberg et al.[107]	N/A
Rapamycin	Selleckchem	Cat.#S1039
Methoxypolyethylene glycol maleimide (mPEG)	Sigma-Aldrich	Cat.#712469
Critical commercial assays		
EditCo Gene Knockout Kits (formerly Synthego Gene Knockout Kit v2)	EditCo	https://www.synthego.com/press/gene-knockout-kit-v2/
Wizard Genomic DNA Purification Kit	Promega	Cat.#A1120
Qiagen RNeasy Kit	Qiagen	Cat.#180244
Deposited data		
Data S1_Query Gene and Screen Information	This paper; Mendeley Data	https://doi.org/10.17632/bpcpfns6vb.1
Data S2_Library Gene Information	This paper; Mendeley Data	https://doi.org/10.17632/bpcpfns6vb.1
Data S3_HAP1 Essential Gene Analysis	This paper; Mendeley Data	https://doi.org/10.17632/bpcpfns6vb.1
Data S4_HAP1 Genetic Interaction Dataset	This paper; Mendeley Data	https://doi.org/10.17632/bpcpfns6vb.1
Data S5_Replicate Screens and MCMC Consensus GI profiles	This paper; Mendeley Data	https://doi.org/10.17632/bpcpfns6vb.1
Data S6_gRNA Validation Library Interaction Dataset	This paper; Mendeley Data	https://doi.org/10.17632/bpcpfns6vb.1
Data S7_PTAR1 CRISPR_KO vs. Gene Trap GIs	This paper; Mendeley Data	https://doi.org/10.17632/bpcpfns6vb.1
Data S8_HAP1 GI Matrix Clustered	This paper; Mendeley Data	https://doi.org/10.17632/bpcpfns6vb.1
Data S9_Global Hierarchical Clusters	This paper; Mendeley Data	https://doi.org/10.17632/bpcpfns6vb.1
Data S10_HAP1 GI Profile Similarity Network	This paper; Mendeley Data	https://doi.org/10.17632/bpcpfns6vb.1
Data S11_GI Profile Similarity Network_SAFE analysis	This paper; Mendeley Data	https://doi.org/10.17632/bpcpfns6vb.1
Data S12_Poorly Characterized Gene List	This paper; Mendeley Data	https://doi.org/10.17632/bpcpfns6vb.1
Data S13_ Chemical Genetic Interaction Data	This paper; Mendeley Data	https://doi.org/10.17632/bpcpfns6vb.1
Data S14_ GI Density and Hub Gene Features	This paper; Mendeley Data	https://doi.org/10.17632/bpcpfns6vb.1
Data S15_GI Enrichment Within and Between Protein Complexes	This paper; Mendeley Data	https://doi.org/10.17632/bpcpfns6vb.1
Data S16_GI Profile Similarity-Based Functional Hierarchy	This paper; Mendeley Data	https://doi.org/10.17632/bpcpfns6vb.1
Data S17_Genetic Suppression Analysis	This paper; Mendeley Data	https://doi.org/10.17632/bpcpfns6vb.1
Data S18_GI Density Within and Between Conserved Bioprocesses	This paper; Mendeley Data	https://doi.org/10.17632/bpcpfns6vb.1
Data S19_Tumor Suppressor List	This paper; Mendeley Data	https://doi.org/10.17632/bpcpfns6vb.1
Data S20_GI Conservation	This paper; Mendeley Data	https://doi.org/10.17632/bpcpfns6vb.1
Data S21_ED vs. qGI Analysis	This paper; Mendeley Data	https://doi.org/10.17632/bpcpfns6vb.1

(*Continued on next page*)

Continued

REAGENT or RESOURCE	SOURCE	IDENTIFIER
Data S22_GI and Co-essentiality Network Comparison and Integration	This paper; Mendeley Data	https://doi.org/10.17632/bpcpfns6vb.1
Data S23_3D Genome vs. Fitness and GI degree	This paper; Mendeley Data	https://doi.org/10.17632/bpcpfns6vb.1
Data S24_SKIC2 Genetic Interactions	This paper; Mendeley Data	https://doi.org/10.17632/bpcpfns6vb.1
RNAseq analysis of 61 HAP1 query mutant cell lines	This paper	GEO: GSE296341
Experimental models: Cell lines		
HAP1 parental cells (clone C631; sex, male with lost Y chromosome)	Horizon Discovery (https://horizondiscovery.com)	RRID: CVCL_Y019
HAP1 query mutant cell lines	This paper; Mendeley Data; Data S1	RRID: CVCL_Y019 (parental line)
Experimental models: Organisms/strains		
Saccharomyces cerevisiae TSQ3052 (*MATa ecm9-5002::natMX can1Δ::STE2pr-Sp_his5; lyp1Δ; his3Δ1 leu2Δ0 ura3Δ0 LYS2*)	Costanzo et al.[5]	N/A
Saccharomyces cerevisiae Y16258 (*MAT **a**/a ECM9/ecm9Δ::natMX CAN1/can1Δ::STE2pr-Sp_his5; LYP1/lyp1Δ; HIS3/his3Δ1 LEU2/leu2Δ0 URA3/ura3Δ0*)	This paper	N/A
Saccharomyces cerevisiae Y15767 (*MATa ecm9Δ::natMX abh1Δ::URA3 can1Δ::STE2pr-Sp_his5; lyp1Δ; his3Δ1 leu2Δ0 ura3Δ0 LYS2*)	This paper	N/A
Oligonucleotides		
Illumina TruSeq adapters (i5 and i7 indices)	Illumina	Cat.#RS-122-2001
Recombinant DNA		
TKOv3 CRISPR pooled library	Addgene	Cat.#: 90294
P13744: URA3-marked, low copy, galactose-inducible yeast expression vector	This paper	N/A
P13719: URA3-marked, low copy, galactose-inducible yeast expression vector expressing human *PTAR1* and *RABGGTB*	This paper	N/A
P13708: URA3-marked, low copy, galactose-inducible yeast expression vector expressing human *ABHD16A*	This paper	N/A
P13712: URA3-marked, low copy, galactose-inducible yeast expression vector expressing human *ABHD17B*	This paper	N/A
P13713: URA3-marked, low copy, galactose-inducible yeast expression vector expressing yeast *ABH1*	This paper	N/A
Software and algorithms		
Quantitative genetic interaction (qGI) score	This paper; Billmann et al.[52]	https://github.com/csbio/qGI
Cytoscape yFiles Organic network layout	Cytoscape	https://cytoscape.org/download.html
Spatial Analysis of Functional Enrichment (SAFE)	This paper, Baryshnikova[61]	https://github.com/csbio/GIN/tree/v1.0.2
MCMC-JEDER approach for generating genetic interaction consensus profiles	This paper	https://github.com/mahfuz05062/jeder
HAP1 genome variant calling - GATK	Van der Auwera et al.[141]	https://github.com/broadinstitute/gatk
HAP1 genome variant calling - ANNOVAR	Wang et al.[142]	https://github.com/WGLab/doc-ANNOVAR
RNASeq Read Mapping	Dobin and Gingeras[143]	https://github.com/alexdobin/STAR
BIONIC	Forster et al.[114]	https://github.com/bowang-lab/BIONIC
FLEX	Rahman et al.[26]	https://github.com/csbio/FLEX_R

(*Continued on next page*)

Please cite this article in press as: Billmann et al., Global genetic interaction network of a human cell maps conserved principles and informs functional interpretation of gene co-essentiality profiles, Cell (2026), https://doi.org/10.1016/j.cell.2026.03.044

Continued

REAGENT or RESOURCE	SOURCE	IDENTIFIER
ED_analysis	This paper	https://github.com/csbio/GIN/tree/v1.0.2
Genetic suppression analysis	This paper	https://github.com/csbio/GIN/tree/v1.0.2
Profile similarity_network construction	This paper	https://github.com/csbio/GIN/tree/v1.0.2
Network integration depmap_gin analysis	This paper	https://github.com/csbio/GIN/tree/v1.0.2
Paralog analysis	This paper	https://github.com/csbio/GIN/tree/v1.0.2
Profile Similarity_hierarchical clustering	This paper	https://github.com/csbio/GIN/tree/v1.0.2
Synthetic lethal analysis	This paper	https://github.com/csbio/GIN/tree/v1.0.2
Within_between complex analysis	This paper	https://github.com/csbio/GIN/tree/v1.0.2

EXPERIMENTAL MODEL AND STUDY PARTICIPANT DETAILS

Human Cell lines

Parental human HAP1 cells were obtained from Horizon Discovery (clone C631; sex, male with lost Y chromosome; RRID: CVCL_Y019). Genetic interaction screens were performed in either wild-type HAP1 cells, or HAP1 cells with a defined query gene knockout. HAP1 query mutant cell lines carrying a stable LOF mutation in a query gene of interest were obtained from Horizon Discovery (catalog numbers included in Data S1) or generated in-house. In-house query mutant cell lines were generated by electroporation of single-guide RNAs (gRNA) targeting the gene of interest complexed with Cas9 protein (RNP complexes) into HAP1 parental cells using the Neon electroporation system (Thermo Scientific). For each query gene, a pool of three distinct gRNAs was used to maximize knockout efficiency (Synthego Gene Knockout Kit v2 guide pools or guides selected from TKOv3). RNP complex preparation and electroporation was carried out according to manufacturer's instructions. Genomic DNA extracted from knockout pools was sequenced by Sanger sequencing using primers proximal to the guide target sites and analyzed using TIDE to estimate editing efficiency. Single clones were selected by limiting dilution and mutations in clonal populations were confirmed using Sanger sequencing of the target region. For every cell line, we carry out STR profiling to ensure that the cells match references for authentication. Moreover, cells are regularly monitored for mycoplasma infection. A complete list of query mutant cell lines used in this study is provided (Data S1). Cell culture conditions are described in the method details section below. Query cell lines constructed in house or purchased from Horizon Discovery (https://horizondiscovery.com) are indicated in Data S1. HAP1 query mutant cell lines constructed "in house" are available upon request.

Saccharomyces cerevisiae strains

All strains used for Synthetic Genetic Array (SGA) analysis, yeast two hybrid analysis and complementation assays were derivatives of BY4741 or Y7092, the construction of which was described previously.[144] A temperature-sensitive allele of *ECM9*, TSQ3052 (*MATa ecm9-5002::natMX can1Δ::STE2pr-Sp_his5; lyp1Δ; his3Δ1 leu2Δ0 ura3Δ0 LYS2*) was used as a query mutant for SGA analysis. Yeast complementation analysis was performed using Y16258 (*MAT **a**/a ECM9/ecm9Δ::natMX CAN1/can1Δ::STE2pr-Sp_his5; LYP1/lyp1Δ; HIS3/his3Δ1 LEU2/leu2Δ0 URA3/ura3Δ0*) or Y15767 (*MATa ecm9Δ::natMX abh1Δ::URA3 can1Δ::STE2pr-Sp_his5; lyp1Δ; his3Δ1 leu2Δ0 ura3Δ0 LYS2*) as indicated below.

METHOD DETAILS

General information about the datasets

HAP1 essential gene and single mutant fitness datasets

We provide a list of HAP1 essential genes and a catalog of single mutant fitness measurements for all HAP1 genes targeted by the TKOv3 library[51] in both rich and minimal growth medium, as described below (HAP1 single mutant fitness effects and identification of essential genes). Essential library genes and library gene mutant fitness measurements are provided in Data S2.

HAP1 genetic interaction datasets

Genetic interaction analyses described in this study are based on either the [1] complete or [2] non-redundant HAP1 genetic interaction dataset as describe below and provided in Data S4.

[1] *Complete genetic interaction dataset (298 query mutant cell lines x 17,804 library genes).* The complete dataset comprises 298 genome-wide screens, corresponding to 222 mutant cells lines, each carrying a single loss-of-function (LOF) mutation in a unique query gene of interest. Thus, the complete dataset includes biological replicate screens for a set of 50 query mutant cell lines. The number of replicates/query mutant ranges from 2 to 8 replicates depending on the query mutant cell line. Each query mutant cell line was screened for negative and positive interactions with 17,804 genes targeted by the TKOv3 library.[51] This includes a set of 80 library genes that exhibited highly variable single mutant fitness effects across replicate wild-type

screens. A list of query mutant cell lines and genome-wide screens, including biological replicate screens performed as part of this study is provided in Data S1. A list of all library genes targeted by TKOv3, including those with variable single mutant fitness, is provided in Data S2. The complete genetic interaction dataset was used for all analyses based on genetic interaction profile similarity, unless otherwise indicated. Data S4 contains single and double mutant fitness (log_2 fold change) measurements as well as genetic interactions (qGI scores) derived from the complete dataset, which includes all gene pairs tested in this study, including biological replicates of query mutant cell lines and library genes that showed variable single mutant fitness.

[2] *Non-redundant genetic interaction dataset (222 query mutant cell lines x 17,724 library genes).* The non-redundant genetic interaction dataset consists of 222 mutant cell lines, each carrying a LOF mutation in a unique query gene. A representative screen was selected for each query gene mutant cell line that was repeated multiple times and replicate screens were excluded from this dataset. Gene pairs involving the set of 80 library genes that exhibited highly variable single mutant fitness in replicate wild-type screens were also excluded from this dataset. Thus, the non-redundant dataset comprised negative and positive genetic interactions derived from 222 unique query genes screened against 17,724 library genes. Lists of query mutant cell lines and library genes that comprise the non-redundant dataset are provided in Data S1 and S2, respectively.

The non-redundant genetic interaction dataset was further filtered based on genetic interaction score ($|qGI| > 0.3$) and statistical significance (FDR < 0.1) thresholds, which we found to strike an optimal balance between false negative and false positives. The quality estimates of data produced at different thresholds was completed as described below (see section, estimating reproducibility of genetic interactions) and is provided in Figure S5 and Data S5. In total, the non-redundant dataset contains fitness phenotypes associated with perturbation of 3,934,506 unique gene pairs and 88,933 high confidence genetic interactions (47,052 negative and 41,881 positive genetic interactions)(Data S4). This dataset was used for all analyses based on direct negative and positive genetic interactions, unless otherwise indicated.

Mitochondrial genes

Previous studies showed that gene pairs with strongly correlated co-essentiality profiles, required for fitness of the same set of DepMap cancer cell lines, predominantly involved mitochondrial-related genes, especially those encoding components of the electron transport chain (ETC) or the 55S ribosome.[26] The HAP1 genetic interaction profiles for mitochondrial gene pairs were also among the most correlated in the HAP1 genetic network (Figures 1B and S7B). ETC and 55S ribosome proteins are highly stable and detection of a growth phenotype resulting from the disruption of these genes may not manifest until the wild-type protein is depleted. Indeed, experimental factors, such as sampling time and cell line doubling rate, were shown to impact fitness measurements and amplify correlation between DepMap co-essentiality profiles associated with ETC and 55S ribosome genes.[26] Given the potential for various experimental factors to confound scoring and interpretation of mitochondrial-related genetic interactions and profiles, we explored network properties for all tested gene pairs as well as for the subset of gene pairs that excluded genetic interactions involving mitochondrial-related genes. To do so, we compiled a list of 1,102 genes targeted by gRNAs in the TKOv3 library that are also associated with mitochondrial function based on 4 sources: [1] Human MitoCarta 3.0,[145] [2] the Kyoto Encyclopedia of Genes and Genomes (KEGG; Oxidative Phosphorylation term),[146] [3] REACTOME database (Electron Transport pathway term),[147] [4] mitochondrial-related protein complexes annotated in the CORUM protein complex database[66] as well as manually curated genes. The list of genes with mitochondrial-associated function is provided in Data S2. To exclude mitochondrial signals, the indicated analyses were repeated by excluding gene pairs where both genes appeared on the mitochondrial-associated function gene list. Gene pairs that contained only one gene from the mitochondrial-associated function gene list were not excluded from analyses.

TKOv3 library, query mutant cell lines and genome-wide CRISPR screens

HAP1 genome variant calling

To fully characterize the expected editing efficacy of sgRNAs in our TKOv3 library, we generated Illumina whole genome sequencing for the HAP1 parental cell line to identify variants relative to the reference human genome. The sequencing data is summarized as follows:

Type	Platform	Depth	# of reads	mean_length	mean_insert_size
Illumina	HiSeq	145×	1453105919 pair-end reads	150bp	291bp

To call variants, we applied the GATK-recommended variant calling workflow[148] with the ploidy parameter for HaplotypeCaller set to 1. Discovered variants were then filtered for exonic variants using ANNOVAR.[142] hg19 was used as the reference genome for all steps. This process resulted in a total of 14,941 exonic variants, which were then analyzed for overlap with TKOv3 guide library target sites (Data S2). Approximately 0.07% (55 gRNAs) of all gRNAs in the TKOv3 library targeted regions where the HAP1 genome sequence varied from the reference genome (Data S2). In each of these cases, at least two other gRNAs in the TKOv3 library targeted unaffected regions in the same gene.

HAP1 query mutant cell line construction. Parental human HAP1 cells were obtained from Horizon Discovery (clone C631; sex, male with lost Y chromosome; RRID: CVCL_Y019). Screens were performed in either wild-type HAP1 cells, or HAP1 cells with a defined query gene knockout. HAP1 query mutant cell lines carrying a stable LOF mutation in a query gene of interest were obtained from Horizon Discovery (catalog numbers included in Data S1) or generated in-house. In-house query mutant cell lines were generated by electroporation of single-guide RNAs (gRNA) targeting the gene of interest complexed with Cas9 protein (RNP complexes) into HAP1 parental cells using the Neon electroporation system (Thermo Scientific). For each query gene, a pool of three distinct gRNAs was used to maximize knockout efficiency (Synthego Gene Knockout Kit v2 guide pools or guides selected from TKOv3). RNP complex preparation and electroporation was carried out according to manufacturer's instructions. Genomic DNA extracted from knockout pools was sequenced by Sanger sequencing using primers proximal to the guide target sites and analyzed using TIDE to estimate editing efficiency. Single clones were selected by limiting dilution and mutations in clonal populations were confirmed using Sanger sequencing of the target region. A complete list of query mutant cell lines used in this study is provided (Data S1). Query cell lines constructed in house or purchased from Horizon Discovery (https://horizondiscovery.com) are indicated in Data S1. HAP1 query mutant cell lines constructed "in house" are available upon request.

TKOv3 library virus production and multiplicity of infection determination. Genome-wide screens were carried out using the Toronto Knockout version 3 (TKOv3) CRISPR library (Addgene #90294), as previously described.[51] CRISPR library lentivirus production was conducted as previously described.[46] To determine viral titers, 3 million HAP1 cells seeded in 15 cm plates were transduced with different dilutions of the TKOv3 lentiviral gRNA library in medium containing 8 μg / mL of polybrene, in a total of 20 mL medium. After 24 h, the virus-containing medium was replaced with 20 mL of fresh medium containing puromycin (1 μg / mL), and cells were incubated for an additional 48 h. Multiplicity of infection (MOI) of the titrated virus was determined 72 h post-infection by comparing percentage survival of puromycin-selected cells with that of cells that were infected but not selected with puromycin (puro-minus controls) after subtracting the percentage survival of uninfected cells in puromycin-containing medium.

Pooled, genome-scale CRISPR screens. Genome-wide genetic interaction screens were performed as previously described.[45,46] Briefly, 3 million HAP1 cells per plate were seeded in 15 cm plates in 20 mL of specified medium. A total of 90 million cells were transduced with lentivirus containing the TKOv3 library at a multiplicity of infection (MOI) of ~0.3 in the presence of polybrene (8ug/mL), such that each gRNA was represented in ~200-300 cells. Transduced cells were allowed to recover for 24 h, selected using puromycin (1ug / mL) for 48 hours, and then a pellet was collected to represent the T0 starting population. The remaining cells were split into triplicate 15 cm plates (3 million cells per plate, 15 million cells total per replicate, representing ≥200-fold library coverage), and cultured for 10-12 population doublings. Three pellets (one from each technical replicate) were collected to represent the endpoint populations. Screens were performed in either DMEM with 10mM glucose and 1mM glutamine ('minimal medium'), or IMDM with 25mM glucose and 1mM pyruvate ('rich medium'), as indicated in Data S1. All media was supplemented with 10% FBS and 1% penicillin–streptomycin, and cultures were grown at 37°C with 5% CO2 and passaged every 3-4 days while maintaining a library coverage >200-fold throughout.

Preparation of sequencing libraries and Illumina sequencing. Sequencing library preparation and Illumina sequencing was performed as described previously.[45,46] Genomic DNA was extracted using the Wizard Genomic DNA Purification Kit (Promega). The gDNA pellets were resuspended in TE buffer, and the concentration was estimated by Qubit using double-stranded DNA (dsDNA) Broad Range Assay reagents (Invitrogen). Sequencing libraries were prepared from 50 μg of the extracted gDNA in two PCR steps, the first to enrich gRNA regions from the genome, and the second to amplify gRNA and attach Illumina TruSeq adapters with i5 and i7 indices, as described previously, using staggered primers aligning in both orientations to the gRNA region.[45,46] Barcoded libraries were gel purified, and final concentrations were estimated by Qubit or qRT–PCR. Sequencing libraries were sequenced on an Illumina HiSeq2500 using single-read sequencing and were completed with standard primers for dual indexing with HiSeq SBS Kit v4 reagents. The first 21 cycles of sequencing were dark cycles, or base additions without imaging. The actual 36-base read begins after the dark cycles and contains 2 index reads, in which i7 is read first, followed by the i5 sequences. The T0 and end time point samples were sequenced at 400- and 200-fold library coverage, respectively.

HAP1 single mutant fitness effects and essential genes

We estimated robust single mutant fitness effects for all human genes targeted by our TKOv3 gRNA library in HAP1 cells. We also defined a robust set of HAP1essential genes.

Library gene mutant fitness catalogue

Single mutant fitness (SMF) effects for 17,804 protein-coding genes targeted by the TKOv3 gRNA library were estimated from a collection of 39 independent wild-type control HAP1 screens. Those screens were completed in minimal (n = 21) and rich (n = 18) cell culture medium, and library gene SMF in each medium was estimated separately. First, SMF effects were estimated from each individual wild-type screen by subtracting the sequencing depth-normalized and $\log_2$-transformed read-counts representing the abundance of each gRNA in the library at the start of the experiment (T0) from those at the experimental endpoint. For each wild-type control screen, gRNA-level $\log_2$-fold changes (LFC) were then adjusted such that the median of all gRNA targeting a gold-standard, nonessential gene set[149] is equal to zero, and mean-summarized across the three technical replicates per screen. Across all wild-type control screens in each media condition, gRNA LFC were then mean-summarized for all gRNAs not flagged

Please cite this article in press as: Billmann et al., Global genetic interaction network of a human cell maps conserved principles and informs functional interpretation of gene co-essentiality profiles, Cell (2026), https://doi.org/10.1016/j.cell.2026.03.044

by our empirical quality score (see Filtering TKOv3 gRNAs). Finally, library gene SMF was derived by mean-summarizing across the 2-4 independent gRNAs targeting each library gene. Library gene SMF measure in each media condition is provided in Data S2 and shown in Figure S1.

Random forest model to identify HAP1 essential genes

In addition to library gene SMF, we also defined the subset of library genes that are essential for HAP1 growth in cell culture. The identification of the HAP1 essential gene set was formulated as a binary prediction problem. Features for the predictive model were derived from the complete collection of HAP1 wild-type control (described above) and query mutant genetic interactions screens (described below), and a gold standard set of "core" essential genes that are essential in at least 60% of human cell types examined in the 20Q2 release of Cancer Dependency Map project dataset (DepMap; depmap.org/portal).[10,12,13] A gene was labeled as core essential if the gene met a CERES score cutoff of < -1 in more than 60% of DepMap cancer cell lines. A CERES score < -1 threshold corresponds to the median score of all essential genes in the DepMap data. We note that this is a relatively stringent criterion as the goal was to identify a set of genes that is highly likely to be essential across most human cell lines as a basis for training our model. This set of high-confidence core essentials resulted in 733 essential genes amongst the 17,804 genes targeted by our library (Data S2). We reasoned that these core essential genes could be used to learn specific characteristics of essential genes in our HAP1 screen data. The assumption is that the majority of "core" essential genes are also essential in HAP1, but that training a predictive model to recognize the features of those genes based on HAP1 data would identify additional HAP1 essential genes with high accuracy. This provides a more precise definition of HAP1 essential genes by leveraging the wealth of phenotype data collected as part of this study compared to more simple strategies such as applying a single threshold on the average LFC per gene derived from wild-type control screens.

We trained a random forest supervised model to predict HAP1 essential genes. Three different types of features from our HAP1 screen data were used as input to this model, which can be grouped into three general categories: [1] *Central tendency (mean/median LFC) features*. These reflect average single mutant phenotypes across the 298 genome-wide genetic interaction screens completed as part of this study: [2] *Variance features*. These reflect variability of individual genes' phenotypes across the 298 screens. Specifically, the standard deviation and coefficient of variance of LFC values were used as inputs to our model. [3] *Screen dynamics features.* These features were derived from time-resolved wild-type control screens where we sampled gRNA abundance at different timepoints over the course of the screen, which helped to differentiate essential genes from genes that simply result in a slow growth phenotype in cell culture. Screen dynamics metrics were based on the pairwise slopes between gRNA abundance measured at different time points. The complete set of features, detailed descriptions, and the feature table used for this essential gene model are provided as Data S3.

Input features along with the gold-standard core essential gene set was used to build and optimize parameters for a random forest classifier using a 5-fold cross-validation approach. For each gene, the predicted probability of gene essentiality was extracted from the model for which it was in the held-out fold, and a precision-recall curve was used to evaluate overall performance of the model. All genes that met a score threshold corresponding to a 0.95 recall or higher on the gold-standard essential gene set were defined as "HAP1 essential". This process was conducted separately for HAP1 screens performed in minimal and rich media to predict two essential gene sets, one in each media condition. The overlapping essential genes from the rich and minimal media conditions was used to define the complete HAP1-specific essential gene set, which consists of 1,524 genes. Genes that were not deemed essential by this process but exhibited a statistically significant SMF effect (LFC < 0 or LFC > 0) were deemed "non-essential fitness effect" genes, which included an additional 2,417 genes. The complete set of HAP1 essential library genes and nonessential genes associated with a fitness effect are listed in Data S2 and shown in Figures S1 and S2.

Features associated with HAP1 essential genes

We analyzed the collection of HAP1 essential genes, described above, for differences in several physiological, evolutionary and functional gene features listed in Data S14. For continuous-valued and discrete-valued features, we used Wilcoxon rank-sum tests to assess the difference in the HAP1 essential gene set distribution from the distribution of the non-essential gene set. For features that were statistically significant, we plotted the log-ratio of the mean of the essential gene group to the non-essential gene group for that feature (absolute value was first applied to negative means, Figure S2E). The essential gene set was also tested for enrichment across the Reactome pathways and GO biological process terms Data S3). The results of these analyses are shown in Figure S2.

A quantitative genetic interaction (qGI) score

To derive quantitative genetic interactions, we modeled expected combinatorial gene perturbation effects and estimated the deviations from this null model as the quantitative genetic interaction (qGI) score. Each step is described in more detail below, but we provide a brief overview of the process here. We compare the fitness effects of each query mutation screen with a wild-type HAP1 control screen and fit a loess (locally estimated scatterplot smoothing) regression as the null model. This partially adjusts the growth effect distribution of all library genes to the background of a given query. Additional corrections to the data improve this null model. Since genetic interactions are estimated semi-independently for each query screen, those corrections are applied on a per genetic interaction screen basis followed by a network-wide set of corrections for systematic biases that cannot be estimated from individual screens. Each of these steps is described briefly below and in detail in an associated manuscript.[52] All corrections were completed at the gRNA level to increase sensitivity unless stated otherwise.

Please cite this article in press as: Billmann et al., Global genetic interaction network of a human cell maps conserved principles and informs functional interpretation of gene co-essentiality profiles, Cell (2026), https://doi.org/10.1016/j.cell.2026.03.044

Filtering TKOv3 gRNAs

Based on screens completed as part of this study, we identified a small set of guides with clear efficacy issues and removed them from further analysis. Specifically, for every gene targeted in the TKOv3 library, we compared gRNA-level genetic interaction profiles (see qGI score described below) across all screens. For each within-gene gRNA pair, we computed a pairwise Pearson correlation coefficient and median-summarized this for each single gRNA (excluding self-correlation). This score quantified how similar genetic interaction profiles of gRNAs were to those of other gRNA targeting the same gene. Based on this metric, we removed the worst gRNA for 517 of 17,804 genes (2.9%) prior to computing the gene-level genetic interaction scores (qGI scores), the associated FDR, and the single mutant fitness (SMF). More details on the gRNA quality score are provided in.[52]

Individual screen corrections

Hybrid T0 normalization. First, we measured gRNA abundance by sequencing the library for each screen after the puromycin selection (T0) and balanced this abundance with an average of the T0 gRNA abundances derived from all other screens in the dataset. This prevented gRNA loss during puromycin selection, which can lead to spurious genetic interaction calls.

MA transformation. Next, for each wild-type control-query screen pair, we MA-transformed the fitness scores prior to fitting the loess model. This stabilized null model estimates for extreme positive or negative fitness scores.

Effect size scaling. Query mutant cell lines with extreme single mutant fitness phenotypes often exhibited strong, non-specific deviations from the null model. These effects were controlled by adjusting residual values for a screen by matching the variance of the central 80% of residual effects.

Multiple WT-query pairs. The null model is fit for all pairs of a query screen with all wild-type control screens performed in the same growth medium (21 minimal media screens; 18 rich media screens) and the residual effects are shrunk by providing the highest weight to the pair with the smallest sum of squared residuals.

Local genetic interaction shift correction. Finally, residual scores for gRNAs are arranged according to the genomic positions of their target genes, and smoothing is conducted to identify genome regions where a collection of gRNAs that target adjacent genomic regions deviate from the null model either positively or negatively. The median of residual scores of detected shifts was set to 0.

Network-wide corrections

Variable single mutant fitness correction. To specifically isolate screen-to-screen variation due to the query mutation, we computed mock residual fitness scores by comparing wild-type control screens in each media condition to other wild-type control screens conducted in the same medium. Mock residual fitness scores represent ''pseudo-genetic interactions'', or genetic interactions that are identified in the absence of a query mutation and thus provide an estimate of expected single mutant fitness variability per library gene in actual query mutant cell line screens. Based on these estimates, we first corrected the per-gRNA variance across query screens to account for the observed variation across wild-type control screens. We also observed reproducible co-variance amongst gRNAs (and the corresponding genes) across multiple control screens, suggesting there are biological factors driving systematic effects in control screens (and query screens). To remove this covariation, we used Singular Value Decomposition (SVD) to isolate singular vectors describing the variation observed across control screens then projected the query screen data onto these control screen components and subtracted the resulting projections from the query residual matrix. This effectively removed signal from the query screen data that reflects patterns also observed in control screens. This analysis also identified library genes with highly variable single mutant fitness phenotypes in the control screens. A set of 80 library genes that exhibited the most variable fitness effects (''core'' set of highly variable fitness genes) were excluded from all analyses related to genetic interaction degree and density in this study (Data S2). An ''expanded'' set of library genes that exhibited more subtle variation in the control screens was also identified, which included 427 additional genes (Data S2). The complete set of 507 ''core'' and ''expanded'' library genes with variable single mutant fitness were excluded from the construction and analysis of the HAP1 genetic interaction profile similarity network (see ''constructing a genetic interaction profile similarity network'' section below) to ensure library genes susceptible to variation in controls did not affect our conclusions from these analyses. Information related to all query and library genes is provided in Data S1 and S2, respectively.

Global systematic effect correction. Minimal and rich medium SVD-corrected ''pseudo-genetic interaction'' matrices were merged into a global query gene-by-library gene residual matrix. Patterns explaining substantial variation in this matrix are not expected to reflect true genetic interactions (given that GIs are expected to be sparse), and thus, we applied a second SVD normalization to the merged matrix to removed contributions of the first four singular vectors.

gRNA quality control and gene-level genetic interaction scores. As described above (see Filtering TKOv3 gRNAs), based on an empirical gRNA quality score, we removed the lowest scoring gRNA for a total of 517 genes. Additional details on all of these scoring and normalization steps and evaluation of their specific impact on the resulting quantitative genetic interaction scores are available elsewhere.[52] These correction steps produced corrected residual (gRNA-level genetic interaction) scores derived from analysis 324 query screens that comprised 69,474 high-quality gRNAs targeting 17,804 protein-encoding genes. All genes were targeted by at least two gRNAs each, and 90.4% of genes were targeted by four independent gRNAs.

To measure quantitative GI (qGI) scores for query-library gene pairs, the mean of the 2-4 residual values for a given query-library gene combination was computed. Each qGI score was assigned a statistical significance measure using the following procedure. gRNA-level residuals for each query-library gene pair were computed (i) prior to network-wide corrections to preserve experimental uncertainty of the measurements and (ii) resolved to show all contrasts between a given query and the multiple number of wild-type control screens (minimal medium (min) screens, n = 21; rich medium (rich) screens, n = 18). By considering those 18 or 21 gRNA-level

values as technical replicates and the 2-4 independent gRNA sequences as biological replicates for the same gene pair, we computed *P*-values reflecting the deviation from 0 using a moderated t-test followed by multiple hypothesis correction using the Benjamini-Hochberg method to control FDR. As detailed below (see section estimating reproducibility of genetic interactions), we performed extensive analysis of the reproducibility of genetic interactions at a range of effect size and FDR thresholds (Data S5). Genetic interactions at a standard confidence threshold were identified using |qGI| > 0.3 and FDR < 10% thresholds, and strict genetic interactions were identified using |qGI| > 0.6 and FDR < 1% thresholds. Sensitivity and precision of the interactions identified at those thresholds are characterized in the "estimating reproducibility of genetic interactions" section below.

Estimating reproducibility of genetic interactions

We applied a Markov Chain Monte Carlo (MCMC)-based approach to estimate the reproducibility of genetic interactions, as previously described.[57] Briefly, we performed 4-5 biological replicate screens for 7 representative query mutant cell lines (*FANCG, FASN, NGLY1, PDCD5, PELO, PTAR1* and *VPS52*) (see Data S5). First, genetic interactions were scored independently for each biological replicate screen, generating qGI scores and an associated FDR for each library gene targeted in every query gene biological replicate screen. A "consensus profile" was then inferred for each query mutant starting from a thresholded version of the replicate interaction profiles, where a weak confidence threshold is applied (FDR < 50%) to define a set of positive or negative interactions for that screen. An MCMC approach is then used to jointly infer false negative rates (FNR) and false positive rates (FPR), as well as a binary consensus GI profile (separately for positive/negative GI). After this inference process converges, the resulting consensus profile is used to generate a data-derived interaction standard for evaluation of individual screen data (assuming pairs with posterior probability of interaction of > 0.5 are interactions). Finally, this consensus standard is used to evaluate per screen performance characteristics over a range of different qGI score effect size and statistical significance cutoffs (FDRs) on the per screen scores. At each evaluated qGI score effect size and statistical significance cutoff, we measured precision and recall metrics, which were then summarized across this collection of 7 replicated query screens. This evaluation led to the selection of two recommended cutoffs for our dataset. A "strict" cutoff (|qGI score| > 0.6 and FDR < 1%), which results in an estimated precision of per screen called genetic interactions of 0.91 and a recall of 0.12 and a "standard" cutoff (|qGI score| > 0.3 and FDR < 10%), which results in an estimated precision of per-screen called interactions of 0.61 and a recall of 0.37. For all analysis that depended on a thresholded set of genetic interactions, we applied the "standard" cutoff, unless otherwise noted. Data S4 provides unfiltered qGI scores and FDR statistics for all tested gene pairs. Precision and recall estimates are provided over a range of different qGI score and FDR thresholds highlighting the relative balance between false positives and false negatives such that a user can define thresholds appropriate for future studies. The results of this analysis are presented in Figure S5A and Data S5.

Validating genetic interactions with an independent gRNA library

We constructed an independent gRNA library consisting of ~37,000 gRNAs targeting ~1,200 genes that showed significant negative or positive genetic interactions in at least one of five genetic interaction screens using *ARID1A*, *FANCG*, *FASN*, *NGLY1* or *PTAR1* query mutant cell lines (Figure S5H; Data S6). Candidate gRNA sequences were identified from FASTA files of the hg38 chromosomes using the regular expression pattern '[ACGT]{20}.GG', then filtered to remove guides with polyT stretches and Esp3I restriction sites. Next, genomic coordinates for the filtered guide sequences were overlapped with exons from the desired target ~1,200 genes using bedTools 'intersectBed' to produce a list of candidate sgRNAs. Finally, to produce a library that widely covered the target genes, up to 40 sgRNAs per gene were selected randomly from the filtered candidate gRNAs. Of the genes targeted, 743 were targeted by 40 sgRNAs, while the remainder of genes were targeted by fewer. The vast majority (> 95%) of gRNAs in this library were not represented in the TKOv3 library. To calculate differential LFC scores, we performed the following steps: [1] Remove gRNAs with either NA or read count < 30 in any of the WT or query T0 screens; [2] Depth normalize read count data as follows: normalized reads per screen = [(raw reads/sum of reads) * 1,000,000] + 1; [3] Calculate LFC between each replicate and the reference timepoint; [4] Average across all gRNAs and technical replicates per library gene to obtain the final differential LFC for each query; [5] Calculate the differential LFC for each gene based on its LFC values measured in the query gene mutant cell line and the reference WT control cell line; [6] For each query gene, separate the 1,215 library genes into groups of "negative", "positive", and "no interaction" based on the qGI score and FDR associated with the corresponding gene pair derived from genome-wide TKOv3 screens. Raw read counts and differential LFC scores used to independently identify genetic interactions for 5 different query genes of the gRNA tiling library, are provided in Data S6 and results from this analysis are shown in Figure S5H.

Hierarchical clustering of HAP1 genetic interaction profiles

We modified a previously described hierarchical clustering algorithm to cluster the complete HAP1 genetic interaction dataset and produce a set of uniformly sized gene clusters across layers of the dendrogram (Zenodo: https://doi.org/10.5281/zenodo.15320010).[150] Briefly, for each dendrogram layer, an iterative process identified gene clusters based on their size and a signal-to-noise ratio (SNR), calculated as the average within-cluster Pearson correlation divided by its standard deviation.[150] Gene clusters that met a minimum size requirement (at least three genes) and ranked in the top percentile of SNR were selected and removed from subsequent clustering iterations. Genes that did not belong to a cluster in the first iteration were re-clustered in subsequent iterations until only one or no genes remained or until remaining clusters did not meet the selection criteria. This process was then repeated at the next layer of the dendrogram. This iterative approach within each layer ensured balanced clustering by

Please cite this article in press as: Billmann et al., Global genetic interaction network of a human cell maps conserved principles and informs functional interpretation of gene co-essentiality profiles, Cell (2026), https://doi.org/10.1016/j.cell.2026.03.044

preventing a few highly coherent clusters from dominating the hierarchy. We applied this clustering algorithm to the complete genetic interaction dataset (298 query cell lines x 17,804 library genes) to generate two layers of "Global" gene clusters (L2 parent clusters and L1 child clusters), which are provided in Data S9. Results of this analysis are also shown in Figures S3D and S9A.

We also applied the algorithm to cluster a smaller subset of 3,784 genes that comprise the high-confidence profile similarity network and used this subset of clusters to define the HAP1 functional hierarchy, as described below (see section: a genetic interaction profile similarity-derived functional hierarchy, Data S16).

Constructing a genetic interaction profile similarity network

To construct the genetic interaction profile similarity network shown in Figure 1, we performed two additional filtering/normalization steps before constructing the profile similarity network. The purpose of both additional steps was to ensure that the similarity network analysis was focused on the highest confidence set of genes and that any non-specific interaction signal was removed before computing similarity networks. First, excluded an expanded set of 507 library genes associated with variable single mutant fitness phenotypes from the complete HAP1 genetic interaction dataset. The list of library genes with variable mutant fitness is provided in Data S2. Second, additional normalization procedures were applied to genetic interaction profiles to construct the profile similarity network. These normalization procedures are described in detail below.

Genetic interaction profile normalization

We identified two gene expression patterns related to several query mutant cell lines that were distinct from the HAP1 parental cell line gene expression profile based on genome-wide gene expression profiling of 60 selected HAP1 query mutant query cell lines, described below (see section expression profiling of HAP1 query mutant cell lines). In both cases, the group of cell lines that exhibited a similar differential expression signature also exhibited similar patterns of genetic interactions (Figure S7C). For most cell lines, the observed differential expression patterns had no clear connection to the query mutation. Thus, we concluded that the observed expression signatures and genetic interaction profiles shared by query mutant cell lines comprising each group may reflect experimental and/or biological factors that were not entirely related to the specific query gene mutation. As a result, we applied additional normalization procedures to the genetic interaction dataset to minimize "non-specific" similarities between genetic interaction profiles prior to constructing the HAP1 genetic interaction profile similarity network.

First, we applied standard two-dimensional clustering analysis[151] to the gene expression and the HAP1 genetic interaction data corresponding to the subset of 60 query mutant cell lines to identify two distinct groups of query genes that shared similar gene expression signatures and genetic interaction profiles (Figure S7C). The first group consisted of 5 query mutant screens that shared a similar gene expression and genetic interaction profiles (GSK3A_GIN247, GSK3B_GIN237, FANCA_GIN010, BCL2_GIN338, EMC6_GIN231)(Data S1). The second group involved 5 query gene screens (CRIPT_GIN260, MPV17_GIN230, C5orf34_GIN261, TMEM126A_GIN309 and POLR2A_GIN281)(Data S1) that also shared similar gene expression and genetic interaction profiles but whose profiles were distinct from the profiles associated query genes in the first group. For each group, we defined an "expression centroid" and a "qGI centroid" signature representing the average differential expression pattern and average genetic interaction pattern (based on qGI scores) for each group of query genes, respectively. We next examined the complete set of 298 genome-wide screens to identify additional query genes with genetic interaction profiles that resembled the genetic interaction profiles of query genes belonging to Centroid 1 or Centroid 2. An additional 4 query gene screens (GSK3A_GIN405, PC_GIN219, SLX1_GIN239, KAT7_GIN173) exhibited Centroid 1-related genetic interaction profiles and another 3 screens (POLR2A_GIN395, C5orf34_GIN357, TMEM126A_402) were associated with Centroid-2 related genetic interaction profiles (Data S1). We then computed final qGI centroid vectors based these expanded query gene screen groups by computing the average qGI signature across the screens in each group, resulting in a 1 x 17,804 qGI vector for each centroid group. The complete genetic interaction dataset was first normalized for the Centroid 1 vector and then subsequently normalized for the Centroid 2 vector, using the following procedure:

[1] Each centroid was unit normalized by dividing by its l^2 norm:

$$U_{r\times 1} = C_{r\times 1} / \| C \|_2$$

[2] Each centroid unit vector was projected onto the complete qGI score matrix of 298 query screens:

$$M_{r\times c}^{projection} = U_{r\times 1} \times U_{r\times 1}^{T} \times M_{r\times c}$$

[3] The resulting centroid projection was subtracted as follows, creating a corrected matrix of qGI scores:

$$M_{r\times c}^{corrected} = M_{r\times c} - M_{r\times c}^{projection}$$

The resultant centroid-corrected genetic interaction dataset excluding 507 library genes with variable single mutant fitness (listed in Data S2) is provided as a clustered matrix in Data S8 and shown in Figure S8. The same dataset was used to construct the profile similarity network shown in Figure 1 and described below.

Expression profiling of HAP1 query mutant cell lines

Gene expression analysis was performed on 61 HAP1 cell lines (wild-type, and knockout queries) using RNA sequencing (RNAseq). Query cells were grown in the same conditions used for the screens, and pellets containing $2x10^7$ cells were collected when the cells reached 70-80% confluence. Total RNA was extracted from the pellets using Qiagen RNeasy kits. Poly(A)-enriched mRNA libraries were prepared using NEBNext Ultra II Directional RNA library prep kit using the manufacturer's protocol. Library quality was assessed on an Agilent 2100 Bioanalyzer, and all samples had an RNA integrity value (RIN) of 9.8 or higher. Samples were sequenced on an Illumina NovaSeq 6000 with an S1 flowcell with paired end 151bp reads to an approximate depth of 25 million reads per sample. After checking the sequencing quality with FastQC (v.0.11.9), reads were aligned to human genome build hg38 with Gencode v32 gene annotations using the STAR short-read aligner (v.2.7.9a) using the following parameters: –outSAMtype BAM SortedByCoordinate –quantMode GeneCounts –sjdbGTFfile gencode.v25.annotation.gtf. Per-sample read count matrices were merged with ENSEMBL and Entrez Gene annotations in R. With the bulk RNA sequencing data covering 60 query screens across 16,546 TKOv3 library genes, we calculated their $\log_2$-fold-change (LFC) values against the single mutant (WT) expression data as differential expression (DE). Raw FASTQ files and read counts are available through the GEO database with accession GSE296341.

Mapping the genetic interaction profile similarity network

We constructed a genetic interaction profile similarity network measuring similarity between library genes targeted in our genome-wide screens. First, Pearson correlation coefficients (PCC) were measured between all pairs of library genes using each gene's profile across 298 queries in the Centroid-normalized qGI score matrix described above (Data S8). We then removed edges between gene pairs whose profile similarity did not satisfy a PCC > 0.41 threshold. Finally, we removed weak similarity edges for the most highly connected genes thus setting a maximum of 30 edges/connection per gene/node in the profile similarity network. This resulted in a "core" genetic interaction profile similarity network consisting of 1017 genes and 3483 edges. The core network was visualized using the "yFiles Organic" network layout in Cytoscape (Data S10).[152] A subset of 234 genes was disconnected from the core network, and these genes were manually placed on the periphery of core network closest to the region of the network enriched for functions related to the specific disconnected gene set.

Gene coordinates in the core network were then fixed, and the network was expanded to include additional genes using a K-nearest neighbors (KNN) approach. For each gene in the core network, we ranked all other genes based on their genetic interaction profile similarity (PCC) derived from the complete, centroid-corrected genetic interaction profile similarity matrix and then selected the top K neighbor genes, where K was set to 35, and all connected genes satisfied a minimum correlation threshold (PCC > 0.1). Each node in the core network could add a maximum of K new auxiliary nodes meeting this threshold. To prevent network oversaturation caused by highly connected nodes, only one edge connecting a new gene with the highest profile similarity to another gene in the core network was added to the expanded profile similarity network. This resulted in an expanded genetic interaction profile similarity network consists of 3,784 genes and 6,433 unique edges (Figure 1; Data S10). The core and expanded profile similarity networks are also provided as Data S8 and S10. The source code and files for this network construction process are also available from (Zenodo: https://doi.org/10.5281/zenodo.15320010).

Biological process annotation of the genetic interaction profile similarity network

The expanded genetic profile similarity network was annotated using a modified version of Spatial Analysis of Functional Enrichment (SAFE).[61] The modified SAFE code is available from (Zenodo: https://doi.org/10.5281/zenodo.15320010). To functionally annotate the genetic interaction profile similarity network shown in Figure 1B, we applied the modified SAFE method using default parameters with the following exceptions:

node_distance_metric='shortpath_weighted_layout'
neighborhood_radius=0.12
attribute_distance_threshold=0.65
enrichment_threshold=0.2
multiple_testing=TRUE

To calculate node distance and define spatial network neighborhoods, we weighted profile similarity edges based on the ratio between the Euclidean distance (d_{ij}) measured between two genes/nodes in the network and the profile similarity (Pearson Correlation Coefficient, PCC) between the corresponding connected genes (i.e. edge weight = d_{ij} / PCC). SAFE was combined with a reduced set of Gene Ontology (GO) Biological Process (BP) terms filtered for size (GO BP terms containing between 1-500 genes) to identify functionally enriched regions of the genetic interaction profile similarity network. SAFE analysis identified 42 functionally enriched network domains, which were reviewed and manually merged into 17 larger functional domains (Figure 1B; Data S11).

Subcellular compartment annotation of the genetic interaction profile similarity network

To functionally annotate the genetic interaction profile similarity network shown in Figure 1C, we applied the modified SAFE method using default parameters with the following exceptions:

node_distance_metric='shortpath_weighted_layout'
neighborhood_radius=0.15
enrichment_threshold=0.001

Please cite this article in press as: Billmann et al., Global genetic interaction network of a human cell maps conserved principles and informs functional interpretation of gene co-essentiality profiles, Cell (2026), https://doi.org/10.1016/j.cell.2026.03.044

multiple_testing=TRUE

We used SAFE to identify regions of the profile similarity network enriched for genes that localize to the same subcellular compartment as defined by curated cell compartment annotations[62]

Protein complex annotation of the genetic interaction profile similarity network

We projected centroids of manually curated CORUM complexes[66] based on the spatial positions of their member genes. Complexes were retained if at least two of their genes were present in the network, and each gene was assigned to only one complex, favoring the largest in cases of overlap. These criteria yielded a nonredundant set of 71 complexes. Centroids were computed from the Euclidean coordinates of genes in the embedded network layout, with minor jitter added to prevent visual overlap. Complexes were visualized and colored according to biological process as shown in Figure 1D. A list of complexes visualized on the profile similarity network is provided (Data S11).

Using the HAP1 interaction profile similarity network to annotate function

To demonstrate the utility of the HAP1 genetic interaction profile similarity to functionally annotate genes and datasets, we applied SAFE or standard enrichment analysis to identify regions of the genetic interaction profile similarity network that were specifically enriched for genes sets derived from the datasets described below.

Annotating individual query gene genetic interaction profiles

For a given query gene, we applied the standard genetic interaction confidence threshold ($|qGI| > 0.3$, FDR < 0.1) to generate a binarized profile of negative and positive genetic interactions for a given query gene. We then used the modified version of SAFE (Zenodo: https://doi.org/10.5281/zenodo.15320010), described above, to identify regions of the HAP1 genetic interaction profile similarity network that were enriched for genes that showed negative or positive interactions with the query gene of interest. The modified SAFE method was applied using default settings with the following exceptions:

node_distance_metric='shortpath_weighted_layout'
neighborhood_radius=0.05
enrichment_threshold=0.001
multiple_testing=TRUE

This method was applied to identify regions of the genetic interaction profile similarity network that were enriched for negative and positive interactions identified with HAP1 query mutant cell lines carrying LOF mutations in either *C1orf112* as shown in Figure S9B or *VPS52* as shown in Figure 3E.

Annotating chemical-genetic interaction profiles

A chemical-genetic interaction refers to a mutant strain that exhibits sensitivity or resistance to a particular bioactive compound and the set of mutants that show differential compound sensitivity generates a chemical-genetic interaction profile reflecting the compound mode-of-action.[67] We performed genome-wide chemical-genetic interaction screens to identify genes that showed differential sensitivity to different bioactive compounds (Data S13). Chemical-genetic interaction screens were performed as previously described.[153] Briefly, HAP1 cells were grown in suspension format in 100-150mL IMDM medium supplemented with 1:700 dilution of anticlumping reagent (ThermoFisher, Cat# 0010057DG) in Erlenmeyer flasks and maintained in a shaking incubator (150 rpm, 37°C, 5% CO_2). At each timepoint, cells were collected by centrifugation and trypsinized with TrypLE.

One hundred million wild-type HAP1 cells stably expressing Cas9, were transduced with the lentiviral TKOv3 library at a low MOI (~0.3), such that each guide is represented in 200-300 cells. 24 hours post infection; cells were selected for viral integration with 1μg/mL puromycin for 48 hours. Cells were then harvested and pooled and 30-50 million cells were collected for subsequent gDNA extraction and calculation of library representation at the initial timepoint, T0. At this stage, the pooled cells were divided into three technical replicates, each consisting of 15 million cells to maintain 200-fold library coverage. Selection screens were performed by subculturing cells after four days (T4), at which point each technical replicate was divided into treatment arms, including an untreated one (DMSO, vehicle control), and sub-cultured every three to four days for up to 15 days (~15 doublings). Compounds were added at predetermined concentrations with ABD957 used at 10uM, resulting in LD30 and NGI-1 was used at 9.5-15uM with an average LD65.

Genomic DNA from pelleted cells at the initial timepoint, T0 and the endpoint, T14 were isolated using the QIAamp Blood Maxi Kit (Qiagen) and DNA concentrations were determined using the Qubit dsDNA Broad Range Assay kit (Invitrogen). To prepare sequencing libraries, 50μg of genomic DNA was processed using a two-step nested PCR approach, to amplify the sgRNA and append Illumina TruSeq adapters with i5 and i7 indices. The barcoded libraries were then purified with the QIAquick PCR Purification and Gel Extraction kits (both from Qiagen). The resulting samples were then sequenced on an Illumina HiSeq2500, using single-read sequencing. Quantitative chemical-genetic interactions were measured used a modified version of the qGI scoring method described above and elsewhere.[154] Chemical genetic interactions for NGI-1 and ABD957 are provided in Data S13 and shown in Figure S9C for NGI-1 and in Figure 5H for ABD957.

We applied a standard genetic interaction confidence threshold ($|qGI| > 0.3$, FDR < 0.1) to generate a binarized profile of negative and positive chemical-genetic interactions associated with the bioactive compound, NGI-1. We then used the modified version of SAFE (Zenodo: https://doi.org/10.5281/zenodo.15320010), described above, to identify regions of the HAP1 genetic interaction profile similarity network that were enriched for genes that showed negative or positive chemical-genetic interactions with the NGI-1, as shown in Figure S9C. The modified SAFE method was applied using the parameters described above (see section annotating individual query gene genetic interaction profiles).

Annotating OMIM disease genes

The OMIM disease set was downloaded from OMIM: https://omim.org/ in July 2021[117] and filtered to comprise a set of 208 diseases with at least 4 annotated genes. A hypergeometric test was conducted to assess which of the 17 biological process-enriched domains on the genetic interaction profile similarity network (Figure 1B) were enriched for a particular disease gene set, assuming the background gene set of all genes present on the profile similarity network. Results pertaining to this analysis are shown in Figure S9D.

Annotating GWAS phenotype-associated genes

The genome-wide association study (GWAS) trait set was downloaded from the NHGRI-EBI GWAS Catalog: https://www.ebi.ac.uk/gwas/[155] in July 2021. This data was filtered to include a subset of 194 traits with at least 60 associated variants and linked genes that passed a GWAS significance threshold of $P < 5x10^{-7}$. A hypergeometric test was conducted to assess which (if any) of the 17 biological process-enriched domains on the genetic interaction profile similarity network (Figure 1B) were enriched for genes associated with a particular trait, assuming the background gene set of all genes present on the profile similarity network. Results pertaining to this analysis are shown in Figure S9D.

Genetic interaction degree and network density analysis

Genetic interaction network hub genes

We defined library genes with a positive genetic interaction degree equal to or higher than the 95th percentile as "positive genetic interaction hub" genes. Similarly, genes were defined as "negative genetic interaction hub" genes if their negative GI degree was equal to or greater than the 95th percentile. Positive and negative GI degrees associated with all library genes are provided in Data S14. Reactome pathway enrichment analysis was performed on the hub gene sets against the universe of all library genes, restricting the set of pathways tested to those with more than 10 total genes amongst the library gene universe and less than 300 member genes. The *P*-values were adjusted with the Benjamini-Hochberg correction and were filtered using an FDR < 0.2 threshold. The enrichment results are provided in Data S14. Analysis of genetic interaction network hub genes are shown in Figures 2 and S10.

Correlation analysis of genetic interaction degree

We assessed the correlation of the number of negative and positive genetic interactions associated with each library gene derived from the nonredundant dataset with several different physiological, evolutionary and functional gene features. Gene features are described in Data S14 and include binary-, continuous-, and discrete-valued features. We used Wilcoxon rank-sum tests to determine if binary gene features partitioned genes into two groups such that one group had an average degree that was significantly higher or lower than the other group. Genes for which the value of the binary feature was unknown were excluded from the feature's test. For continuous- and discrete-valued gene features, we calculated the Pearson correlation coefficient (PCC) between genetic interaction degrees of genes and each feature. We considered the degree of genes targeted by the TKOv3 library, by counting the number of interacting query genes, meeting the standard confidence threshold ($|qGI| > 0.3$, FDR < 0.1) derived from the nonredundant dataset. The correlations for library genes are provided in Data S14 and shown in Figures 2, S10, and S11.

Analysis of high- vs. low-genetic interaction degree essential genes

To understand properties associated with essential genes that exhibited high vs. low genetic interaction degree in our screens, we tested for differences between these two groups in terms of the same physiological, evolutionary and functional gene properties described above (see Section features associated with HAP1 essential genes)(Data S14). First, we formed a group of "high-density" essential genes (among the set of all library genes) by identifying the top 20% of HAP1 essential genes in terms of total genetic interaction degree. We formed a group of "low-density" essential genes by identifying the bottom 50% of HAP1 essential genes in terms of total genetic interaction degree. The continuous-valued and discrete-valued features listed in Data S14 were then used to test for differences between these two groups with a Wilcoxon rank-sum test. For each feature, the mean of the high-density group and the low-density group was computed, and the $\log_2$ ratio of these means was plotted in Figure S10F, with and without the mitochondrial gene set (see Data S2).

Analysis of single mutant fitness and genetic interaction degree with the 3D genome

We explored essential and non-essential genes causing a negative impact on fitness in the context of genome topology by comparing both gene sets to genes found among 2,584 common significant trans-contacts ($q < 0.05$, $\geq$ 10 Hi-C datasets), that were identified by *Signature* in 62 human Hi-C datasets.[70] We converted all genes to Ensembl Gene IDs using GENCODE before comparisons. Binomial testing was used to assess the overlap and test for significance in comparison to the rest of genome. The first column of Data S23 represents a 1 Mb bin of the trans-contacts, and the second and third columns show the number of nonessential genes with fitness defects or essential genes identified in the given bin and their gene ID, respectively.

The topological map was generated from 62 near-diploid Hi-C datasets, methodological details can be found in.[70] Using the same topological map as base, we visualized genetic interactions that overlap with any of the 40,282 significant trans-contacts ($q < 0.05$, across 62 Hi-C datasets) in grey edges. We next compared genetic interactions to 2,584 common significant trans-contacts, and coloured overlapping trans-contacts based on the *qGI_score* (calculated as the conservative effect (closer to zero) for the reciprocal interactions). Data S23 includes the genetic interactions that were also identified as significant trans-contacts by *Signature*. The first two columns represent the bin IDs in the format [chromosome ID]_[start of the bin in Mb]. The third column shows the *qGI_score*. The

last column indicates whether the GI contact is found in the common significant trans-contacts. To assess the overlap of positive and negative genetic interactions with 53 anchor loci[70] in comparison with the rest of the genome, we used Mann-Whitney testing. The results of this analysis are shown in Figure S12A.

Genetic interactions involving paralogs

Genetic interactions within pairs of paralog genes

A list of paralog gene pairs was obtained from the Ensembl database.[156] In addition, a list of paralog genes classified as "Ohnolog" duplicated gene pairs was also obtained.[157] To evaluate the density of positive and negative genetic interactions observed between paralogs as a function of sequence identity, three subsets of Ensembl paralog pairs were selected based on the HAP1 expression level of each gene in a pair (Data S2): [1] Paralog pairs in which both genes had expression scores of $\log_2$ (TPM+1) > 1, [2] Paralog pairs where exactly one gene met this expression criteria, and [3] Paralog pairs where neither gene met the expression criteria. Paralogs were further binned based on their sequence identity to each other; for each sequence ID bin, the sets were filtered to include only pairs having a sequence identity greater than the bin and those pairs screened in our study for a genetic interaction. Finally, the percentage of positive and negative genetic interactions identified at a standard threshold (|qGI| > 0.3 and FDR < 10%) within the filtered set were calculated per bin for all three described subsets. To calculate the density of negative genetic interactions as a function of paralog family size, a subset of paralog pairs was selected for analysis by requiring expression in HAP1 [($\log_2$ (TPM+1) > 1] for both paralogs and requiring that the paralogs' sequence identity was greater than the indicated cut-off (20%, 50% or Ohnolog set). The family size of each paralog pair was then recalculated with respect to only paralogs that satisfied the expression and sequence identity criteria. Finally, the density of negative genetic interactions (determined by standard cut-off of qGI < -0.3 and FDR < 10%) within the filtered set was calculated among the set of pairs screened in our study and reported for each family size bin. The results of this analysis are shown in Figures 2G, S12D, and S12E.

Overall genetic interaction density of paralog genes

To calculate the overall density of negative and positive genetic interaction for paralog library genes with all query genes as a function of paralog family size, a subset of paralog pairs was selected for analysis by requiring expression in HAP1 [$\log_2$ (TPM +1) > 1] for both paralogs and requiring that the paralogs' sequence identity was greater than the indicated cut-off (20%, 50% or Ohnolog set). The family size of each paralog pair was then recalculated with respect to only paralogs that satisfied the expression and sequence identity criteria. Finally, the density of library paralog gene negative and positive genetic interactions (|qGI| > 0.3 and FDR < 0.1) with all possible query genes tested within the filtered set was calculated and reported for each family size bin. We also measured the negative and positive interaction density associated with duplicated query genes. Negative and positive interaction density was measured for query genes paralogs that shared greater than 20% sequence identity as well as Ohnolog genes that were screened as a query in this study. Query gene genetic interaction density reflects the number of negative or positive genetic interactions identified at a standard confidence threshold (|qGI| > 0.3, FDR < 0.1) per query gene divided by the total number of tested gene pairs involving the corresponding query gene. Paralog query gene interaction density was compared to negative and positive interaction density associated with non-duplicated query genes screened in this study. Results corresponding to this analysis are shown in Figures S12B and S12C.

Paralog degree asymmetry analysis

We compared the negative genetic interaction degree associated with each gene of a paralog pair (i.e. the number of negative genetic interactions each paralog exhibited with all tested query genes). Gene pairs from the Ensembl paralog pair set were selected for this analysis where both genes were represented as library gene in the non-redundant genetic interaction dataset (Data S4), both satisfied a HAP1 expression cutoff of $\log_2$ (TPM+1) > 1, and they represented paralog pair with sequence identity greater than 20% or 50%. Only paralog pairs with a negative degree (standard cut-offs of |qGI| > 0.3 and FDR < 10%) of greater than 4 were considered in this analysis. For each pair of library gene paralogs, we measured a negative interaction degree ratio statistic, computed by dividing the negative interaction degree associated with the paralog showing the higher interaction degree by the interaction degree of the sister paralog with fewer negative interactions. Ratios that were greater than 30 were assigned a value of 30. We used simulations to establish a null distribution for this ratio statistic that assumed genetic interactions would accumulate with equal probability for each gene within a paralog pair (i.e. symmetric negative interaction degree). Statistics for random paralog pairs under this null model were created by randomly generating negative interaction degrees for each gene pair from a binomial distribution with probability of 0.5 and the maximum limit of total observed degree for each real paralog pair. One thousand different random scenarios were generated, with ratio statistics measured for all random paralog pairs in each scenario. An empirical *P*-value was generated using the R 'qvalue' package (empPvals function) by comparing the observed average degree ratio and the average degree ratios from 1000 random models. The same analysis was repeated using the Ohnolog paralog list. Results from this analysis are shown in Figure S12F.

Overlap of genetic interactions with other genomic datasets

We characterized the functional relationships between pairs of genes connected by negative or positive genetic interactions by evaluating their overlap with other types of molecular and functional interactions, described below. The results of this analysis are shown in Figure S13A.

Please cite this article in press as: Billmann et al., Global genetic interaction network of a human cell maps conserved principles and informs functional interpretation of gene co-essentiality profiles, Cell (2026), https://doi.org/10.1016/j.cell.2026.03.044

Protein-protein interactions

Protein-Protein interactions (PPI) were collected from three sources and combined to generate a unified PPI standard that was compared to the HAP1 genetic interaction dataset. These included HuRI,[158] BioPlex,[159] and huMAP.[160] All possible pairs of proteins within this set that did not demonstrate a PPI in any of the datasets were assumed to be non-interacting for the purposes of this analysis.

Gene Ontology (GO) biological process co-annotated gene pairs

GO term annotations were downloaded in June of 2021[161] and a functional standard for co-annotation to GO Biological Process (GO BP) terms was built using the FLEX software.[26] Briefly, a set of GO BP terms was curated to include only those terms that contained between 2 and 300 genes. Terms of this size were considered to have enough specificity to be functionally informative. Two genes were considered functionally related if they were co-annotated to one or more of these GO BP terms. Two genes were considered unrelated if both genes were annotated to at least one GO term but the lowest common ancestor to which both genes were annotated was not part of the functionally specific set of GO bioprocess terms defined above. All other gene pairs (e.g., those with one or both unannotated genes), were ignored for the purposes of co-annotation analysis.

Co-expressed gene pairs

We measured gene co-expression using the Cancer Cell Line Encyclopedia (CCLE) dataset.[162] To generate a set of co-expressed gene pairs, expression profile similarities were calculated using Pearson correlation (PCC) for all possible gene pairs. The top 0.1% of all the gene pairs (according to PCC values) was considered as co-expressed and the rest were not considered to be co-expressed.

Co-localized protein pairs

Gene product pairs were considered co-localized if they shared one or more cellular compartment annotation(s) based on a standard we derived from the COMPARTMENTS Subcellular localization database retrieved in July 2021.[62] Specifically, we applied a high-confidence cutoff of > 4.5/5 and focused on the following subset of 9 terms: Nucleus, Nucleolus, Golgi apparatus, Mitochondrion, Peroxisome, Endoplasmic reticulum, Lysosome, Endosome, Cytoskeleton & Plasma membrane.

Co-complex annotated protein pairs

Co-complex pairs were derived from the CORUM protein complex standard (release 3.0).[66] Any pair of genes whose products were members of the same complex was treated as a positive example while any gene pair for which each of the gene products were annotated to at least one complex, but not the same complex, was treated as a negative example.

Co-pathway annotated gene pairs

Co-pathway pairs were derived from the Molecular Signatures Database (MSigDB).[163] Any pair of genes whose products were members of the same MSigDB pathway was treated as a positive example while any gene pair for which each of the gene products were annotated to at least one pathway, but not the same pathway, was treated as a negative example.

Precision-recall analysis

All precision-recall analyses were performed using the FLEX R package[26] along with the corresponding GO BP co-annotation (GO BP) or CORUM co-complex functional standards, described above. Results of precision-recall analyses are shown in Figures 7F, S7B, S14A, and S21F.

Genetic interactions within and between protein complexes

Genetic interaction enrichment within and between protein complexes

We performed tests for enrichment of genetic interactions that occur within and between protein complexes annotated to the CORUM protein complex database.[66]

Within-complex enrichment analysis tests if gene pairs connecting genes that encode members of the same protein complex are enriched for negative and/or positive genetic interactions.

Between-complex enrichment analysis tests if gene pairs encoding members of two different complexes (i.e. interaction between a gene annotated to complex 1 and a second gene annotated to complex 2) are enriched for negative and or positive genetic interactions.

For these analyses, we considered only those CORUM protein complex where at least three genes were represented in our library gene set and at least one gene was represented in the query gene set. A standard threshold ($|qGI| > 0.3$ and FDR < 0.1) was applied to identify significant negative and positive genetic interactions. When computing enrichment statistics, the library gene universe was reduced to only those genes that overlap with the CORUM complex standard genes, and all query genes in the non-redundant genetic interaction dataset (Data S1 and S4) were included in the analysis. Enrichments were calculated independently for positive, negative and total interactions (combined positive and negative) genetic interactions. *P*-values were derived from one-tailed hypergeometric tests, focusing on increased genetic interaction density relative to the background genetic interaction density. *P*-values were corrected using the Benjamini-Hochberg method applied to the within-complex and between-complex sets separately. After correction, any enrichment driven by a single interaction was marked insignificant by setting the *P*-value to 1. Genetic interaction enrichment observed within and between CORUM-annotated protein complexes is provided in Data S15. Results pertaining to genetic interaction enrichment within and between protein complexes is shown in Figures 2H–2J and S13B.

Genetic interaction purity score

The genetic interaction purity score refers to the fraction of positive or negative genetic interactions relative to the total number of observed genetic interactions within the same complex or between a pair of different complexes.[5,60,164] The genetic interaction purity score was normalized to the range of [-1,1], where -1 indicates that all genetic interactions within a specific complex or between a particular pair of complexes are exclusively negative. A purity score of 1 indicates all genetic interactions observed with a complex or between a pair of complexes are all positive.

The genetic interaction purity score distribution plots, shown in Figures 2J and S13B summarize the genetic interaction purity for protein complexes consisting of more than 5 screened pairs and that are enriched for genetic interactions (FDR < 0.10, hypergeometric test, Benjamini-Hochberg-corrected). To generate a null (background) purity score distribution, a random positive genetic interaction count was generated for each complex from a binomial distribution given the number of total genetic interactions in the complex and the background probability of observing a positive interaction (fraction of positive genetic interactions measured across all complexes). This analysis was completed both within and without the mitochondrial gene set. In Figure S13B, a set of smaller complexes that were subsets of larger complexes were excluded from the analysis results. This reduced complex set was formed based on overlap index scores computed for all pairs of complexes in the CORUM standard. The overlap index between two complexes is the number of shared genes divided by the size of the smaller complex. An overlap-index cut-off of 0.3 was applied here such that no two complexes with an overlap index of $\geq$ 0.3 were both included in the non-redundant set. To observe the contribution of mitochondria-related complexes to this result, all analyses were repeated after removing a set of complexes for which more than 50% member genes are mitochondrial. Genetic interaction purity scores are provided in Data S15. Results pertaining to genetic interaction purity scores within and between protein complexes are shown in Figures 2H–2J and S13B.

A genetic interaction profile similarity-derived functional hierarchy

Constructing a functional hierarchy

As described above (Hierarchical clustering of HAP1 genetic interaction profiles), we modified a previously described hierarchical clustering algorithm to the complete genetic interaction dataset to produce a set of uniformly sized gene clusters across layers of the dendrogram (Data S9)[150] (Zenodo: https://doi.org/10.5281/zenodo.15320010). The same algorithm was also used to cluster the subset of 3,784 genes derived from the same centroid-corrected, genetic interaction profile similarity network shown in Figure 1 and described above (Constructing a genetic interaction profile similarity network) to build a genetic interaction profile-based hierarchy of gene function (Data S16). Initial clustering organized these genes into 4 levels of hierarchically organized modules. Gene modules identified in level 4 of the hierarchy represented parent clusters in the hierarchy, which were separated into smaller child clusters in lower hierarchical levels, with level 1 of the hierarchy consisting of the smallest child gene clusters. Genes that did not belong to a functionally enriched cluster identified at level 2 of the hierarchy, were removed from the analysis. Functionally enrichment was defined as level 2 clusters whose gene members were statistically enriched (FDR < 0.1, hypergeometric test, Benjamini-Hochberg-corrected) for one or more GO bioprocess terms.[165] The resultant functional hierarchy consisted of 1,863 genes associated with functionally rich genetic interaction profiles. These genes were organized into 6 large parent clusters at level 4 of the hierarchy, 18 child clusters of level 3 of the hierarchy, 181 level 2 clusters and finally, 593 level 1 clusters (Data S16). Importantly all 1,863 genes were represented at each level of the functional hierarchy and a set of 98 genes that did not belong to a cluster at each of the 4 hierarchical levels were excluded from this analysis. This was a critical filtering step because it ensured that the same set of genes was examined at all levels of hierarchical study and that any differences observed (e.g. in genetic interaction density) were due to hierarchical structure at different levels and not differing sets of gene involved in the hierarchy at each level. As a result of these procedures: [1] all genes were members of only one cluster at each level of the hierarchy; [2] all clusters were strict subsets of their parent clusters one level above, and [3] each cluster was comprised of the union of its children clusters one level below. In addition, at the fourth layer, we identified one cluster including 292 genes that are associated with mitochondrial functions, which was later excluded for some analyses (where noted in Data S16).

To functionally characterize each level of the hierarchy, we performed enrichment analysis for co-annotated genes within the clusters at each layer of the hierarchy using the CORUM,[66] GO BP,[166] and cellular compartment[62] functional standards. At each layer, we calculated the fraction of gene pairs within each cluster that are co-annotated to the same term in a functional standard relative to the population of all possible gene pairs (i.e. 1,863 choose 2 = 1,734,453) and then performed a hypergeometric test to assess enrichment of genes within the same cluster to be co-annotated to the same functional term. Note that to distinguish functional signals that were specific and unique to each level of the hierarchy, the hypergeometric test was performed using only the additional gene pairs added by each hierarchical layer compared to the preceding layer. Specifically, this includes those gene pairs that are newly co-clustered at a given level of the hierarchy that were not previously co-clustered based on the descendant clusters. These sets of gene pairs are referred to as the "shell" at each level of the hierarchy, and enrichment fold-change and *P*-values are reported for these sets. This analysis showed that parent clusters at the fourth level of the hierarchy were specifically enriched for distinct subcellular compartments. Smaller level 3 clusters were enriched for more specific but distinct GO bioprocess terms while clusters identified at levels 1 and 2 of the hierarchy were uniquely enriched for distinct biological pathways and protein complexes (Figure S14B; Data S16). This analysis was also repeated after excluding 292 mitochondrial genes (Data S16). Analyses pertaining to the genetic interaction profile-based functional hierarchy are shown in Figures 3 and S14.

Measuring interaction density and magnitude at different levels of the functional hierarchy

The functional hierarchy was used to assess the density of genetic interactions at varying degrees of functional relatedness, where relatedness was defined by the hierarchy level described above. For each screened pair of genes, we noted whether it shared a genetic interaction and a level of functional relatedness of that pair, as defined by the most specific level of the hierarchy in which they shared membership to a common cluster. We used this measure for calculating interaction density at different levels of functional relatedness and assigned each pair to the level of their most specific common cluster. This prevented the density estimate at each level from being dominated by the trends observed at lower levels. Density was defined as the number of significant interactions meeting our standard significance threshold ($|qGI| > 0.3$; FDR < 0.1), divided by the number of screened pairs. Similarly, after binning all pairs of genes by their qGI score magnitude, we measured the fraction of pairs in each bin belonging to each hierarchy level using the most specific level available for each pair. To alleviate the potential bias introduced by mitochondrial genes, we also performed the same measurement excluding 292 mitochondrial genes identified in one of the 6 large clusters at the fourth layer. The results from this analysis are shown in Figures 3 and S14.

Genetic interaction enrichment within and between biological processes

We performed tests for enrichment of genetic interactions that occur within and between different biological process-level gene sets. Gene sets representing functionally coherent groups of genes for this analysis were based on the domains described in the section above "biological process annotation of the genetic interaction profile similarity network". For each domain, we compiled the list of library genes and query genes associated with that domain. For these analyses, we considered only those domains where at least three genes were represented in our library gene set and at least one gene was represented in the query gene set, which resulted in a total of 15 domains (Data S16). We tested each domain for enrichment of genetic interactions (within-domain analysis), and we also tested each pair of domains for enrichment of genetic interactions (between-domain analysis).

For each within-domain or between-domain gene pair set, the enrichment test was completed as follows. First, a standard threshold ($|qGI| > 0.3$ and FDR < 0.1) was applied to identify significant negative and positive genetic interactions. When computing enrichment statistics, the library gene universe was reduced to only those genes that overlapped the domains of interest, and the query gene universe was also restricted to only those genes that overlapped the domains of interest. Enrichments were calculated independently for positive, negative and total interactions (combined positive and negative) genetic interactions. *P*-values were derived from one-tailed hypergeometric tests, focusing on increased genetic interaction density relative to the background genetic interaction density. *P*-values were corrected using the Benjamini-Hochberg method applied to the within-domain and between-domain sets separately. After correction, any enrichment driven by a single interaction was marked insignificant by setting the p-value to 1. Genetic interaction enrichment observed within and between these bioprocess-level domains is provided in Data S16, and the related figure is plotted in Figure 3D.

Genetic Suppression Analysis

Suppression score

To define the subset of positive genetic interactions that may represent instances of genetic suppression, we formulated a suppression score for all positive interactions that satisfied the standard genetic interaction significance threshold (qGI > 0.3, FDR < 0.1).

$$S_{ij} = \frac{DMF_{ij} - SMF_{min}}{|SMF_{min}|}, if\ SMF_{min} < (-0.9)\ \&\ SMF_{min} < DMF_{ij}$$

$$S_{ij} = 0, otherwise$$

$$SMF_{min} = minimum(L_i, Q_j)$$

$$DMF_{ij} = L_i + Q_j + qGI_{ij}$$

Where *L* is the library gene single mutant fitness (in $\log_2$ fold-change) and *Q* is the query gene single mutant fitness (in $\log_2$ fold-change). Suppression scores for all positive interacting gene pairs are provided in Data S17. Results related to genetic suppression analysis are shown in Figures 4 and S15.

Functional enrichment analysis of genetic suppression interactions

To assess if genetic suppression gene pairs were more functionally related compared to gene pairs connected by positive genetic interactions in general, positive genetic interactions were sorted based suppression scores. FLEX[26] was then used to compute the precision of identifying gene pairs annotated to the same GO bioprocess term based on suppression scores at two different thresholds (suppression score > 0.5 and > 0.8) and for all positive genetic interactions (qGI > 0.3, FDR <0.1 and suppression score $\geq$ 0). Fold-enrichment for co-annotated gene pairs was calculated by dividing precision determined at the suppression score thresholds described above by the background precision (size of positive class divided by total number of gene pairs). The *P*-values comparing each set relative to background precision were determined by Fisher-exact tests. This analysis was also repeated after excluding mitochondrial genes. These results of this analysis are shown in Figure S15D.

HAP1 essential gene suppression interactions

We examined if HAP1 essential genes involved in genetic suppression interactions were more likely to be considered core or context-dependent essential genes based on the DepMap 20Q2 dataset (DepMap: depmap.org/portal). Positive interactions with a suppression score greater than 0.5 were defined as genetic suppression interactions. HAP1 essential genes were grouped into the following categories: [1] all HAP1 essential genes, [2] HAP1 essential genes involved in at least one suppression interaction, [3] HAP1 essential genes with positive genetic interactions, and [4] HAP1 essential genes with no suppression interactions. We then determined the percentage of cancer cell lines in the DepMap 20Q2 dataset that also depended on HAP1 essential genes from each category for viability. Cancer cell line essential genes were defined as genes that met a CERES score threshold of < -1, which corresponds to the median score of all essential genes in the DepMap data. Statistical significance was determined by Wilcoxon rank-sum tests between each pair of HAP1 essential gene groups. The same analysis was repeated excluding the mitochondria gene set. The results of this analysis are shown in Figures 4B and S15E.

Genetic interaction conservation

The following methods were used to evaluate conservation of genetic interactions between human HAP1 cells and the budding yeast, *S. cerevisiae*. For gene pairs screened more than once, we considered a genetic interaction if at least half of the screened pairs resulted in a significant genetic interaction score ($|qGI| > 0.3$, FDR < 0.1).

Conservation of genetic interaction density between biological processes

We classified human and *S. cerevisiae* genes into 15 distinct bioprocess functional groups (Data S18). For each pair of bioprocess groups, we calculated the negative and positive genetic interaction density between the corresponding gene sets in the HAP1 genetic network described in this study and the *S. cerevisiae* genetic interaction network.[5] Genes annotated to more than one bioprocess group were excluded from the analysis, and we only considered pairs of bioprocesses for which at least 100 gene pairs were tested for genetic interactions. Finally, we calculated the Pearson's correlation coefficient between the interaction density obtained in the HAP1 and *S. cerevisiae* genetic networks. The results of this analysis are provided in Data S18 and shown in Figures 5A and S16A.

Conservation of genetic interactions between human-yeast ortholog gene pairs

We used DIOPT (DIOPT: https://fgr.hms.harvard.edu/diopt)[103] to retrieve orthology mappings between human and *S. cerevisiae* genes and selected genes with 1:1 orthologs between both species or gene with more than one ortholog in human (i.e. N:1 orthology relationships, such that 1 gene in *S. cerevisiae* has N orthologs in human). Of all the gene pairs tested in HAP1 cells, 3.7% involved such selected genes. Next, we selected the gene pairs that were tested for genetic interactions in both HAP1 cells and *S. cerevisiae* and counted the number of genetic interactions identified only in HAP1 cells (i.e. HAP1-specific genetic interactions) and in both species (i.e. conserved genetic interactions). The results of this analysis are provided in Data S20 and shown in Figure 5B.

Conservation of genetic interaction profile similarity human-yeast orthologs

We measured the genetic interaction profile similarity for human gene pairs as explained above (see section, mapping the genetic interaction profile similarity network). Genetic interaction profile similarity values for *S. cerevisiae* gene pairs were downloaded from thecellmap.org.[5,63] For yeast gene pairs associated with multiple temperature-sensitive mutant alleles, the correlation values were averaged. We only considered gene pairs involving genes with a 1:1 or N:1 human to *S. cerevisiae* orthology relationship for which profile similarity data was available in both species. Next, we retrieved gene pairs within the top 5% of HAP1 profile similarity and determined the fraction of those pairs whose orthologs were within the top 5% similarity values in the *S. cerevisiae* genetic interaction profile similarity network. We calculated the same fraction for the remaining 95% of gene pairs in the HAP1 profile similarity network. Statistical significance was calculated using Fisher's exact test. The results of this analysis are show in Figures S19A and S19B.

Genetic interaction enrichment analysis among yeast-human conserved genes

We first selected gene pairs tested for genetic interactions in HAP1 cells whose ortholog pairs (with 1:1 or N:1 orthology relationships, see above) were also tested in *S. cerevisiae*.[5] For the sets of gene pairs with and without a genetic interaction in HAP1 cells, we calculated the fraction that showed a corresponding genetic interaction in *S. cerevisiae*. We derived the fold enrichment in the conservation of genetic interactions in yeast by calculating the ratio between both fractions and calculated the statistical significance using Fisher's exact test.

To calculate the conservation of genetic interaction in HAP1 cells, we used the same approach but starting from gene pair sets with and without a genetic interaction in *S. cerevisiae* and calculated the fraction of pairs which had a genetic interaction in HAP1 cells. We repeated the same calculations using: [1] 100 randomized genetic interaction networks respecting the network topology and compared the obtained fold enrichments to the result in the real genetic interaction network to obtain an empirical *P*-value; [2] Process-specific genetic interaction networks involving only pairs with at least a gene annotated to the corresponding biological process.

We followed the same approach to examine the conservation between *hPTAR1* and *yECM9* genetic interactions but restricted the gene pairs in HAP1 cells to those involving *PTAR1*, and the gene pairs in *S. cerevisiae* to those involving *ECM9*. *ECM9* genetic interactions were identified using SGA analysis described in the next section. Only reproducible *ECM9* genetic interactions identified in independent biological replicate screens were considered in this analysis. The results of these analyses are provided in Data S20 shown in Figures 5B–5E and S18.

Follow-up Experiments

Hc3716 cell proliferation assay

PELO KO hepatocytes were generated by transduction of Hc3716 cells with lentiCRISPR-v2(Puro)-based viral particles carrying the sgRNA sequence GGCTTACCACACACCATCGAGC. After selection with 2.5 ug/ml puromycin, clonal KO lines were isolated by limiting dilution and confirmed by western blotting (PELO antibody, Proteintech 105821-1-AP). To validate the PELO-SKIC2 negative interaction in targeted proliferation assays in Hc3716 cells, 30,000 WT or PELO KO cells were seeded per well in a 24 well plate and infected with lentiCRISPR-v2(Neo)-based lentiviral particles in the presence of 5 ul/ml polybrene. SKIC2 was targeted with a 1:1:1 mixture of viral particles each carrying one of 3 gRNAs (GAGTGCTCCACACCATGCAG, GTAACCCAGTATCTGGCCTG, AACAGATCTGAACACACGGG); control wells received viral particles lacking sgRNA. After 7 days of selection with 8 ug/ml G418, viability was assessed by MTT assay. Statistical analysis was performed using a one-way ANOVA followed by Tukey's post hoc test for multiple comparisons.

mTOR activity assays

For Figure S17B, wild-type and query mutant cell lines (*ANGPTL4*, *EMC6*, *FANCA*, *GSK3A*, *SLX1*, *C1orf112*, *PDCD5*, *TAPT1*, *VPS52*) were cultured in IMDM (Gibco), 10% FBS (Gibco) and 1X penicillin and streptomycin (Gibco) at 37°C with 5% CO_2. For immunoblots, 250k cells seeded in 12-well plates were lysed at 70-80% confluency directly in well using RIPA buffer [50 mM Tris-HCl (pH8.0), 150 mM NaCl, 2 mM EDTA, 1% NP-40, 0.5% sodium deoxycholate, 0.1% SDS with 1X Halt Protease and Phosphatase Inhibitor Cocktail (Thermo Fisher)]. 10 μg total protein was mixed with 6X loading buffer [375 mM Tris-HCl (pH7.4), 50% Glycerol, 6% SDS, 30% 2-Mercaptoethanol, 0.04% Bromophenol blue], and incubated at 95°C for 5 min. Samples were run on pre-cast gels (Bio-rad) and transferred to Nitrocellulose membranes using iBlot 2 Gel Transfer Device (Thermo Fisher). Membranes were blocked in 5% BSA/TBS-T and incubated overnight at 4°C with primary antibody against phospho-S6 Ribosomal Protein Ser240/244 (CST, #2215), S6 Ribosomal Protein (CST, #2317), phospho-Akt Ser473 (CST, #4060), and Akt (CST, #2920). Secondary antibody incubation was done for 1 hour at room temperature in dark using donkey anti-mouse IRDye® 680RD (Li-Cor, 926-68072) and donkey anti-rabbit IRDye® 800CW (Li-Cor, 926-32213). Membranes were visualized with Li-Cor Odyssey Classic instrument and ImageStudio was used for signal quantification. GraphPad Prism v.10 was used for statistical analyses.

For Figures S17C and S17D, HAP1 wild-type and query mutant cell lines (*GSK3A*, *CDKN2B*, *ANGPTL4*) were seeded at a density of 500,000 cells/well in a 6-well plate and cultured for 24 hours. The following day, cells were treated with 250 nM rapamycin (Selleckchem, Cat.#S1039) for 24 hours. On day 2, cells were subjected to amino acid starvation for 50 min using amino acid-free DMEM (Wisent, Cat.#319-004-CL), followed by amino acid refeeding for 10 min. Cells were then washed twice with ice-cold PBS and lysed on ice using RIPA lysis and extraction buffer (Thermo Fisher Scientific, Cat.# 89901) supplemented with Halt Protease and Phosphatase Inhibitor Cocktail (Thermo Fisher Scientific, Cat.#23227). Protein concentrations were quantified using the Pierce BCA Protein Assay Kit (Thermo Fisher Scientific, Cat.#23227). Cell lysates were mixed with NuPAGE LDS sample buffer (Invitrogen, Cat.# NP0007) and denatured at 95°C for 5 min. Proteins were separated using NuPAGE 4-12% Bis-Tris Mini Protein Gels (Invitrogen, Cat.#NP0323BOX) and transferred for immunoblotting. Primary and secondary antibodies and dilutions were as follows: Akt(pan)(40D4) mouse mAb at 1:1000 (Cell Signaling, Cat.#2920; RRID: AB_1147620); phospho-Akt1(Ser473)(D7F10) XP rabbit mAb at 1:1000 (Cell Signaling, Cat.#9018; RRID: AB2629283); p70 S6 kinase (49D7) rabbit mAb at 1:1000 (Cell Signaling, Cat.# 2708; RRID: AB_390722); phospho-p70 S6 kinase (Thr389) (108D2) rabbit mAb at 1:1000 (Cell Signaling, Cat.#9234, RRID: AB_2269803); b-actin (8H10D10) mouse mAb at 1:10,000 (Cell Signaling, Cat.#3700; RRID:AB_2242334); goat anti-mouse IgG (H+L) cross-adsorbed secondary Ab, HRP (Invitrogen, Cat.#A16072; RRID: AB_2534745); and goat anti-rabbit (H+L)-HRP conjugate (Bio-Rad, Cat.#170-6515; RRID: AB_11125142). Chemiluminescence was detected using the SuperSignal West Pico PLUS Chemiluminescence Substrate (Thermo Fisher Scientific, Cat.#34580) and images were acquired using the iBright FL1500 Imaging System (Invitrogen) in chemiluminescent mode.

yECM9/hPTAR1 *functional studies*

The following sections describe methods to validate *ECM9* as a yeast prenyltransferase important for prenylation and activation of Ykt6. The results from these experiments are shown in Figures 5G, S19C, S19D, and S19G.

Yeast strains

All strains used for SGA, yeast two hybrid analysis and complementation assays were derivatives of BY4741 or Y7092, the construction of which was described previously.[144] A temperature-sensitive allele of *ECM9*, TSQ3052 (*MAT*a *ecm9-5002::natMX can1Δ::STE2pr-Sp_his5; lyp1Δ; his3Δ1 leu2Δ0 ura3Δ0 LYS2*) was used as a query mutant for SGA analysis. Yeast complementation analysis was performed using Y16258 (*MAT* ***a****/a ECM9/ecm9Δ::natMX CAN1/can1Δ::STE2pr-Sp_his5; LYP1/lyp1Δ; HIS3/his3Δ1 LEU2/leu2Δ0 URA3/ura3Δ0*) or Y15767 (*MATa ecm9Δ::natMX abh1Δ::URA3 can1Δ::STE2pr-Sp_his5; lyp1Δ; his3Δ1 leu2Δ0 ura3Δ0 LYS2*) as indicated below.

Yeast Two Hybrid Analysis

Genes encoding the alpha and beta subunits of farnesyltransferase, and geranylgeranyl transferase type I-III were amplified by PCR from *S. cerevisiae* genomic DNA, using sequence specific primers fused to common sequences used for homologous recombination cloning.[167] Genes were cloned into DNA binding domain- and activation domain-fusion plasmids and two hybrid analysis was performed as described elsewhere.[167]

Synthetic Genetic Array (SGA) analysis to map genetic interactions for yeast ECM9

We constructed a hypomorphic, temperature-sensitive (TS) mutant of the yeast essential gene, *ECM9* (TSQ3052), in the SGA query strain background and screened it for genetic interactions against ordered arrays of 3,827 nonessential yeast deletion mutants and 786 TS alleles representing 560 yeast essential genes, as previously described.[5,168] All SGA selection steps were conducted at permissive temperature (22°C) except for the final selection of haploid double mutants, which were incubated at a semi-permissive temperature (26°C) prior to imaging. Genetic interactions were identified and measured using the quantitative SGA genetic interaction score, as described elsewhere.[5,60] *ECM9* genetic interactions are provided in Data S20.

PTAR1-RABGGTB complementation assay

An *ECM9* heterozygous deletion strain (Y16258) harboring a low-copy vector control plasmid with a *URA3* selection marker (plasmid P13744) or the same plasmid expressing human *PTAR1* and *RABGGTB* (plasmid P13719) genes from the galactose-inducible *GAL1* promoter were sporulated in liquid sporulation medium for 1 week, as described elsewhere.[168] Asci were digested with Zymolyase and tetrads were dissected onto YEPD and YEPGalactose and grown 4 days at 30°C. Plates were photographed and replica plated onto selective YEPD or YEPGalactose medium supplemented with neurothrecin as well as synthetic defined medium lacking uracil to follow the segregation patterns of knockout alleles relative to the fitness phenotype, as described elsewhere.[19]

ABHD16A and ABHD17B complementation assay

Overnight cultures of an *ecm9Δabh1Δ* double deletion mutant (Y15767) harboring a low-copy vector control plasmid with a *URA3* selection marker or the same plasmid expressing human *ABHD16A* (plasmid P13708), human *ABHD17B* (plasmid P13712) or yeast *ABH1* (P13713) genes from the galactose-inducible *GAL1* promoter, were serially diluted and spotted onto selective agar media lacking uracil supplemented with 2% glucose or 2% galactose as indicated. Strains were grown for 2 days at 30°C and imaged.

Palmitoylation Detection by mPEG replacement chemistry

Denatured, whole-cell yeast protein extracts were subjected to three chemical steps to replace thioester-linked palmitoyl-modifications with the methoxypolyethylene glycol maleimide (mPEG) (Sigma-Aldrich 712469): [1] blockade of free thiols with N-ethylmaleimide (NEM), [2] treatment with neutral pH hydroxylamine to release thioester-linker modifications (e.g. palmitoylation), restoring thus the cysteinyl thiol and [3] modifying the newly exposed thiols with the 10 kDa thiol-reactive mPEG reagent, resulting in a size-shift for proteins having acylated cysteines. In practice, Steps 2 and 3 were combined, i.e. hydroxylamine treatment and mPEG reaction were done concurrently. The treated extracts were subjected to Tricine SDS-PAGE and then Western blotting, using a rabbit polyclonal anti-Ykt6 antiserum and aHRP-conjugated goat anti-rabbit secondary antibody. Final visualization was via enhanced chemiluminescence (ECL) and x-ray film exposure.

The early steps of the acyl-mPEG exchange protocol, closely track the previously described small-scale acyl-biotinyl exchange (ABE) protocol.[169] 1 x 10^8 cells were harvested by centrifugation from log-phase yeast cultures growing in YPD media (1% yeast extract, 2% peptone, 2% glucose) with the cell pellet resuspended into ice-cold 200 ul Lysis Buffer (LB: 150 mM NaCl, 50 mM Tris/Cl, 5 mM EDTA pH 7.4), supplemented with 10 mM NEM (Sigma) and 2xPI (1xPI: 1mM PMSF, and 0.25 mg/ml each of antipain, leupeptin, pepstatin, and chymostatin). A 200 ul volume of glass beads (Sigma) was added and lysis was effected with five 45 sec intervals of vigorous vortex mixing, interspersed with 2 min rest periods on ice. The lysate was decanted away and combined with a 300 ul LB/10 mM NEM/1xPI quick wash of the beads. To solubilize cellular membranes, Triton X-100 (Anatrace) was added to 1.7% and the lysates were subjected to gentle mixing at 4°C. Protein from a 150 µl portion of the lysate was collected by chloroform-methanol (CM) precipitation.[170] The scaled-down version of the CM precipitation used here involves 8-fold reduced volumes relative to the previously detailed CM precipitation,[170] allowing the use of 1.5 ml screw-cap centrifuge tubes and a microfuge. The resulting protein pellet was solubilized with 30 ul SDS Buffer (SB: 4% SDS, 50 mM Tris/Cl, 5 mM EDTA, pH 7.4) with 10 mM NEM and incubated at 37°C for 10 min to denature protein. The sample was then diluted with 120 ul LB supplemented with 1 mM NEM, 0.2% Triton X-100, and 1xPI and further incubated for 60 min at 4°C. Three sequential CM precipitations were then used to fully remove residual NEM. After the first two precipitations, protein pellets were dissolved into 30 ul SB and then diluted with 120 ul LB with 0.2% Triton X-100. Following the third CM precipitation, protein pellets were dissolved in 70 ul SB, which was used for the two experimental conditions, + and –mPEG. For the +mPEG condition, a 15 ul of the sample was diluted into 60 ul 0.8 M hydroxylamine (Sigma-Aldrich 467804), 150 mM NaCl, 2 mM mPEG, 0.2% Triton X-100, 1xPI. For the –mPEG control condition, 15 ul was diluted into 60 ul 0.8 M hydroxylamine, 150 mM NaCl, 0.2% Triton X-100, 1xPI. Samples were incubated at room temperature with gentle rotation for 1 hour. Finally, 75 ul LB was added and samples were subjected to a final CM precipitation with the protein pellet being dissolved into sample buffer for gel loading.

HAP1 chemical-genetic interaction profiling of the small molecule, ABD957

We performed a genome-wide chemical-genetic interaction screens with ABD957, a small molecule inhibitor of the *ABHD17* subset of depalmitoylases. Chemical-genetic interaction screens were performed as described above (see section annotating functions using the HAP1 interaction profile similarity network) and elsewhere.[153] ABD957 negative and positive chemical-genetic interactions were scored as previously described.[154]

Analysis of genetic interactions underlying cancer gene dependencies

Expression dependency (ED) score analysis

For each unique gene pair tested in the HAP1 nonredundant genetic interaction dataset (Data S4), we extracted CRISPR gene effect fitness scores (Chronos score, DepMap 22Q4) and gene expression [$\log_2$(TPM+1)] derived from a panel of cancer cell lines examined

in the DepMap 22Q4 dataset (DepMap: depmap.org/portal). We then measured the correlation (PCC) between cancer cell line fitness scores associated with one gene and expression of the second gene across the same panel of cancer cell lines. In doing so, we generated two PCC and *P*-values using scipy.stats.pearsonr[171] for each pair of genes tested based on Gene A fitness-Gene B expression and Gene A expression-Gene B fitness. Gene pairs were filtered based on correlation and statistical thresholds (|PCC|>0.1 and *P*-value < 0.01)(Data S21). Reciprocal gene pairs that satisfied these thresholds but exhibited PCC values of opposite signs were also removed. We referred to the correlation between gene pair fitness and expression measured across a panel of cancer cell lines as a gene pair Expression Dependency (ED) score.

Comparing expression dependency (ED) and quantitative genetic interaction (qGI) scores

We performed an overlap analysis to compare gene pairs associated with a significant negative or positive ED score, described above, to the set of 41,773 HAP1 gene pairs that showed a positive genetic interaction and 47,052 gene pairs that exhibited a negative genetic interaction at the standard confidence threshold (|qGI| > 0.3, FDR < 0.1). A small subset of HAP1 query genes (*GFPT1, CDKN2B, ITGAV, SGF29, TAPT1, VPS52, SP1, BCL2, NDUFA2*) each accounted for a disproportionate fraction (~2%) of gene pairs that exhibited significant qGI and ED scores and gene pairs involving this subset of query genes were excluded from this analysis. Among all tested gene pairs (~4 million) in the HAP1 non-redundant genetic interaction dataset (Data S4), we identified a total of 246,840 gene pairs with significant positive ED score and 218,484 gene pairs with a significant negative ED score (Data S21).

A hypergeometric test was used to evaluate the significance of overlap for all possible ED and qGI score combinations (positive ED-negative qGI, positive ED-positive qGI, negative ED-positive qGI, negative ED-negative qGI). In addition, functional co-annotation enrichment analysis was performed using GO biological process, co-complex, and PPI functional standards, and paralog gene lists, described above. The statistical test universe included the set of gene pairs tested for genetic interactions and represented in each functional standard. ED scores for all tested gene pairs are provided in Data S21 and results pertaining to these analyses are shown in Figures 6, S20A, and S20B.

TCGA Pan-cancer analysis of co-occurring mutations with TP53

The cBioPortal for Cancer Genomics repository was used to investigate genetic alterations within the Cancer Genome Atlas (TCGA). A total of 32 distinct cancer types, comprising 10,967 samples (corresponding to 10,953 patients), were subjected to analysis. Our analysis focused on TP53 and 20 genes identified in positive genetic interactions with TP53. Mutation and copy number variant data for those 21 genes were extracted from the cBioPortal database. The co-occurrence of mutations or copy number changes in genes in the positive GI set with TP53 mutations were tested 2 different ways: (1) tracking only co-occurrence of mutations, and (2) tracking co-occurrence of either mutations or copy number. For both approaches, co-occurrence of mutation or copy number deletion in TP53 and each of the candidate genes with positive genetic interactions in HAP1 was tested for enrichment using Fisher's exact test. The Benjamini-Hochberg method was used to correct for the multiple hypothesis testing and calculate false discovery rate (FDR). Results pertaining to these analyses are shown in Figure S20C.

COMPARING GENETIC INTERACTION AND CO-ESSENTIALITY NETWORKS

Jaccard network overlap analysis

To compare functional information captured by the HAP1 genetic interaction profile similarity and DepMap co-essentiality networks, we first subsampled the DepMap co-essentiality network (20Q2 release) by randomly sampling two groups of cancer cell lines, with each group consisting of 298 non-overlapping cell lines. We then measured Pearson's correlation coefficients (PCC) based on CERES score essentiality scores for all possible gene pairs in each cell line group. The resultant PCC matrices were binarized at different thresholds (PCC ranging from 0.2 to 0.5 at intervals of 0.01). At each threshold, the Jaccard index between connected genes in the two DepMap networks was computed as follows:

$$J(N1, N2, t) = \frac{E(N1, t) \cup E(N2, t)}{E(N1, t) \cap E(N2, t)}$$

Here, J is the Jaccard index between networks N1 and N2 at threshold t and E is the set of edges of a network N at threshold t.

This process was repeated 10 times using different random resampling of DepMap cancer cell lines. We also computed the Jaccard index between each randomly sampled DepMap co-essentiality network and the HAP1 genetic interaction profile similarity network. The 10 DepMap-DepMap network Jaccard indices and the 20 DepMap-HAP1 genetic profile network Jaccard indices were plotted, where the mean at each threshold is indicated by the solid line and the minimum and maximum at each threshold are indicated with the dotted line. The results of this analysis are shown in Figure 7A.

Genetic interaction profile- vs. DepMap co-essentiality-derived network clusters. We evaluated clusters derived from the HAP1 genetic interaction profile similarity network for support in the DepMap-derived co-essentiality network. To accomplish this, we applied the hierarchical clustering algorithm described in the section "hierarchical clustering of HAP1 genetic interaction profiles" to the complete genetic interaction dataset (298 query cell lines x 17,804 library genes) to generate two layers of "Global" gene clusters (L2 parent clusters and L1 child clusters), which are provided in Data S9. For each L1 child cluster from this analysis, we computed a cluster statistic reflecting the normalized within-cluster pairwise similarity. This statistic was computed by applying Fisher's z-transformation to the pairwise Pearson correlation coefficient for each within-cluster gene pair. The resulting z-transformed similarity

statistics were then averaged per cluster to derive a mean correlation z-score for each cluster. This process was completed for each HAP1 network-derived cluster. Analogous statistics were computed in the DepMap co-essentiality network each of the HAP1 network-derived cluster to derive a z-score reflecting the support for that cluster in the DepMap co-essentiality network. Clusters were then grouped based on the combination of their HAP1 z-score and their DepMap z-score for downstream analyses. Data associated with this analysis is provided in Data S22 and shown in Figures 7B–7E, S21A, and S21B.

The process described above starts with cluster definitions derived from the HAP1 profile similarity network. We also completed a reciprocal process starting from clusters derived from the same clustering algorithm applied to the DepMap co-essentiality network. The resulting clusters were then evaluated for support in the HAP1 profile similarity network. The figures resulting from this analysis are presented in Figures S21C–S21E and are also included in Data S22.

Several other statistics were also computed for each of the clusters derived from the process above. These features include the average SMF for genes in each cluster, the number of publications citing genes in the cluster, degree of annotation for genes in each cluster, enrichment for GO biological processes for each cluster, enrichment for PPI within the cluster, average gene expression level and variance within the cluster, and the DepMap average single mutant phenotype and standard deviation. All cluster statistics related to this analysis are reported in Data S22. Gene features used for this are also further described in Data S14. The results of this analysis are provided in Data S22 and shown in Figures 7B–7E and S21A–S21E.

An integrated functional network. The complete DepMap co-essentiality profile similarity network was generated by computing Pearson Correlation Coefficient (PCC) between all pairs of gene essentiality profiles derived from analysis of all cell lines tested in the DepMap 20Q2 dataset (DepMap: depmap.org/portal). NA values were replaced with gene-wise average CERES scores prior to network creation. The HAP1 genetic interaction profile similarity network was constructed from the centroid-corrected genetic interaction dataset, as described above (see section constructing a genetic interaction profile similarity network).

To construct an integrated network, we normalized the HAP1 GI network using the RPCO method with SNF hyperparameters k=5, α=3. Similarly, we applied RPCO with SNF hyperparameters k=5, α=5 to normalize the complete DepMap co-essentiality profile network. Normalized networks were then filtered at a similarity threshold corresponding to the 99.85th percentile such that gene pairs with similarity values above this threshold were retained as edges, while gene values below this similarity threshold were removed. Finally, RPCO-normalized and filtered HAP1 genetic interaction profile similarity and DepMap co-essentiality profile similarity networks were integrated using the BIONIC network integration method.[114] Briefly, BIONIC was run unsupervised for 10,000 epochs with a batch size of 2048, learning rate .0001, and integrated gene embedding size of 4096. The graph attention network (GAT) encoders were set to have an internal embedding size of 256 with 10 attention heads. One GAT layer was used for each input network encoder. All other hyperparameters were unchanged from the previously described default settings.[114] The resulting matrix contains 19274 genes with embedding dimension 4096.

Functional evaluation of integrated vs. individual networks. The resulting integrated network was functionally evaluated using the FLEX tool, as previously described.[26] Briefly, FLEX was used to produce global precision-recall curves based on CORUM complex and GO biological process (BP) functional standards for the integrated network as well as the individual HAP1 genetic interaction profile and DepMap co-essentiality profile networks. Also, FLEX was used to produce per-functional module (defined by specific terms in the GO (BP) and CORUM complex standards) area under the PR curve (AUPRC) scores for each standard. Specifically, for each module in the protein complex or GO BP functional standard, gene pairs with both genes annotated in that module are considered positive examples and gene pairs with only one gene annotated in that module are negative examples in calculating a per-module AUPRC score. A higher per-module score indicates higher pair-wise gene similarities within the module relative to between-module pairs. The results of this analysis are provided in Data S22 and shown in Figures 7F, 7G, S21F, and S21G.

ESTIMATING SIZE OF A COMPLETE HAP1 GENETIC INTERACTION NETWORK

Total number of genetic interactions

To estimate the size of a complete genetic interaction network, we considered only the subset of ~11,000 genes that are expressed in in HAP1 cells [$\log_2$(TPM+1) > 1](Data S2). The number of total genetic interactions (i.e. negative + positive interactions) was estimated by multiplying the total number of possible expressed gene pairs (11,000 choose 2 = ~60,500,000 possible gene pairs) by the average genetic interaction density per library gene (Data S14). Thus, the estimated size of a complete HAP1 genetic interaction network is ~1.4 million genetic interactions (60,500,000 gene pairs x 0.0226 average interaction density).

Extreme synthetic lethal and suppressor interactions

The current HAP1 genetic interaction network consists of 3,341 extreme negative, synthetic lethal interactions. Considering the total number of expressed gene pairs tested for genetic interactions (222 query genes x ~11,000 expressed library genes = ~2,442,000 gene pairs), this translates to a synthetic lethal interaction density of ~0.14% (3,341 / ~2,442,000 HAP1 gene pairs x 100%). Thus, we estimate that a complete HAP1 genetic interaction network will consist of ~85,000 extreme synthetic lethal interactions (i.e. ~60,500,000 expressed gene pairs x 0.0014 interaction density).

The current HAP1 genetic interaction network consists of 1,843 extreme positive, suppression interactions (suppression score > 0.5) where the double mutant fitness is at least 50% greater than the fitness associated with the sickest single mutant of a given gene pair. Considering the total number of expressed gene pairs tested for genetic interactions (222 query genes x

~11,000 expressed library genes = ~2,442,000 gene pairs), this translates to a suppression interaction density of ~0.075% (1,843 / ~2,442,000 HAP1 gene pairs x 100%). Thus, we estimate that a complete HAP1 genetic interaction network will consist of ~45,000 extreme suppression interactions (i.e. 60,500,000 expressed gene pairs x 0.00075 interaction density).

QUANTIFICATION AND STATISTICAL ANALYSIS

Details of all quantification and statistical analyses are provided within the relevant subsections of the method details. Custom analytical methods developed in this study are described therein and are available via the link provided in the additional resources section.

ADDITIONAL RESOURCES

Supplementary Information for this manuscript, including supplemental figures, STAR Methods, code and Data S1–S24, are also available from:

Boone lab: https://boonelab.ccbr.utoronto.ca/supplement/billmanncostanzo2026/
Mendeley Data: https://doi.org/10.17632/bpcpfns6vb.1
Zenodo: https://doi.org/10.5281/zenodo.15320010
The HAP1 genetic interaction network and data can be also browsed via our companion databases:
https://thecellmap.org[63,64]
https://crisprdb.ccm.sickkids.ca/

CellPress
OPEN ACCESS

Supplemental figures

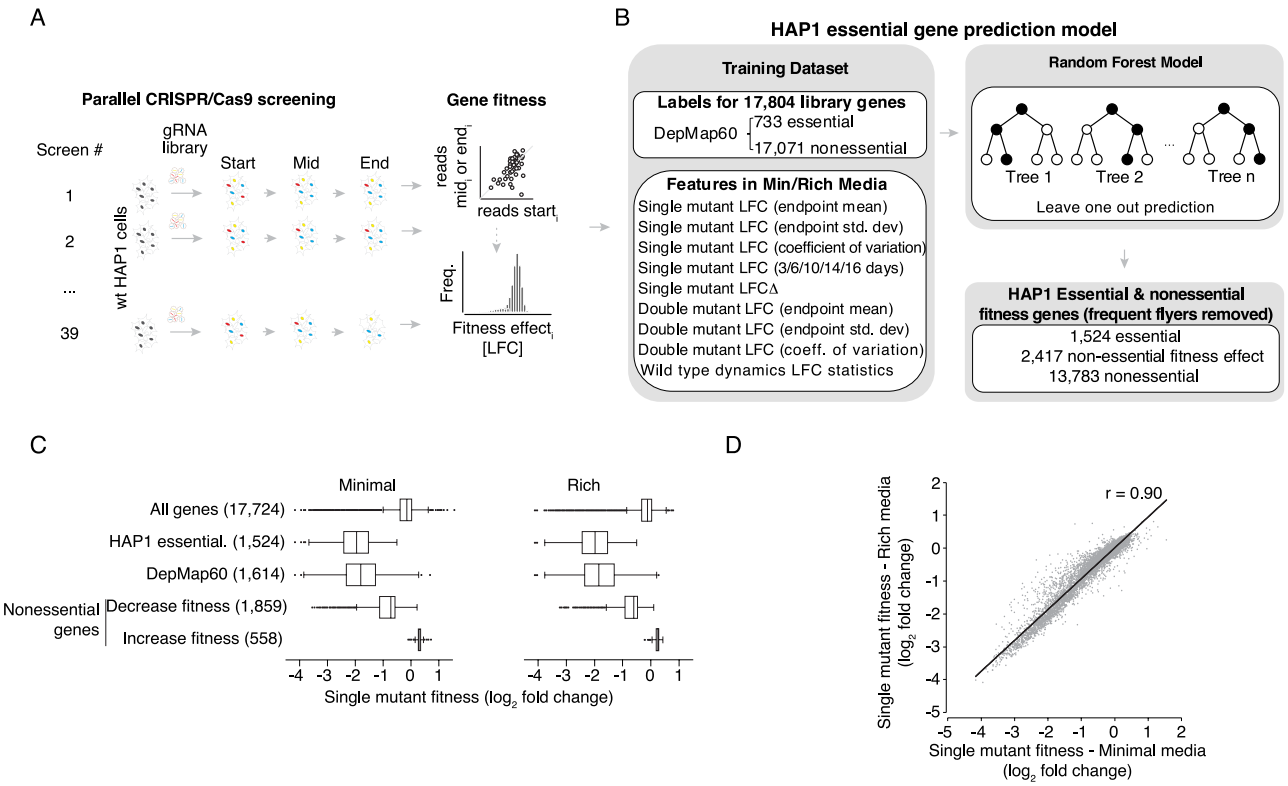

Figure S1. Identifying essential genes and measuring single mutant fitness in HAP1 cells, related to STAR Methods

(A) Experimental workflow for genome-scale pooled CRISPR screens in parental HAP1 cells with the TKOv3 library to measure single mutant fitness (LFC, $\log_2$ fold change).

(B) Workflow for generating a random forest model to identify 1,524 HAP1 essential and 2,417 nonessential genes with fitness phenotypes.

(C) Boxplots showing the distribution of single mutant fitness phenotypes for HAP1 genes grouped according to the indicated categories. DepMap60 includes genes that were classified as essential (CERES < −0.5) in at least 60% of cell lines tested in the DepMap 20Q2 dataset. The number of genes in each category is indicated in brackets. Individual perturbation of ~22% (3,941/17,724) of library genes significantly altered HAP1 cell fitness.

(D) Scatterplot of single mutant fitness effects (mean LFCs) derived from parental HAP1 screens in rich (n = 18) or minimal (n = 21) media. Single mutant fitness measurements derived from both growth conditions were highly correlated, with only a few genes showing significant condition-specific growth phenotypes (~0.2%, 38 genes).

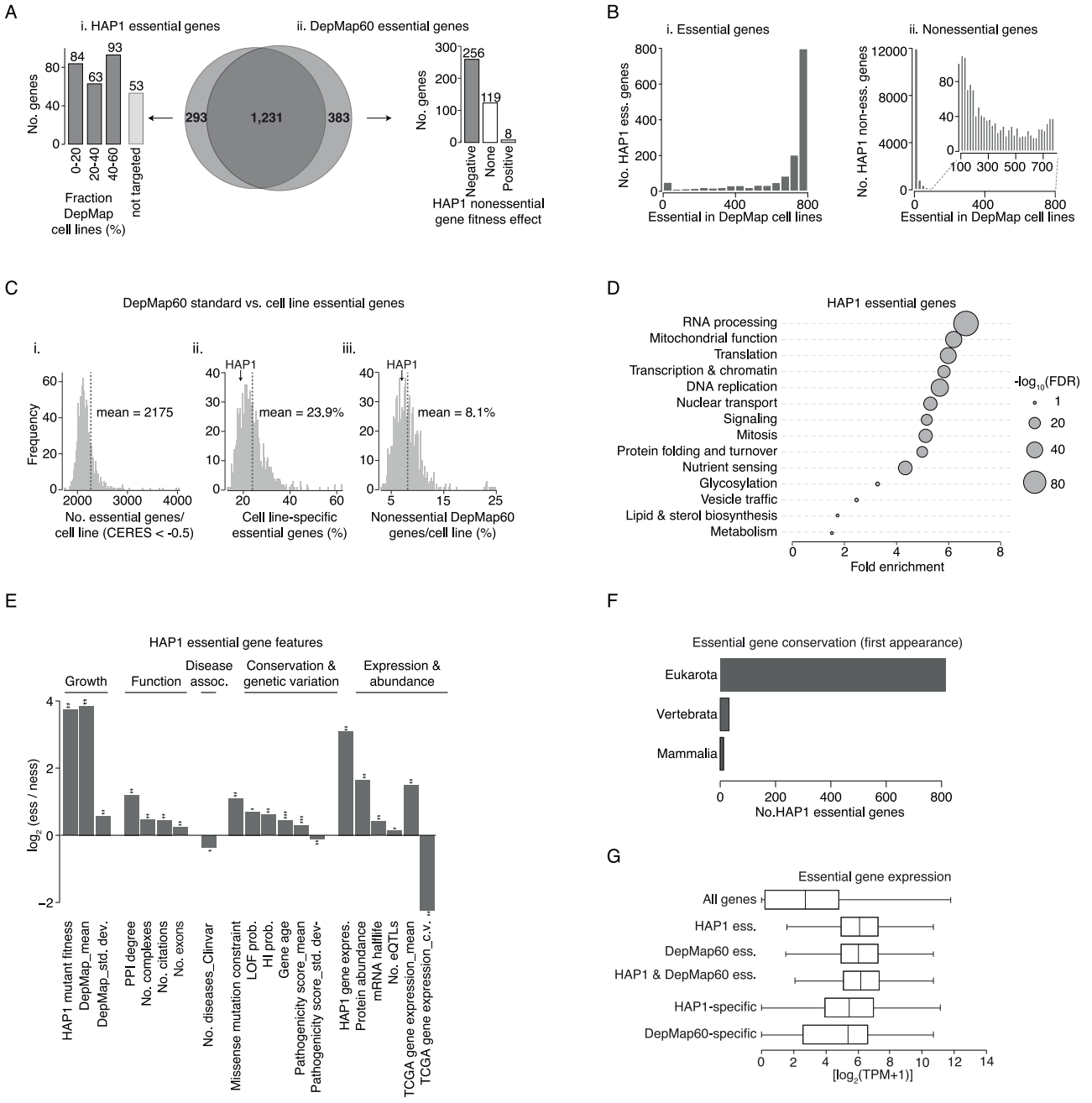

Figure S2. Characterization of HAP1 essential genes, related to STAR Methods

(A) Venn diagram showing the overlap between HAP1 essential genes and DepMap60 genes (i.e., genes that were classified as essential (CERES < −0.5) in at least 60% of cell lines tested in the DepMap 20Q2 dataset). Approximately 81% (1,231/1,524) of HAP1 essential genes are also required for the viability of most DepMap cancer cell lines. (i) Bar plot reporting the number of HAP1-specific essential genes (293 genes) that show DepMap essential phenotypes (mean CERES < −0.5) in the indicated fraction of DepMap cell lines. Genes not targeted by DepMap CRISPR libraries are indicated. (ii) Bar plot reporting the number of DepMap60-specific essential genes (383 genes) exhibiting fitness phenotypes in HAP1 cells. Negative denotes a single mutant fitness defect in HAP1 cells. Positive indicates a mutant with increased fitness relative to WT HAP1 cells.

(B) Distributions showing the number of HAP1 essential genes (i) and nonessential genes (ii) that exhibited a similar phenotype in DepMap cell lines (number of DepMap cell lines for which CERES < −0.5).

(C) (i) Distribution illustrating the percentage of essential genes (CERES < −0.5) per DepMap cell line. Dotted line indicates the average number of essential genes per cancer cell line in DepMap. (ii) Distribution showing the percent of DepMap cell line-specific essential genes per cell line. Dotted vertical line indicates the average percentage of cell line-specific essential genes identified in a given DepMap cancer cell line. The percentage of HAP1-specific essentials is indicated. (iii) Distribution illustrates the percentage of DepMap60 genes that are nonessential (CERES > −0.5) in a particular cancer cell line. The average percentage of

(legend continued on next page)

DepMap60 genes that are nonessential for viability in a specific cancer cell line and the percentage of DepMap60 genes nonessential in HAP1 cells are indicated (dotted lines).

(D) Functional enrichment among HAP1 essential genes. Reactome pathway terms, ranging in size from 10 to 300 genes,[172] statistically enriched (hypergeometric test, Benjamini-Hochberg-corrected FDR < 0.2) among HAP1 essential genes, are summarized according to the functional descriptions shown.

(E) Sequence, functional, and evolutionary properties significantly associated with HAP1 essential genes relative to HAP1 nonessential genes (ess/noness). * Indicates level of statistical significance (*$p < 10^{-3}$, **$p < 10^{-10}$, Wilcoxon rank-sum).

(F) Boxplot showing the conservation of HAP1 essential genes across indicated evolutionary classes.

(G) Boxplot indicating average gene expression values ($\log_2$ [TPM + 1]) for the indicated gene sets broken down by fitness phenotype categories.

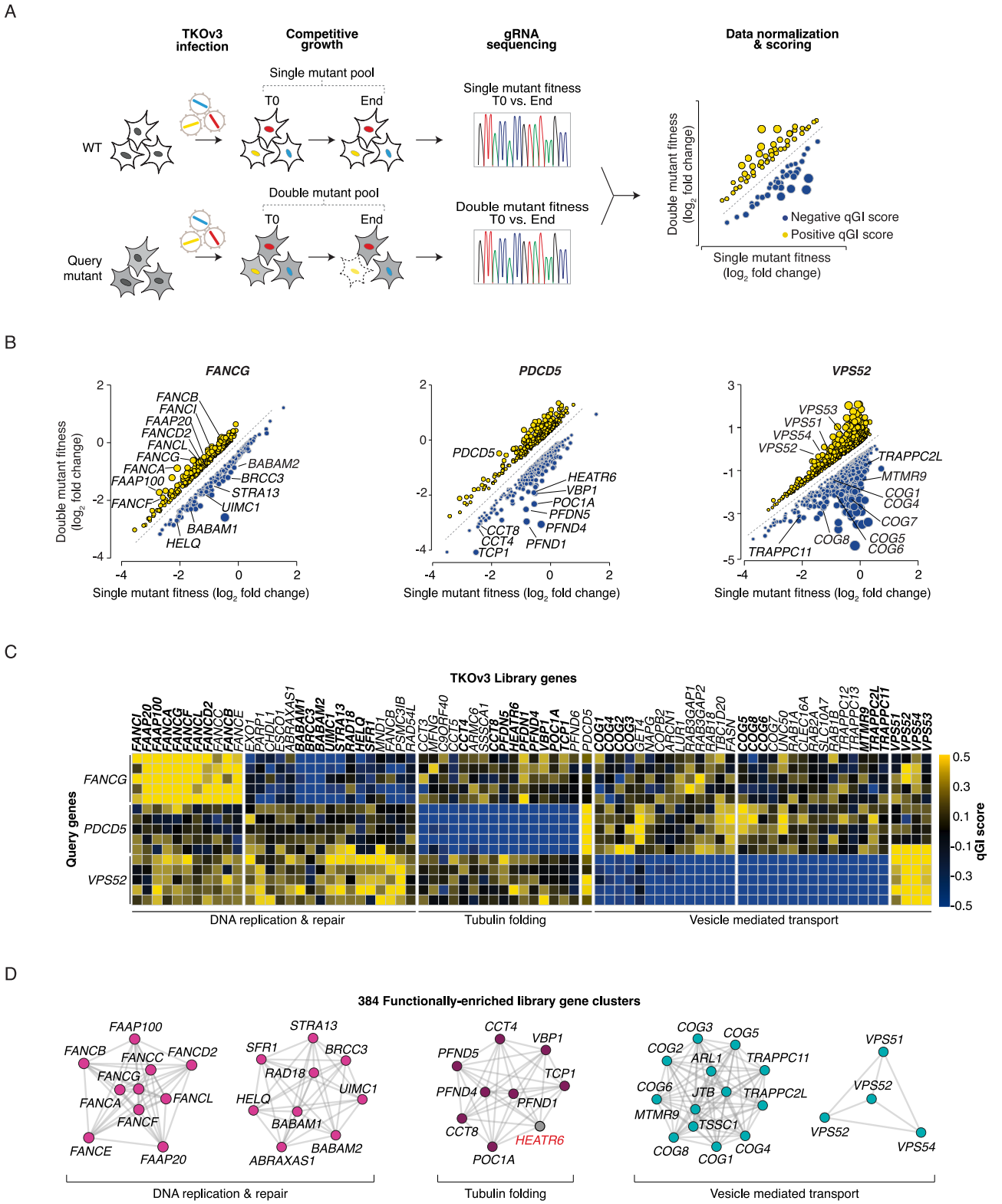

Figure S3. Genome-scale genetic interaction analysis in HAP1 cells, related to Figure 1 and STAR Methods

(A) Diagram of genetic interaction analysis pipeline in HAP1 isogenic cell lines. The quantitative genetic interaction (qGI) score is based on the difference between log fold change measurements for a given library gene in the query mutant (i.e., double mutant) versus WT (i.e., single mutant) cell populations.

(legend continued on next page)

(B) Scatterplots depicting genetic interactions for the indicated query genes. Negative (blue) and positive (yellow) genetic interactions that satisfied a standard genetic interaction threshold (|qGI| > 0.3, FDR < 0.1) are shown. Specific negative and positive interactions identified in each screen are indicated.
(C) Heatmap of qGI values for selected reproducible genetic interactions (columns) from biological replicate screens (n = 5) for the indicated query genes (rows). Negative qGI scores are shown in blue and positive qGI scores in yellow. Genes labeled in (B) are indicated in bold face. Functions enriched among specific groups of library genes are indicated.
(D) Examples of functionally enriched gene modules derived from clustering of the entire genetic interaction dataset. Node color represents shared general function, and the poorly characterized *HEATR6* gene is shown in red.

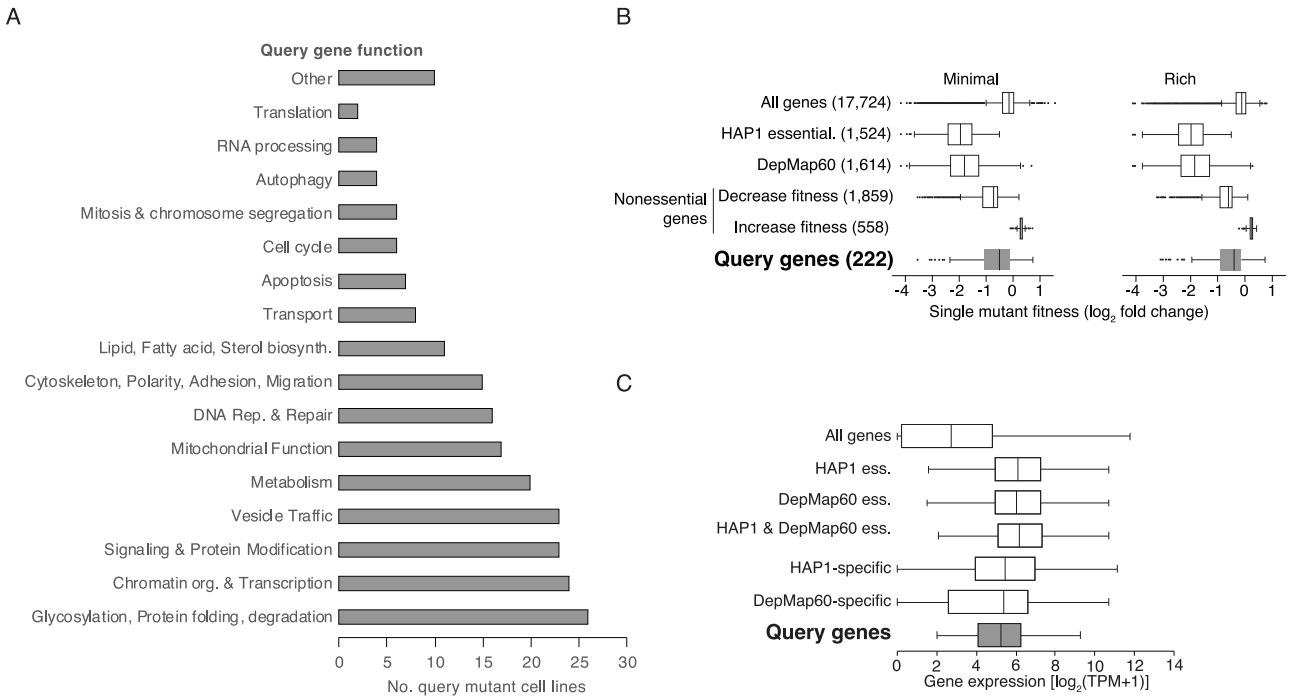

Figure S4. Characterization of HAP1 query mutant cell lines, related to STAR Methods

(A) Functional distribution of 222 query gene mutant cell lines screened on a genome-wide scale for genetic interactions in HAP1 cells.

(B) Boxplots showing the distribution of single mutant fitness effects for HAP1 genes grouped into the indicated fitness categories grown in the minimal or rich medium. Query genes are indicated in bold and gray boxplots. The number of genes in each category is indicated in brackets.

(C) Boxplot indicating average gene expression values (log_2 [TPM + 1]) for the indicated gene sets broken down by fitness categories. Query genes are indicated in bold and gray boxplots.

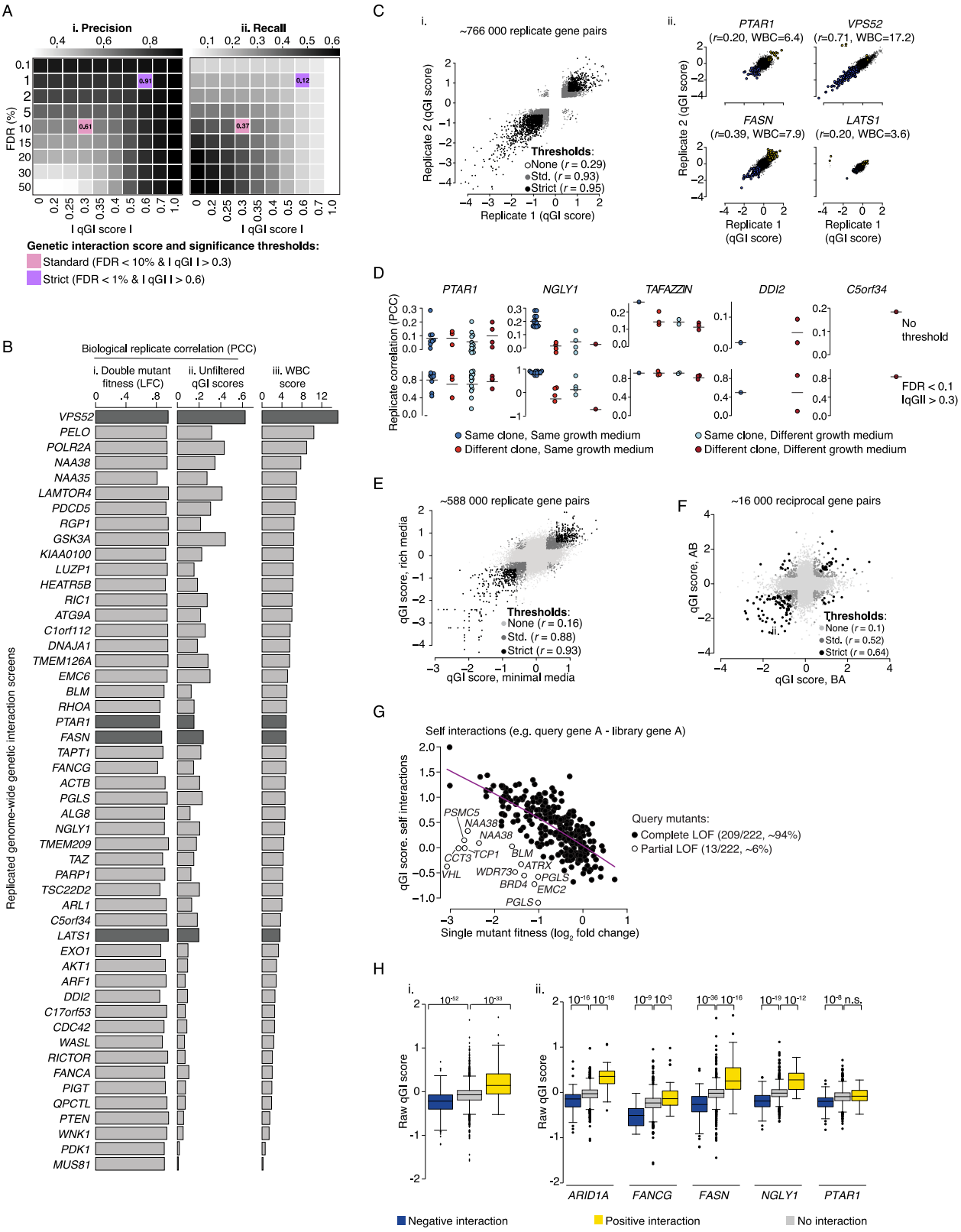

(legend on next page)

Figure S5. Data quality and reproducibility, related to STAR Methods

(A) Heatmap illustrating precision and recall estimates derived using an MCMC approach based on a set of screens with at least 4 replicates each. (i) Precision and (ii) recall estimates are plotted at 90 effect size (qGI score) and FDR cutoffs, as described (see STAR Methods). Standard (pink) and strict (purple) qGI score and FDR thresholds used to filter the raw genetic interaction dataset for large-scale data analysis and detailed mechanistic follow-up, respectively, are indicated.

(B) Scatterplot showing qGI scores for ~766,000 independent replicate gene pairs derived from independent replicate screens for 50 query mutant cell lines. Biological reproducibility analysis from screens performed for the indicated query genes (range n = 2–5). Bar plots showing the average PCC based on all independent replicates for (i) LFCs/double-mutant fitness, (ii) unfiltered qGI scores, and (iii) within-between correlation (WBC) scores.[173] Dark gray bars indicate query genes that are highlighted in (C).

(C) (i) Scatterplot of qGI scores for all replicate gene pairs tested in this study. PCCs were computed after applying the indicated confidence thresholds. (ii) Scatterplots of qGI scores derived from replicated screens with the indicated query gene mutants. Correlation and WBC statistics correspond to the specific pair of replicate screens shown in the plot.

(D) Biological reproducibility analysis from screens performed using combinations of different cell line clones and growth medium for the indicated query genes.

(E) Scatterplot of qGI scores for the same gene pairs measured in different media conditions. PCCs were computed after applying the indicated confidence thresholds.

(F) Scatterplot of qGI scores between reciprocally tested gene pairs. PCCs were computed after applying the indicated confidence thresholds.

(G) Scatterplot illustrating the correlation between HAP1 single mutant fitness and genetic interaction score (qGI) for genes with "self"-genetic interactions. The magnitude of positive self-interaction scores is positively correlated with single mutant fitness of the query gene, indicating that most query cell lines carry complete LOF mutations in the intended query gene.

(H) Boxplots showing results of re-screening 5 query genes from our genome-wide dataset using an independent CRISPR-KO library that targeted ~1,200 genes with ~30 gRNAs/gene (i.e., ~37,000 gRNAs in total) (Data S6). These gRNAs were not present in the TKOv3 library but targeted genes that showed significant genetic interactions with at least one of the 5 selected query genes in the TKOv3 library. (i) Boxplot shows the distribution of all unfiltered qGI genetic interaction scores derived from screens using an independent gRNA library for groups of gene pairs that showed a negative (blue), positive (yellow), or no interaction (gray) in screens using the TKOv3 gRNA library. (ii) Boxplot showing the distribution of qGI genetic interaction scores derived from screens using an independent gRNA library and involving specific query genes that showed a negative (blue), positive (yellow), or no interaction (gray) in screens using the TKOv3 gRNA library (right). Differences of negative and positive interaction distributions from the no interaction distribution were measured using a two sided Wilcoxon rank-sum test.

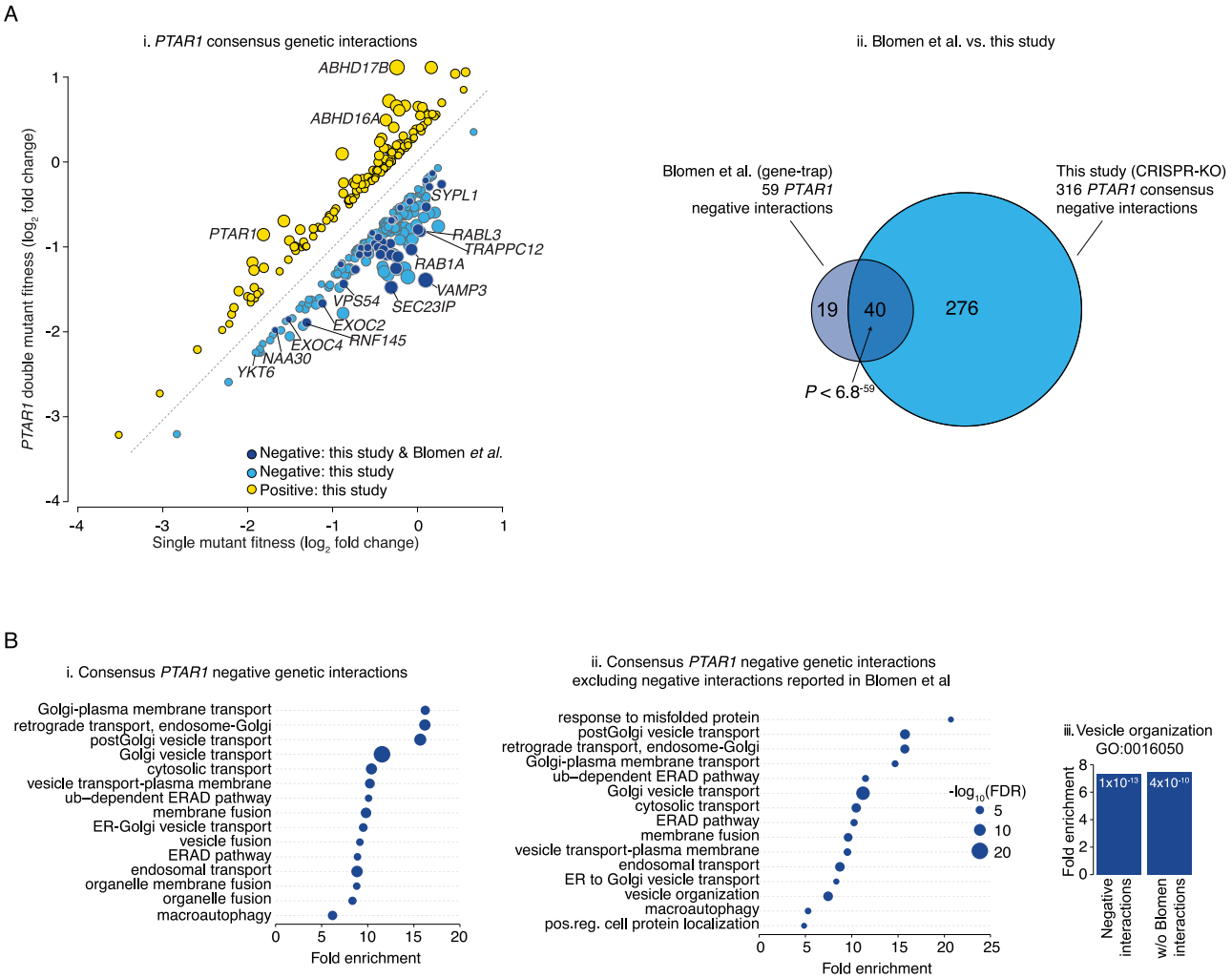

Figure S6. *PTAR1* genetic interactions identified in HAP1 cells using a CRISPR-KO versus a gene retroviral trap approach, related to STAR Methods

(A) (i) Scatterplot of mean consensus qGI scores derived from 4 independent *PTAR1* query screens (GIN003, GIN043, GIN044, and GIN109) with TKOv3. Negative (blue) and positive (yellow) genetic interactions satisfying a standard confidence threshold (|qGI| > 0.3 and FDR < 0.1) are shown. Selected negative (blue) and positive (yellow) interactions are indicated. *PTAR1* negative interactions identified by the gene-trap method[6] are shown in dark blue. (ii) Venn diagram illustrating the overlap between *PTAR1* negative interactions identified in this study and the gene trap analysis (Blomen et al.).[6]

(B) (i) Functional enrichment (hypergeometric test, Benjamini-Hochberg-corrected FDR < 0.2) of genes that showed a negative interaction with *PTAR1* in this study or (ii) genes that showed a negative interaction with *PTAR1* after excluding genes that also showed a negative interaction with *PTAR1* in the Blomen et al. gene trap study.[6] (iii) Bar chart indicating fold-enrichment for each of the indicated gene sets, specifically for the indicated vesicle organization GO term.

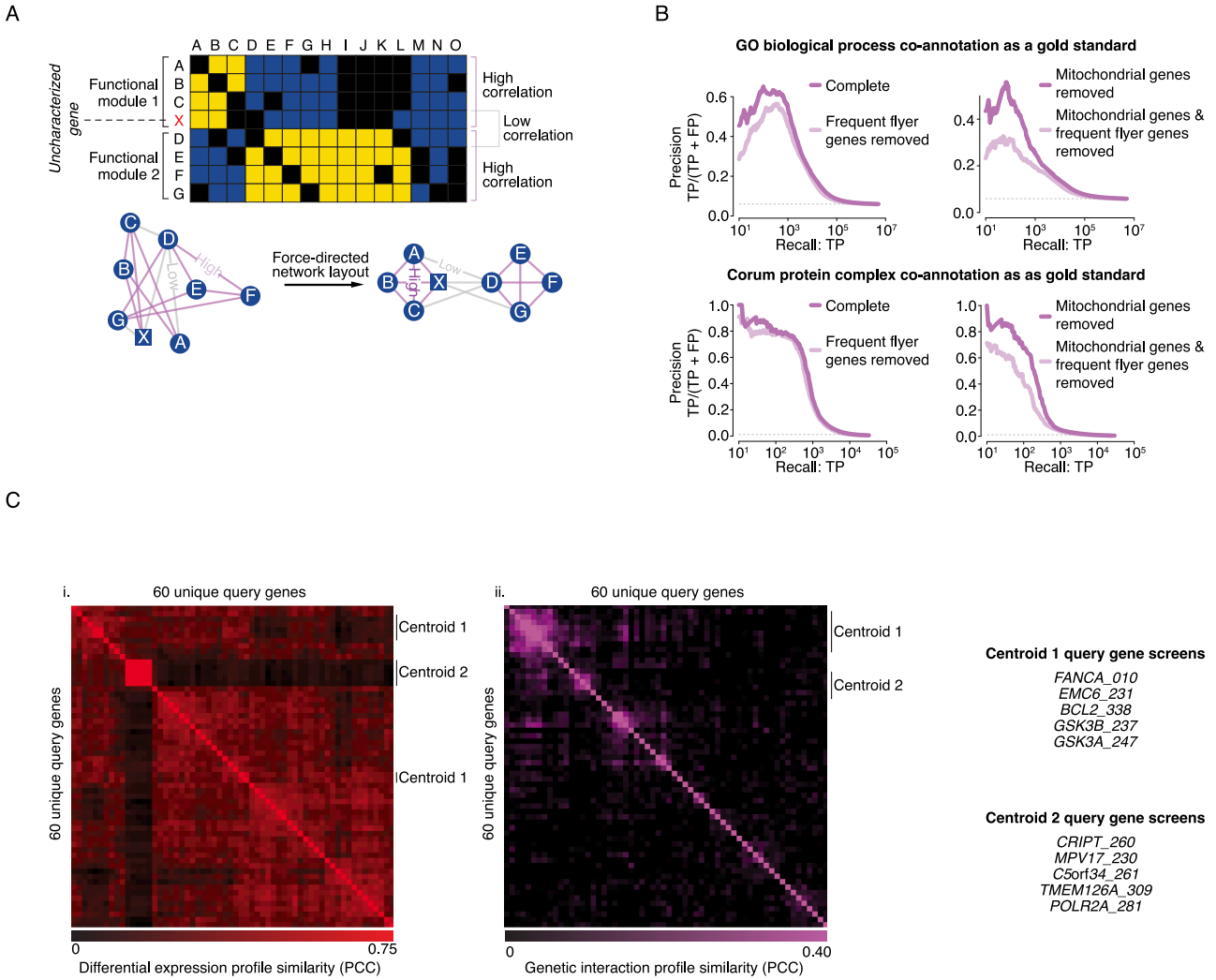

Figure S7. Functional evaluation of genetic interaction profiles, related to Figure 1

(A) Schematic illustrating genetic interaction profile similarity. The set of negative (blue) and positive (yellow) interactions for a given mutant is referred to as a genetic interaction profile. Two-dimensional hierarchical clustering groups genes together based on genetic interaction profile similarity, enabling identification of highly correlated groups of genes that correspond to functionally related gene modules. Genetic interactions can also be visualized as a correlation-based network connecting genes with similar genetic interaction profiles. Using a force-directed network layout, genes with highly similar genetic interaction profiles (purple lines) are placed close to each other in the network while genes with less similar interaction profiles (gray lines) are placed further apart from one another.[65]

(B) Genes with varying degrees of genetic interaction profile similarity were evaluated for overlap with either GO biological process co-annotations or CORUM protein complex co-annotations using precision-recall analysis. Gene pairs were sorted based on Pearson correlation coefficients, reflecting similarity in their genetic interaction profiles. Gray dashed lines show the background rate of co-annotation for the relevant set of gene pairs. Precision-recall analysis was completed separately for genetic interaction profiles derived from all library genes in the dataset as well as genetic interaction profiles excluding genes associated with highly variable single mutant fitness and/or mitochondrial genes, as indicated.

(C) (i) Matrix of 60 unique query gene mutant cell lines clustered based on pair-wise similarity of their differential gene expression profiles (red) or (ii) of their genetic interactions (purple). Two groups of genes that cluster together in both matrices and whose genetic interaction profiles were used to correct the complete genetic interaction matrix to construct a genetic interaction profile similarity network are indicated as centroid 1 and centroid 2 and described in detail in the STAR Methods section. The query gene mutant cell lines that comprise centroid 1 and centroid 2 are listed.

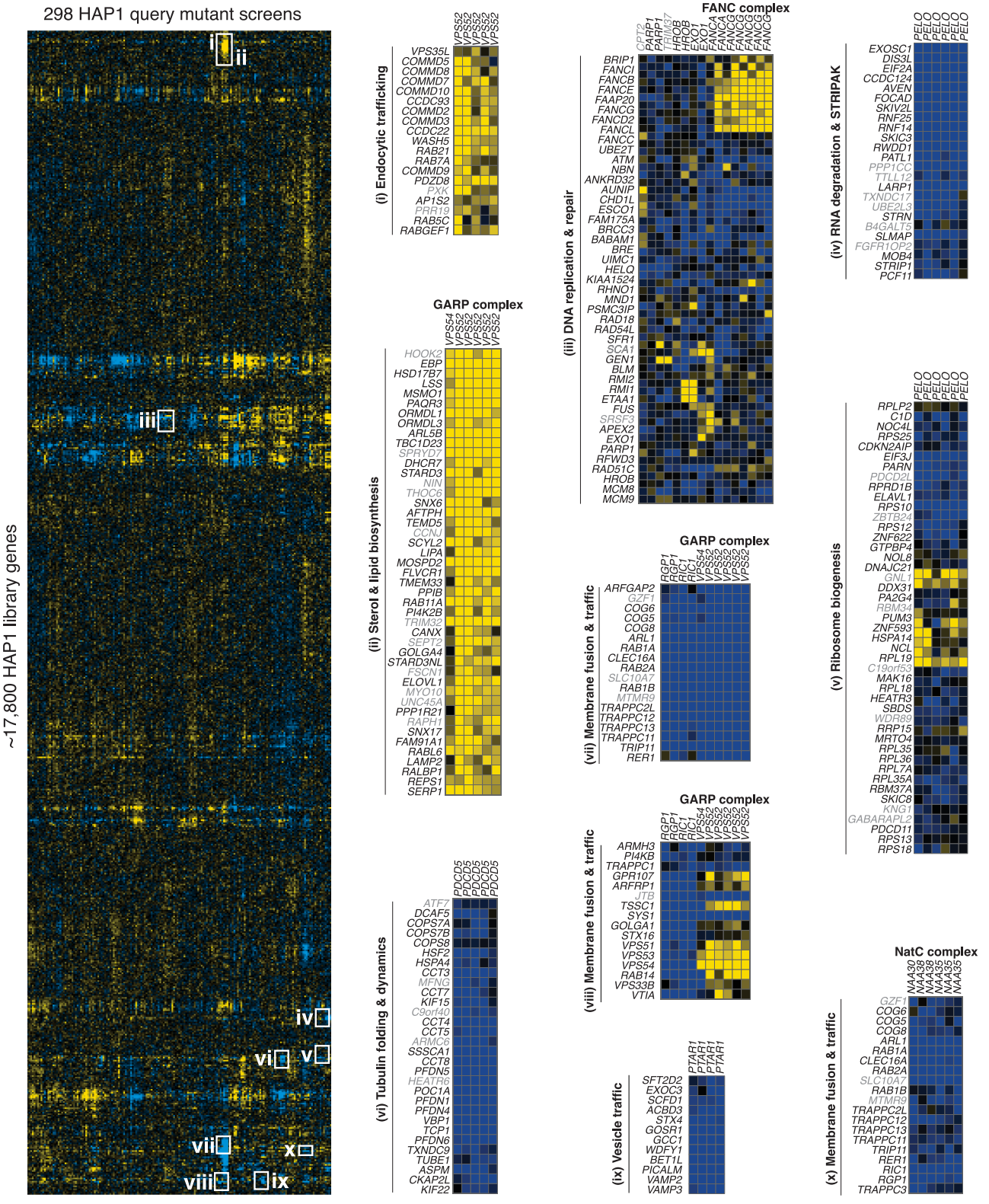

(legend on next page)

Figure S8. Two-dimensional hierarchical clustering of the HAP1 genetic interaction dataset, related to Figure 1

Negative (blue) and positive (yellow) genetic interactions are shown. Rows in the matrix correspond to 17,297 genes targeted by the TKOv3 library. Columns in the matrix represent 298 genome-scale genetic interaction screens corresponding to 222 unique query mutant cell lines. Sections (white outlines) are expanded to allow visualization of specific query-library gene-gene interactions.

A

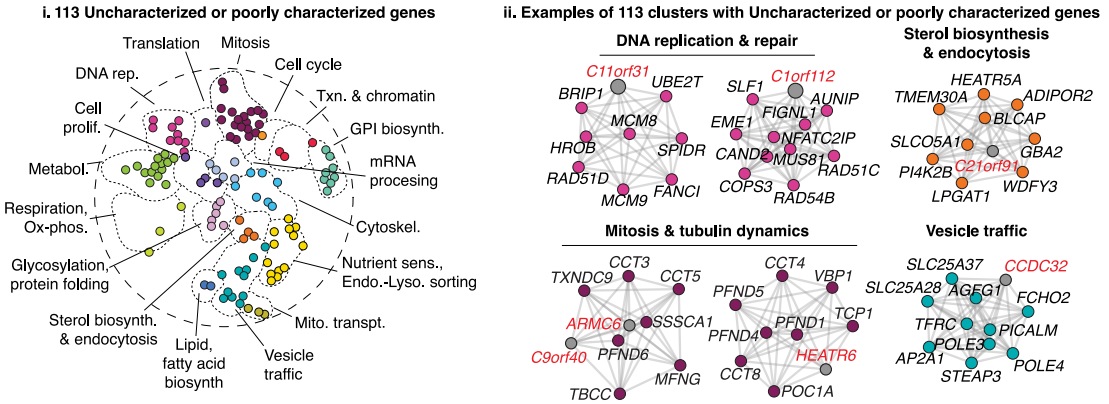

B

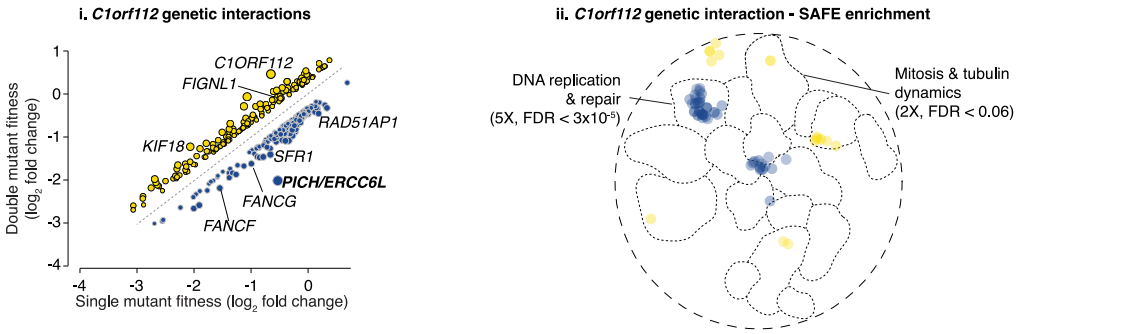

C

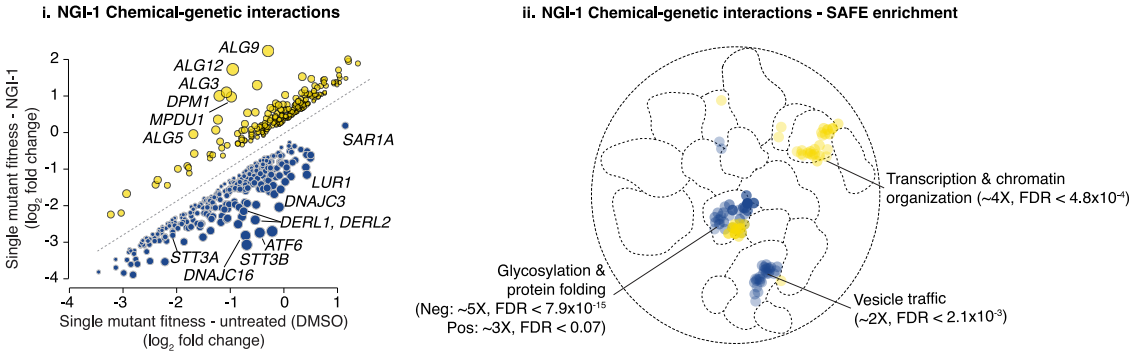

D

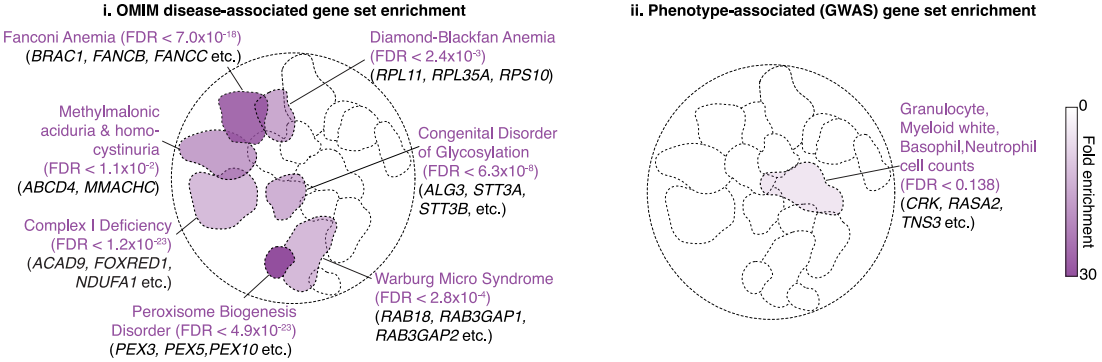

(legend on next page)

Figure S9. Annotating gene function using the HAP1 genetic interaction network, related to Figure 1

(A) (i) Poorly characterized genes (i.e., GO bioprocess terms + PubMed citations < 15) that localize to a specific bioprocess-enriched cluster on the genetic interaction profile similarity network shown in Figures 1A and 1B. Nodes are colored according to bioprocesses shown in Figure 1B. (ii) Selected examples of re-clustered gene modules from the complete HAP1 genetic interaction matrix, where genes with the same node color have a shared function and poorly characterized genes are indicated with gray nodes and red labels.

(B) (i) Scatterplot of qGI scores for a HAP1 *C1orf112/FIRRMM* mutant query screen. The *C1orf112/FIRRMM* profile suggested a role for this gene in DNA damage and repair, a prediction supported by recent studies.[47,174] Negative (blue) and positive (yellow) genetic interactions that satisfied a standard confidence threshold (|qGI| > 0.3 and FDR < 0.1) are shown, and specific negative and positive interactions are labeled, including the strongest negative interaction that confirmed a previously identified *PICH/ERCC6L-C1orf112/FIRRMM* interaction (bold font).[47] (ii) Regions of the HAP1 genetic interaction network that are significantly enriched (hypergeometric test, Benjamini-Hochberg-corrected, FDR < 0.001) for genes exhibiting negative (blue) or positive (yellow) genetic interactions with a *C1orf112/FIRRMM* query mutant cell line. Enrichment was calculated using SAFE as described in STAR Methods.

(C) The HAP1 profile similarity network provides insights into the mode-of-action of bioactive molecules.[4,67,175] (i) Scatterplot of chemical-genetic interactions identified in the presence of 15uM NGI-1, a small molecule inhibitor of the oligosaccharyltransferase (OST) complex.[176] Genes that showed sensitivity (i.e., negative chemical-genetic interactions, blue) or resistance (i.e., positive chemical-genetic interactions, yellow) to NGI-1 were enriched for roles in protein glycosylation and vesicle trafficking and localized to the corresponding functional domain region of the genetic profile similarity network. Genes that exhibited negative and positive chemical-genetic interactions with NGI-1 are indicated. (ii) Regions of the HAP1 profile similarity network that are significantly enriched for genes exhibiting negative (blue) or positive (yellow) chemical-genetic interactions with NGI-1. Enrichments for NGI-1 negative or positive chemical-genetic interactions within functional domains in the HAP1 genetic profile similarity network were determined using a hypergeometric test for over-enrichment conducted for each domain, followed by a Benjamini-Hochberg correction. Fold enrichment and significance of negative and positive chemical-genetic interaction enrichment are indicated.

(D) The HAP1 genetic profile network highlights functions shared among different subsets of genes associated with the same disease trait or phenotype. Regions of the HAP1 genetic interaction network that are significantly enriched for (i) genes associated with a Mendelian-inherited disease (OMIM disease) or (ii) genes associated with traits identified by GWAS. For each disease or trait gene set, a hypergeometric test for enrichment was conducted against the 17 bioprocess domains defined in the HAP1 profile similarity network, followed by a Benjamini-Hochberg correction.

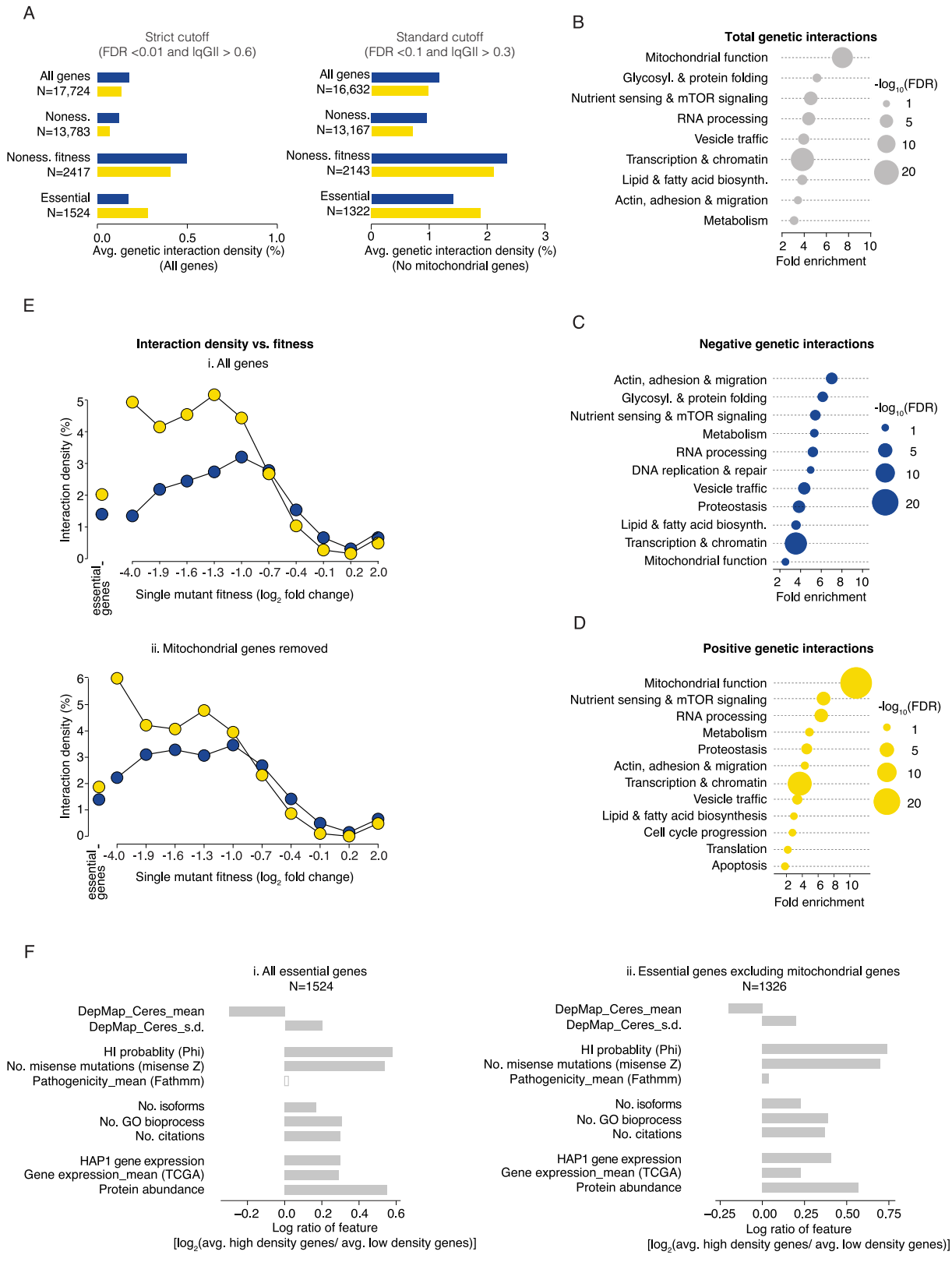

(legend on next page)

Figure S10. Genetic interaction density analysis, related to Figure 2

(A) Bar charts showing genetic interaction density (observed interactions/total gene pairs screened) for all library genes by category (all genes, nonessential genes [noness], nonessential genes with fitness phenotypes [noness. fitness], and essential genes) at strict genetic interaction score and significance threshold (FDR < 0.01, |qGI| > 0.6) and for library genes excluding those with roles in mitochondrial function at the standard score and significance threshold (FDR < 0.1, |qGI| > 0.3). Negative (blue), positive (yellow), and total (gray) interaction densities, with the number of genes in each category, are indicated.

(B–D) Dot plots showing functional enrichment of genetic interaction hubs. Reactome pathway terms[172] statistically enriched (hypergeometric test, Benjamini-Hochberg-corrected FDR < 0.2) among highly connected genes representing total (gray), negative (blue), and positive (yellow) genetic interaction hub genes were summarized according to the functional descriptions shown.

(E) Line plots showing the average density of negative (blue) and positive (yellow) genetic interactions for (i) all library genes and (ii) excluding genes with roles in mitochondrial function relative to library gene single mutant fitness. The average negative and positive interaction density for essential genes (ess.) is also shown on the left.

(F) A subset of essential genes participated in genetic interactions in HAP1 cells. Sequence, functional, and evolutionary properties that are significantly associated with essential library genes that exhibited high genetic interaction density relative to essential genes with few genetic interactions. The analysis was performed using (i) all genes or (ii) excluding mitochondrial genes. High interaction density was defined as the top 20% of HAP1 essential genes with the highest total genetic interaction density, whereas low interaction density consisted of the 50% of HAP1 essential genes with the lowest genetic interaction density. For each feature, the mean of the high-density group and the low-density group were computed, and the $\log_2$ ratio of these means is plotted. Open bars indicate relationships for which the 95% confidence interval on the correlation coefficient includes 0.

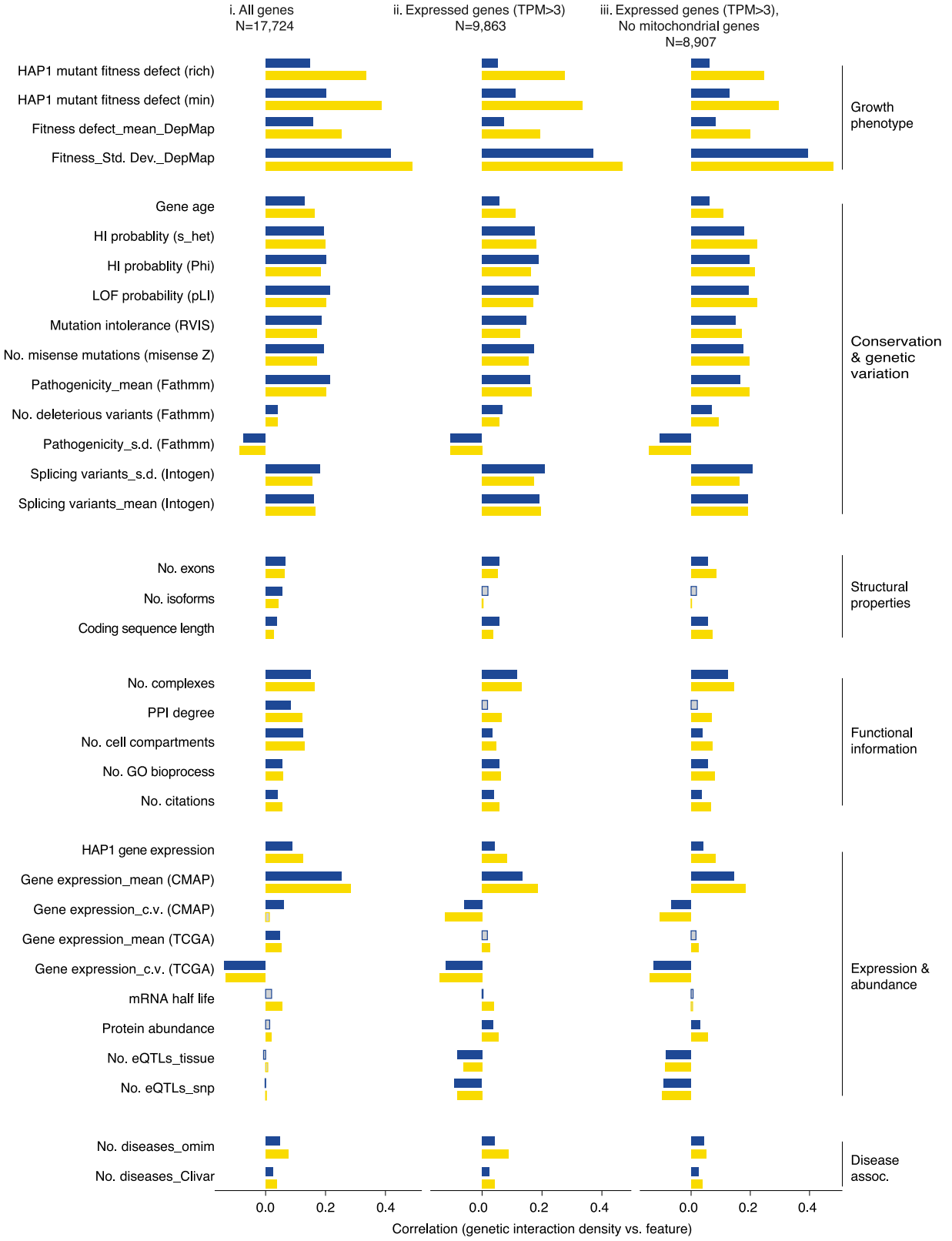

(legend on next page)

Figure S11. Correlation analysis of genetic interaction density, related to Figure 2

Negative (blue) and positive (yellow) genetic interaction density was calculated for (i) all genes targeted by the TKOv3 CRISPR library, (ii) genes expressed in HAP1 cells, and (iii) genes expressed in HAP1 cells without mitochondrial genes. The standard confidence threshold ($|qGI| \geq 0.3$, FDR < 0.1) was applied, and interaction density was computed as the percentage of observed interactions. Pearson's correlation coefficient was used to measure associations between genetic interaction density and features that are continuous or count based. Significant ($p < 0.05$, using the cor.test function in R and Pearson's correlation) non-zero correlation relationships with negative (blue) and positive (yellow) interaction densities are plotted. Open bars indicate relationships for which the 95% confidence interval on the correlation coefficient includes 0. Given that analysis of different features required different statistical tests and some features are not expected to be independent of each other, multiple hypotheses correction procedures were not applied (see STAR Methods and Data S14 for details). HI, haploinsufficiency; LOF, loss of function.

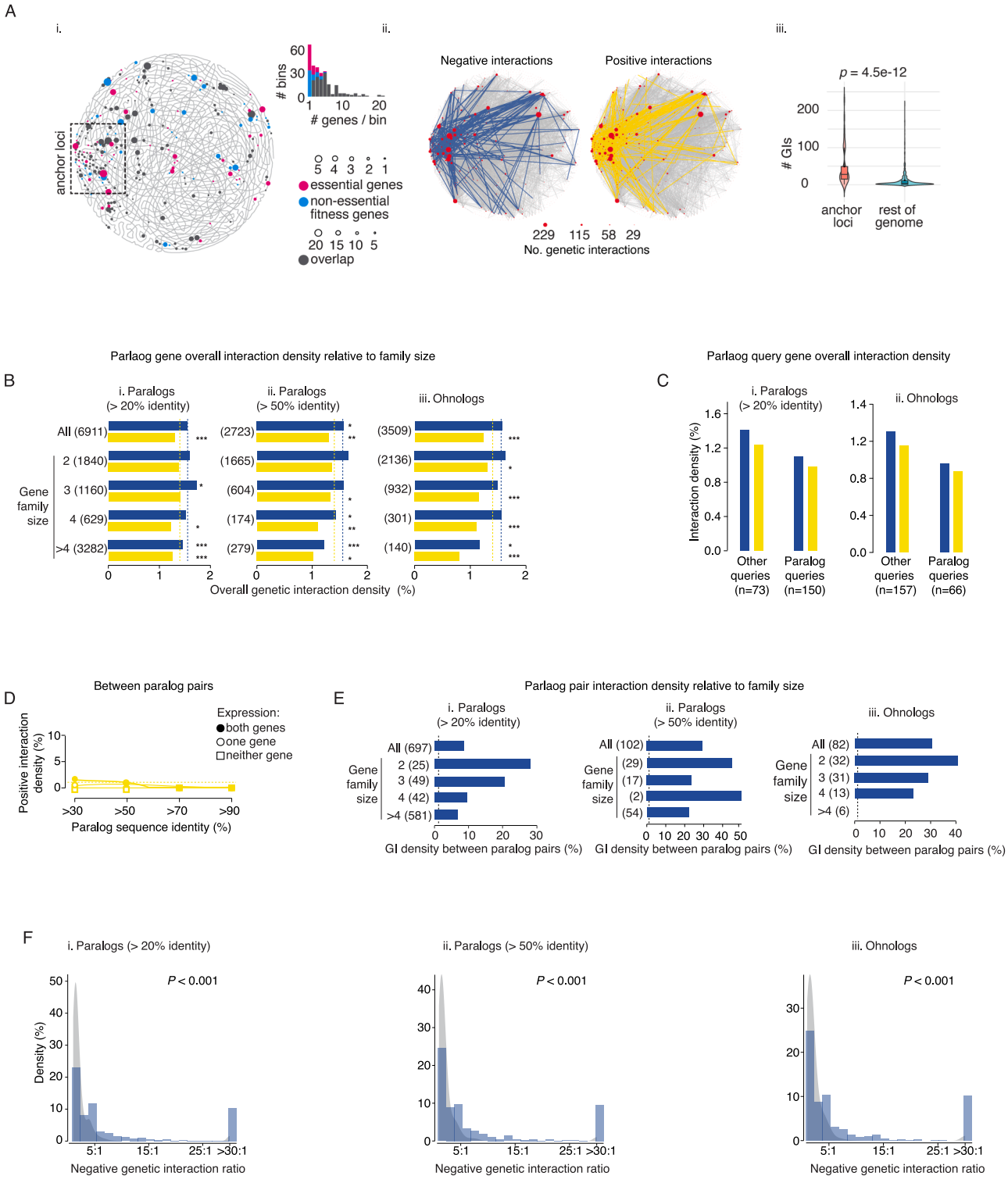

Figure S12. Genetic interaction density associated with genome topology and duplicated genes, related to Figure 2

(A) (i) Genome topology map generated based on *cis*- and trans-chromosomal contacts from 62 near diploid Hi-C datasets.[70] Nodes are colored to represent enrichment for essential genes (magenta), nonessential genes with fitness defects (cyan), and those labeled "overlap," which contain a mixture of essential and nonessential genes with a fitness defect (gray). Node size represents the number of fitness genes overlapping with trans-contacts. Node sizes are indicated by the 2 different scales. (ii) Negative (left) and positive (right) genetic interactions mapped onto the network described in (i). Nodes represent the number of genetic

(legend continued on next page)

interactions in a particular 1 Mb bin. (iii) Violin plots indicating the number of genetic interactions in the anchor loci compared with the rest of the genome (Mann-Whitney U test, $p < 4.5 \times 10^{-12}$).

(B) Bar plots depicting the average negative (blue) and positive (yellow) genetic interaction densities for individual paralog library genes with all tested query genes relative to gene family size for paralogs sharing (i) >20% or (ii) >50% sequence identity, as well as (iii) ohnologs. The numbers of interactions involving a paralog gene tested in each family size bin are indicated (* indicates level of statistical significance, $*p < 0.05$, $**p < 0.01$, $***p < 0.001$, Wilcoxon rank-sum).

(C) Bar plots indicating the average negative (blue) and positive (yellow) genetic interaction densities for individual paralog query genes versus non-duplicated query genes surveyed in this study. Query gene paralogs were defined as genes that share (i) at least 20% sequence identity, as well as (ii) ohnologs.

(D) Positive genetic interaction density among pairs of duplicated genes with increasing sequence identity (i.e., paralogs). Genetic interaction density was measured separately for paralog pairs that are both expressed in HAP1 cells, pairs where one gene/pair is expressed, and pairs that are not expressed in HAP1 cells.

(E) Bar plots depicting paralog pair genetic interaction density ($|qGI| > 0.3$, FDR < 0.1) relative to family size for paralogs sharing (i) >20% or (ii) >50% sequence identity, as well as (iii) ohnologs.[157] Interaction density was expressed as a percentage of all tested paralog gene pairs. The numbers of paralog pairs tested in each family size bin are indicated in brackets.

(F) Histograms of negative interaction degree ratio as evidence for asymmetric functional divergence for paralog gene pairs sharing (i) >20% or (ii) >50% sequence identity and (iii) ohnologs. The ratio is defined as the number of unique negative interactions (degree) identified for each gene of a duplicate pair with the higher degree in the numerator. Shown for comparison is another degree ratio histogram (symmetric null model) in which interactions for every duplicate pair are redistributed to either member with equal probability (gray).

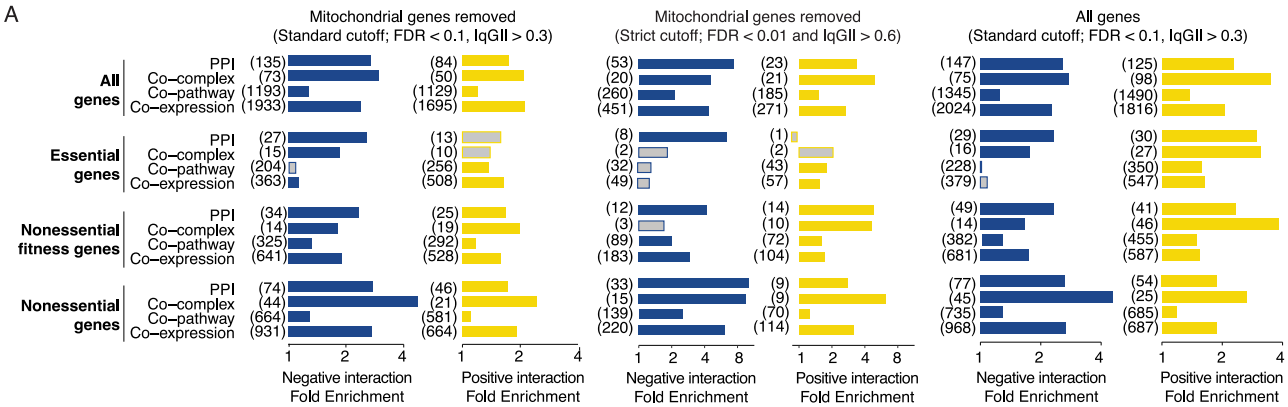

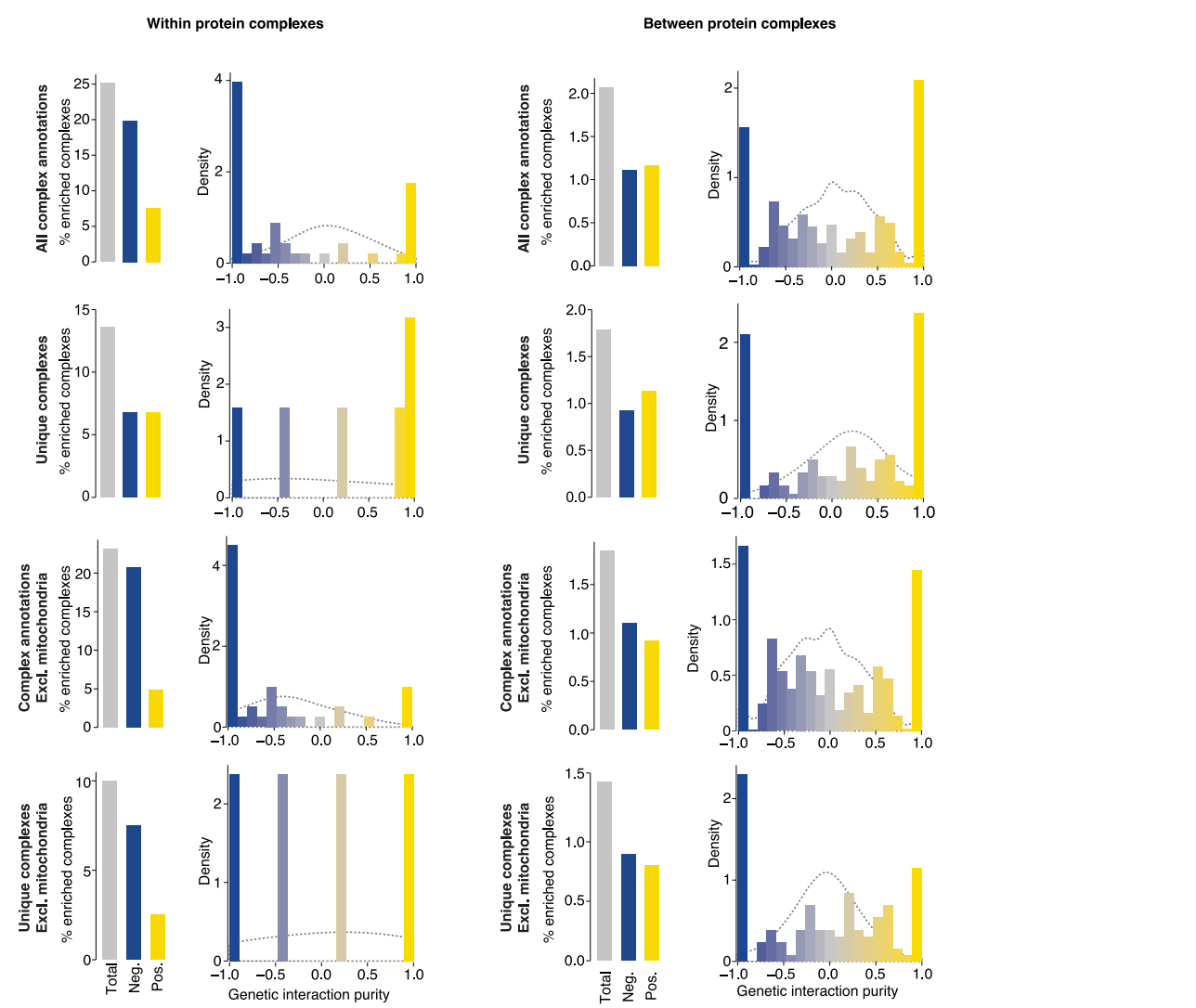

(legend on next page)

Figure S13. Relating genetic and physical interactions, related to Figure 2

(A) Bar charts show significant fold-enrichment ($p < 0.05$, hypergeometric test) for either all gene pairs or gene pairs excluding mitochondrial genes encoding physically interacting proteins (PPI), co-complex proteins, co-pathway proteins, or co-expressed gene pairs among negative (blue) and positive (yellow) genetic interactions defined at the indicated standard or strict confidence threshold. Enrichment was measured for all gene pairs, essential gene pairs, nonessential genes with fitness phenotypes, and nonessential genes lacking a fitness phenotype. Gray bars indicate non-significant enrichment. The numbers of gene pairs tested for enrichment are indicated in brackets.

(B) (Left) Bar graphs summarize complexes enriched for genetic interactions among members of the same complex (within-protein complex) or enrichment of genetic interactions between pairs of protein complexes (between-protein complex) as the percentage of protein complexes (CORUM database) with enriched genetic interactions, categorized as all interactions (gray), negative (blue), or positive (yellow) within/between protein complexes. (Right) Histograms illustrate purity scores indicating the proportion of negative and positive interactions within a protein complex or between a pair of protein complexes. Purity scores range from −1 (purely negative interactions) to 1 (purely positive interactions) among complex members. The dotted gray line indicates the random expectation based on a binomial distribution. Analyses include all CORUM annotated complexes or a subset of complex annotations where redundant complexes with overlapping genes were removed. In both cases, analyses were based on complexes and complex pairs with >5 tested gene pairs. Analyses were repeated after excluding genes with mitochondrial-related functions.

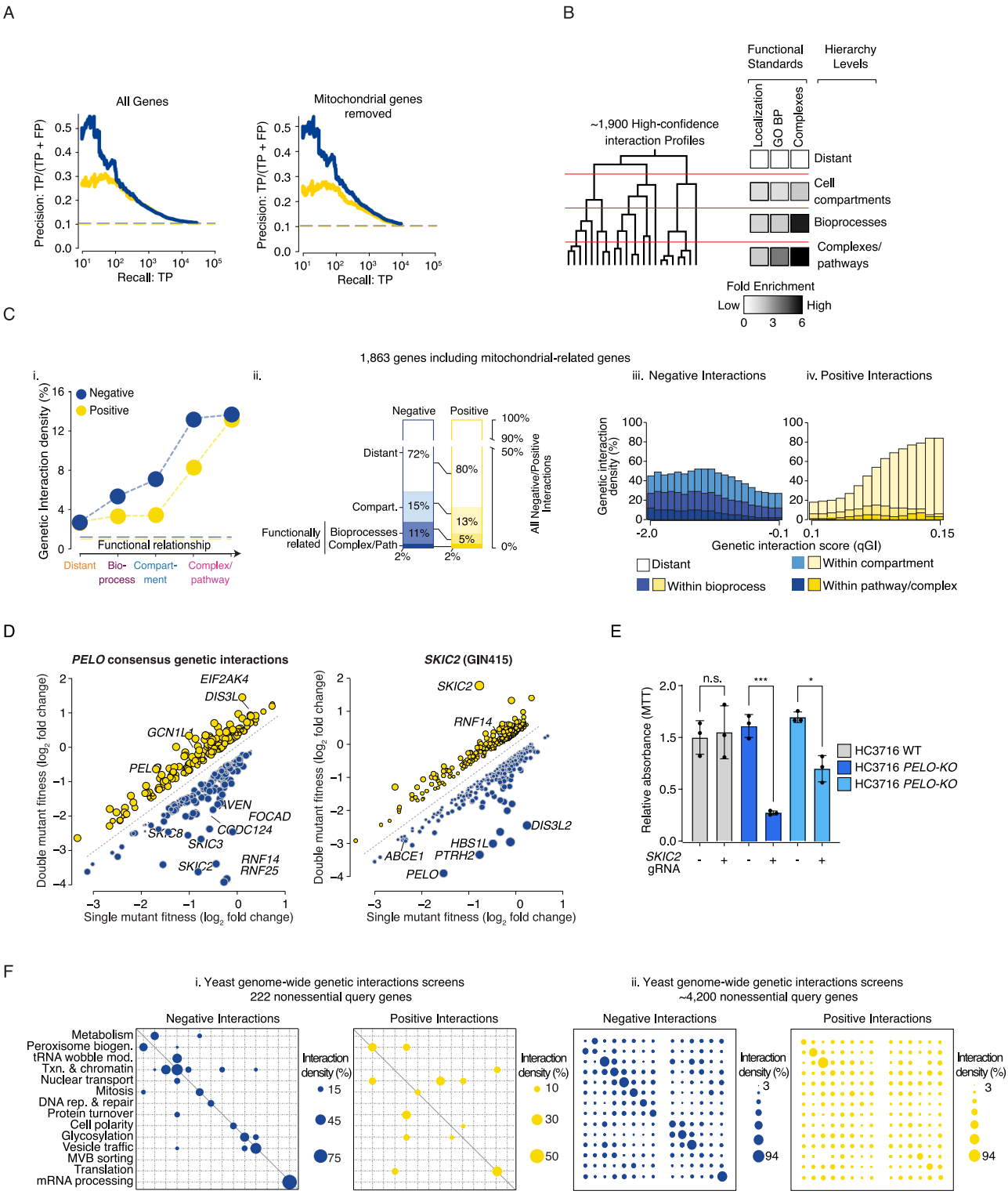

Figure S14. Functional distribution of genetic interactions, related to Figure 3

(A) Precision-recall plots for negative (blue) and positive (yellow) genetic interactions (|qGI| > 0.3, FDR < 0.1) based on co-annotation to GO biological process terms, including and excluding genes with mitochondrial-related functions. Dashed lines indicate background co-annotation rates.

(B) Genetic interaction profile-derived hierarchy schematic. Genes with highly correlated genetic interaction profiles form small, densely connected clusters representing specific pathways or protein complexes. Intermediate correlation combines sibling clusters into larger biological process-enriched clusters, which

(legend continued on next page)

further combine into larger clusters corresponding to cell compartments. Gray scale bar indicates sibling cluster enrichment for functional terms. Analysis includes ~1,600 genes with high-confidence profiles, excluding genes with mitochondrial-related functions.

(C) (i) Line graph depicts the density of negative (blue) and positive (yellow) genetic interactions (|qGI| > 0.3, FDR < 0.1) within a specific level of the genetic network hierarchy. Horizontal dashed lines represent background interaction density. (ii) Stacked bar chart shows the functional distribution of all negative (blue) and all positive (yellow) interactions (|qGI| > 0.3, FDR < 0.1) among genes in the genetic network hierarchy, depicting percentages within clusters corresponding to cellular compartments, bioprocesses, or complexes/pathways. The combined fraction of functionally related interactions is indicated (*). (iii–iv) Bar graphs show the fraction of negative (iii, blue) or positive (iv, yellow) interactions connecting genes within the same cluster at varying functional relatedness levels. This analysis includes genes with mitochondrial-related functions.

(D) Scatterplot of mean consensus qGI scores derived from 4 independent *PELO* query screens (GIN289, GIN291, GIN292, and GIN295; Data S4) or a *SKIC2* query screen (GIN415; Data S24) with TKOv3. Negative (blue) and positive (yellow) genetic interactions satisfying a standard confidence threshold (|qGI| > 0.3 and FDR < 0.1) are shown. Selected negative (blue) and positive (yellow) interactions are indicated.

(E) MTT cell proliferation assay of Hc3716 liver cells with or without *PELO* following perturbation of *SKIC2*. Results using two independent *PELO* KO mutant clones are shown (***$p < 0.01$, *$p < 0.05$ using one-way ANOVA followed by Tukey's post hoc test). Error bars reflect standard deviation in the measurements.

(F) (i) Dot plots depicting yeast network density of negative (blue) and positive (yellow) nonessential gene interactions (|SGA score| > 0.08, $p < 0.05$) within and across biological processes for 222 randomly sampled yeast query mutants. Node size reflects the fraction of interacting gene pairs observed for a given pair of biological processes, and node color indicates significance above random expectation. (ii) Dot plot shows a similar analysis based on the complete set of ~4,200 yeast nonessential gene query mutant strains. Nodes on the diagonal represent interactions within the same biological process, and off-diagonal nodes represent interactions between processes.

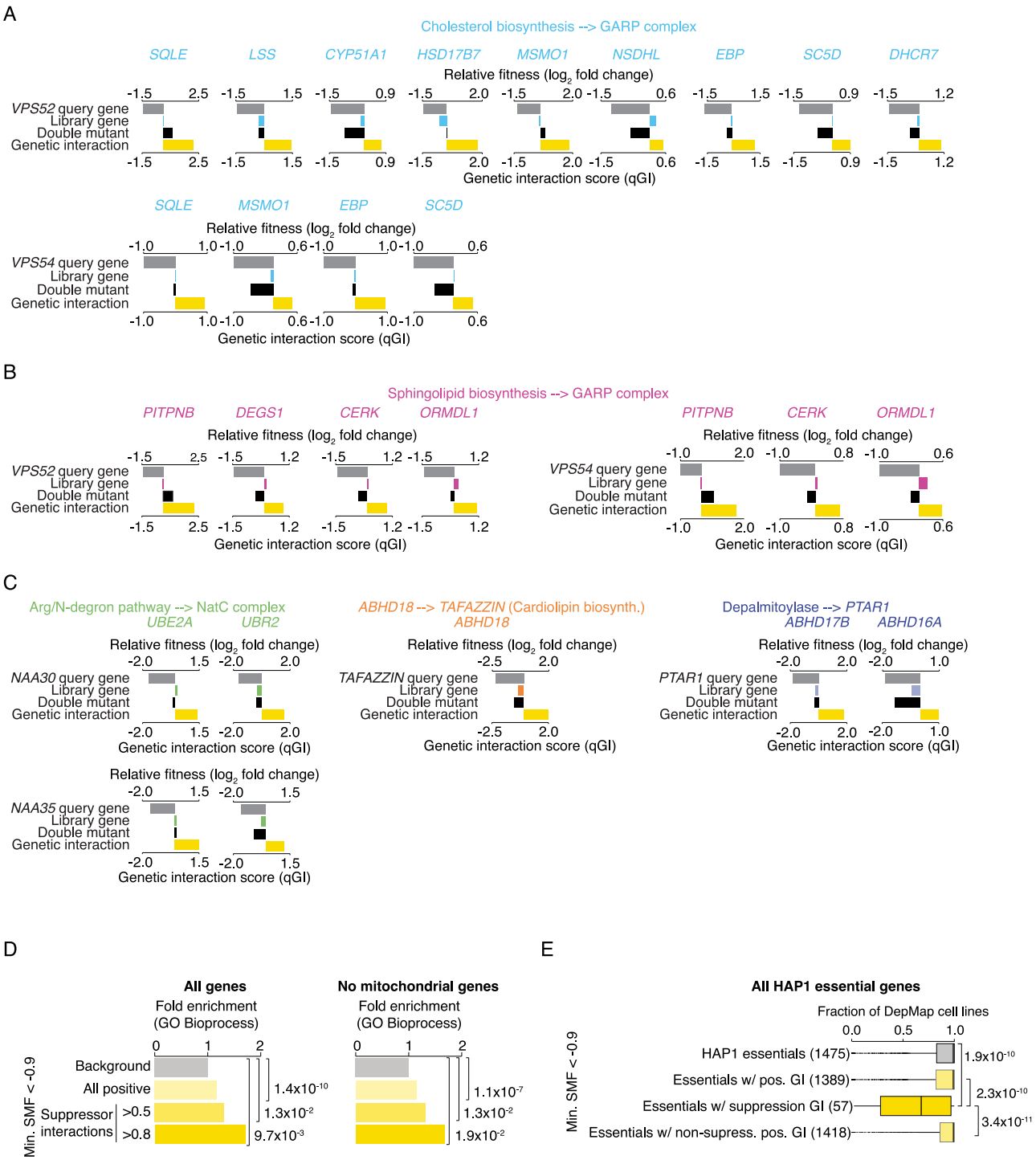

Figure S15. Genetic suppression interactions, related to Figure 4

(A–C) Bar graphs illustrating quantitative analysis of specific genetic suppression interactions. Query gene single mutant fitness (gray bars), library gene single mutant fitness (gene-specific colored bars), double-mutant fitness (black bars), and positive genetic interaction score (qGI, yellow bars) are shown.

(D) Bar graph showing the fold enrichment of GO biological process co-annotation among gene pairs that showed positive interactions and/or suppression interactions defined at two different suppression score thresholds as described in STAR Methods. Significance of enrichment relative to background was assessed using a Fisher's exact test. Analysis with and without mitochondrial genes is shown.

(E) Boxplot showing the average fraction of DepMap cell lines that depend on the indicated groups of HAP1 essential genes for viability. Numbers of essential genes tested in each group are indicated. Significant differences are indicated (*p* value, Wilcoxon rank-sum test). Analysis is based on all essential genes, including essential genes with mitochondrial-related functions.

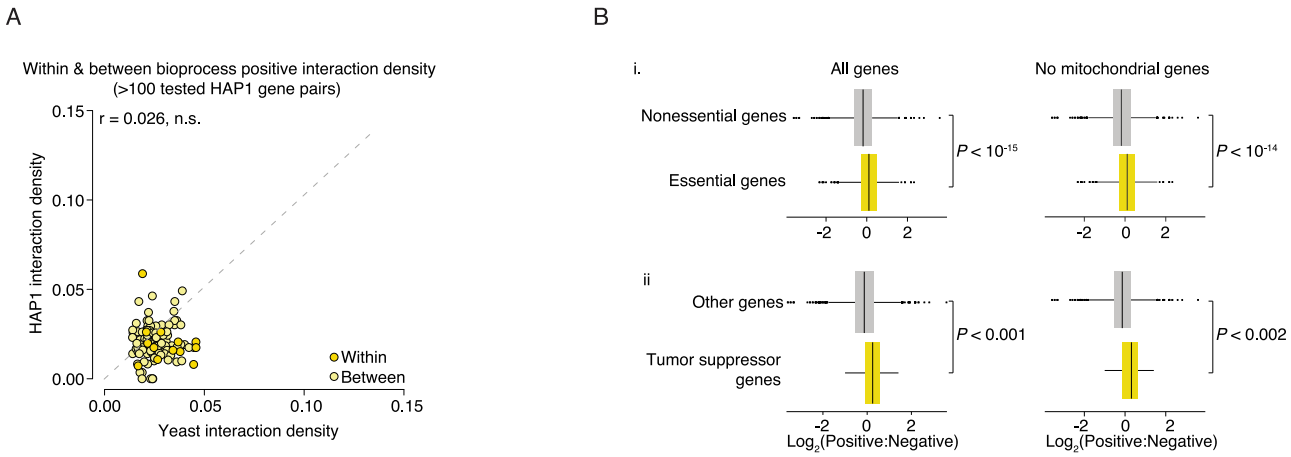

Figure S16. HAP1 positive genetic interactions, related to Figure 5

(A) Scatterplot of human (qGI > 0.3, FDR < 0.1) and yeast (SGA score > 0.08, $p < 0.05$) positive genetic interaction densities that occur within and between corresponding bioprocesses.

(B) (i) Boxplots illustrating the distribution of the ratio of positive to negative genetic interactions for all nonessential and all essential library genes with (all genes) or without (no mitochondrial genes) mitochondrial genes. (ii) Boxplots illustrating the distribution of the ratio of positive to negative genetic interactions for tumor suppressor genes and all other genes with (all genes) or without (no mitochondrial genes) mitochondrial genes. Significant differences (p value, Wilcoxon rank-sum test) are indicated.

See Data S19 for gene lists.

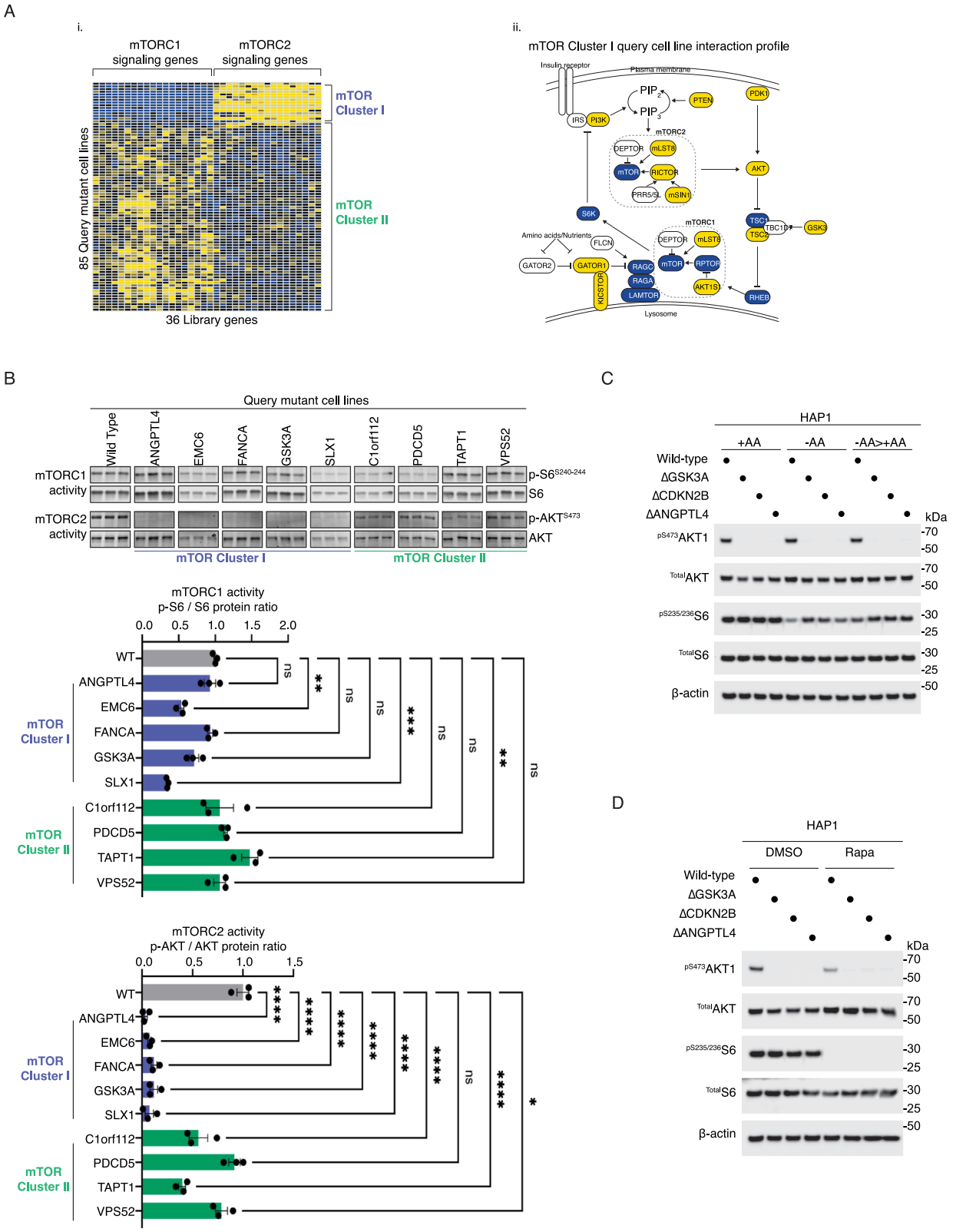

(legend on next page)

Figure S17. Query-driven mTOR signaling effects, related to Figure 5 and Document S1

(A) (i) Heatmap depicting hierarchically clustered genetic interaction matrix comprising 85 different query gene mutant cell lines that show coherent negative (blue) and positive (yellow) genetic interactions with library genes involved in mTORC1 and mTORC2 signaling. This analysis identified two inverse patterns of genetic interactions involving library genes with roles in mTORC1 and mTORC2 signaling. The first pattern, mTOR cluster I, comprised 17 query mutant cell lines that showed strong negative interactions with mTORC1 signaling genes and many strong positive interactions with mTORC2 signaling genes. (ii) Schematic of mTORC1 and mTORC2 signaling pathways. Library genes are colored based on their genetic interactions with query genes belonging to the mTOR cluster I.

(B) Immunoblots and related quantitation showing phospho-AKT1^{S473} and phospho-AKT$^{S240/244}$ effects under baseline growth conditions in the indicated HAP1 queries representative of mTOR cluster 1 or mTOR cluster II signatures. The 3 blots per query represent independent replicates derived from the same cell line but seeded in different wells and treated, lysed, and assayed independently. Blue bars indicate mTOR cluster I, and green bars indicate mTOR cluster II. Error bars reflect standard deviation of replicate measurements. *Indicates level of statistical significance (One-way ANOVA, Dunnett's multiple testing correction; $^{*}p < 0.05$, $^{**}p < 0.01$, $^{***}p < 0.001$, $^{****}p < 0.0001$).

(C and D) Immunoblots depicting phospho-AKT1^{S473} and phospho-AKT$^{S6235/236}$ effects following amino acid starvation and starvation>stimulation (C) and rapamycin treatment (D) in the indicated HAP1 queries representative of mTOR cluster II signatures.

See Document S1.

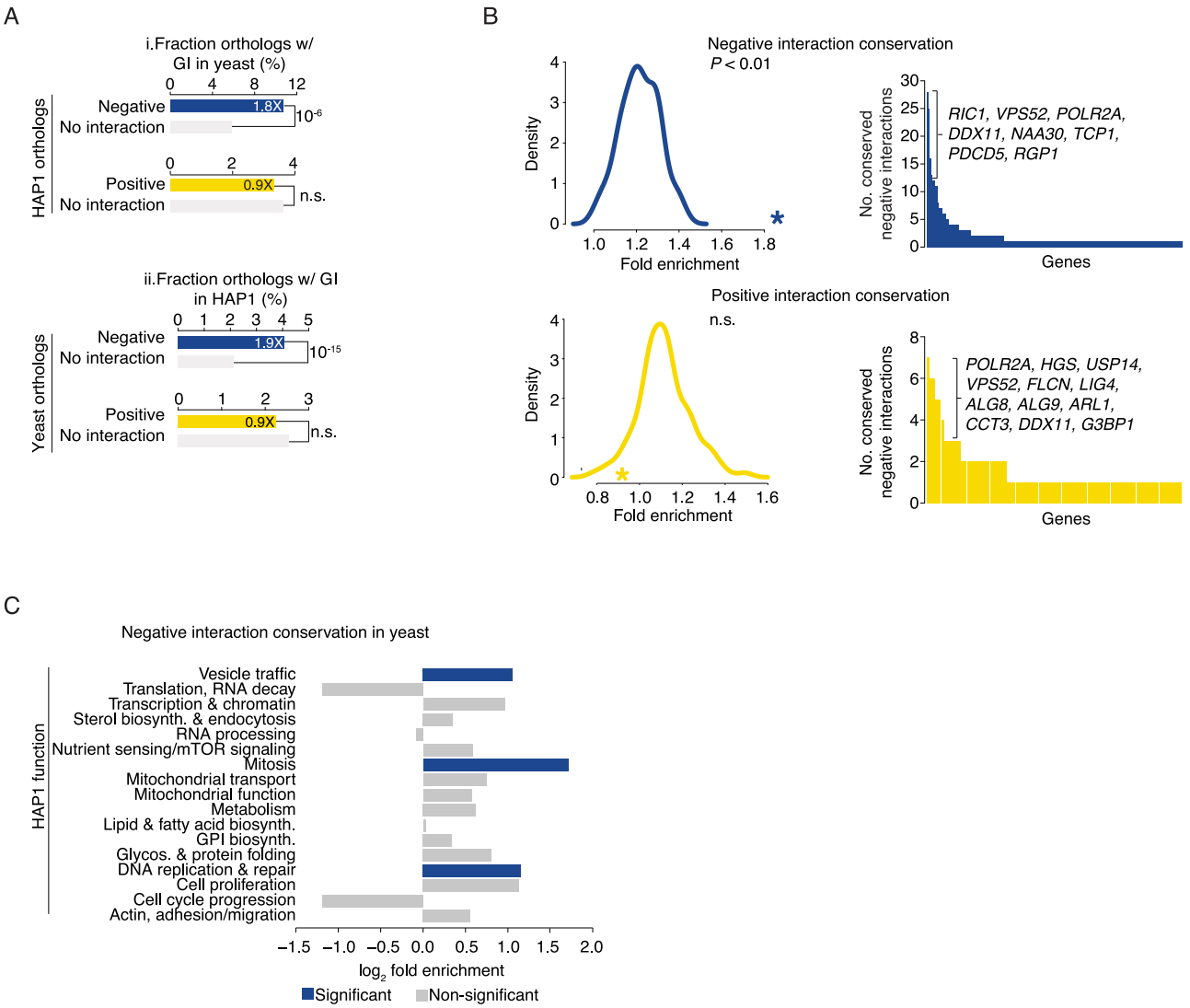

Figure S18. Genetic interaction conservation, related to Figure 5

(A) (i) Bar graph showing enrichment for negative (blue) and positive (yellow) genetic interactions in yeast among conserved gene pairs scored as negative or positive interactions in HAP1 cells. Negative interactions in HAP1 were significantly enriched in yeast compared with other conserved gene pairs without negative interactions. Positive interactions in HAP1 were not significantly enriched in yeast. (ii) Bar graph showing enrichment for negative (blue) and positive (yellow) interactions in HAP1 cells among conserved gene pairs with negative or positive genetic interaction in yeast. Negative interactions in yeast were significantly enriched in HAP1 compared with other conserved gene pairs. Positive interactions in yeast were not significantly enriched in HAP1. In all cases, significance of enrichment was assessed using Fisher's exact test.

(B) Density plots showing the fold enrichment in the conservation of negative (top) and positive (bottom) genetic interactions in *S. cerevisiae* for 100 randomized HAP1 genetic interaction networks. The observed fold enrichment of the real HAP1 genetic interaction network is represented by a star. Bar graphs show the number of negative (top) and positive (bottom) genetic interactions identified in both *S. cerevisiae* and HAP1 cells per human gene. Query genes that contribute many conserved negative and positive interactions are indicated.

(C) Bar graph illustrating biological processes enriched for conserved negative genetic interactions among human-yeast orthologous gene pairs identified in HAP1 genetic interaction screens. Blue bars indicate significant enrichment.

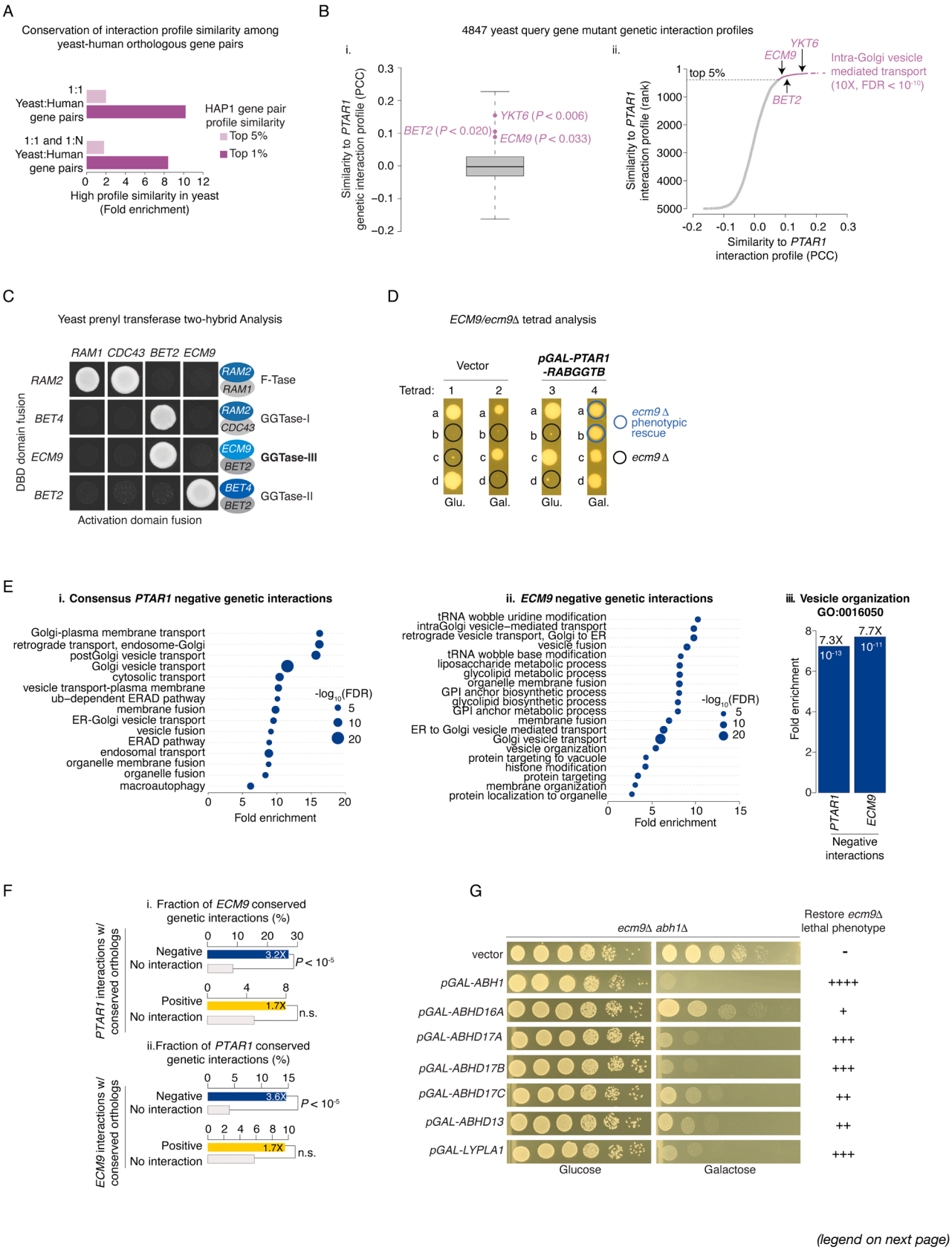

(legend on next page)

Figure S19. Conservation of *PTAR1*/*ECM9* genetic interactions, related to Figure 5

(A) Bar graph illustrating that human gene pairs with conserved yeast orthologs (1:1 and 1 yeast: N human ortholog pairs) that share highly similar genetic interaction profiles in the HAP1 network are enriched for gene pairs that also show high profile similarity in the global yeast genetic network. Gene pairs with high genetic interaction profile similarity were defined as those in the top 5% (light purple) or top 1% (dark purple) of gene pairs with the highest Pearson's correlation coefficient similarity values in the corresponding HAP1 and yeast networks.

(B) (i) Boxplot illustrating the distribution of genetic interaction profile similarity (PCC) of 4,847 yeast query genes with the HAP1 genetic interaction profile mapped for a *PTAR1* query cell line. The similarities of the human *PTAR1* genetic interaction profile with yeast *YKT6*, *BET2*, and *ECM9* query gene genetic interaction profiles are indicated. (ii) Graph of 4,847 yeast query genes plotted as a ranked order of the similarity (PCC) of their yeast genetic interaction profiles to that of human *PTAR1*. The top 5% of yeast query genes (~240) with the highest similarity to the *PTAR1* genetic interaction profile were enriched for the indicated GO bioprocess term (hypergeometric test, Benjamini-Hochberg corrected).

(C) Yeast-two hybrid analysis illustrating the physical interaction between α and β subunits of the indicated prenyltransferases. Two-hybrid analysis showed that yeast Ecm9 interacted specifically with yeast Bet2.

(D) Dual expression of human *PTAR1* and *RABGGTB* complemented the lethality of an *ecm9Δ* deletion allele. Tetrad analysis showing that co-expression of the human *PTAR1-RABGGTB* GGTase-III complements the essentiality of yeast *ECM9*. Yeast *ECM9*/*ecm9*Δ heterozygous deletion strains carrying a vector control or a plasmid expressing human *PTAR1* and *RABGGTB* expressed from a bidirectional galactose-inducible promoter were sporulated. The meiotic progeny derived from four tetrads were dissected and tested for spore germination (denoted a–d) on either glucose (Glu.) medium, where the promoter is repressed, or galactose medium (Gal.), where the promoter is induced. Black circles indicate spore progeny that are predicted to carry the *ecm9*Δ deletion. Blue circles indicate *ecm9Δ* deletion mutants where the *ECM9* essential phenotype is rescued by galactose-inducible expression of the human *PTAR1-RABGGTB* GGTase-III (bold).

(E) (i) GO biological process terms enriched among human genes that show a negative interaction with a *PTAR1* query gene and (ii) yeast genes that show a negative interaction with an *ECM9* query gene. (iii) *PTAR1* and *ECM9* negative interactions are both enriched for genes annotated to the GO bioprocess term, vesicle organization.

(F) (i) Bar graph illustrating enrichment for negative (blue) and positive (yellow) interactions with yeast *ECM9* among conserved gene pairs that showed a negative or positive genetic interaction with human *PTAR1*. Negative interactions with human *PTAR1* were significantly enriched for genes with conserved orthologs that showed negative interactions with yeast *ECM9*, relative to all other conserved gene pairs that were tested for interactions and did not show a negative interaction with *PTAR1* (gray bar). Positive interactions with *PTAR1* were not significantly enriched for positive interactions with yeast *ECM9* (gray bar). (ii) Bar graph showing enrichment for negative (blue) and positive (yellow) interactions with human *PTAR1* among conserved gene pairs that showed a negative or positive genetic interaction with yeast *ECM9*. Negative interactions with yeast *ECM9* were significantly enriched for negative interactions with human *PTAR1*, but positive interactions with yeast *ECM9* showed no significant enrichment with human *PTAR1*. In all cases, significance of enrichment was assessed using Fisher's exact test.

(G) Serial dilution growth assays of a yeast *ecm9Δ abh1Δ* double mutant carrying the indicated galactose-inducible gene expression plasmid in glucose- (repressive condition) or galactose (inducible condition)-containing medium. The ability of each galactose-inducible gene to rescue the loss of *ABH1* and restore the lethal phenotype of an *ecm9Δ* deletion mutant is shown.

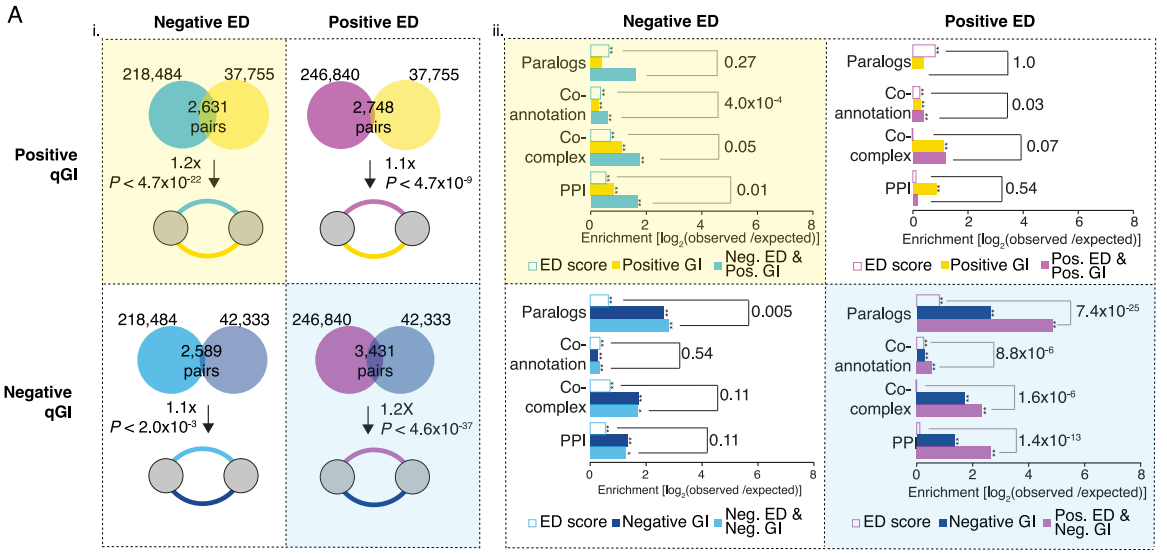

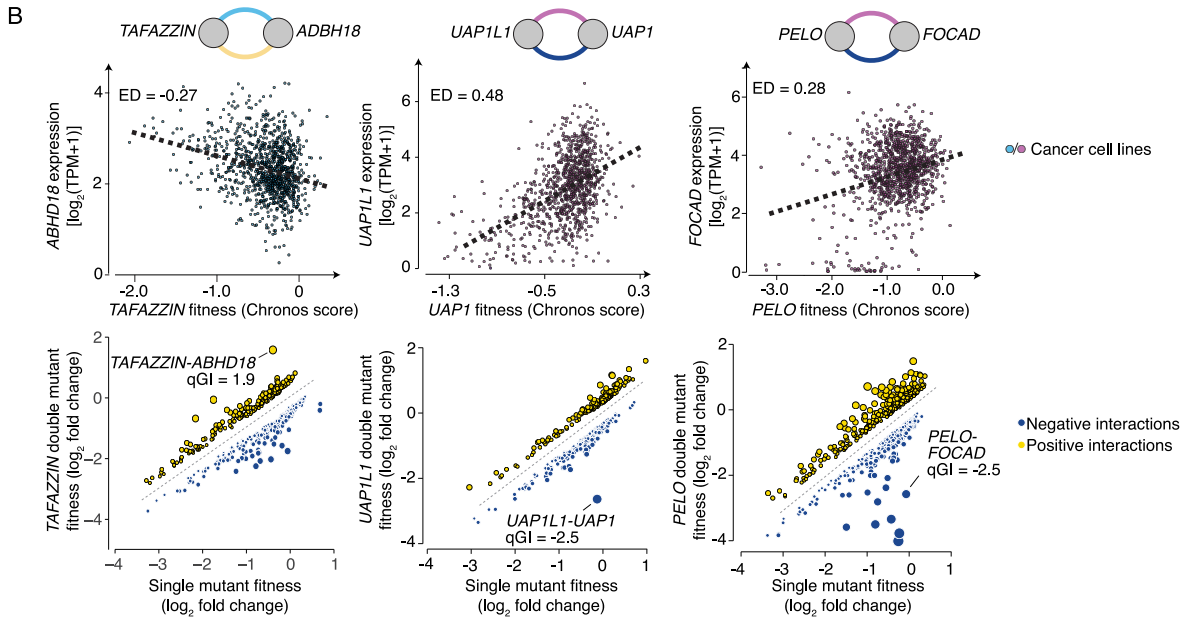

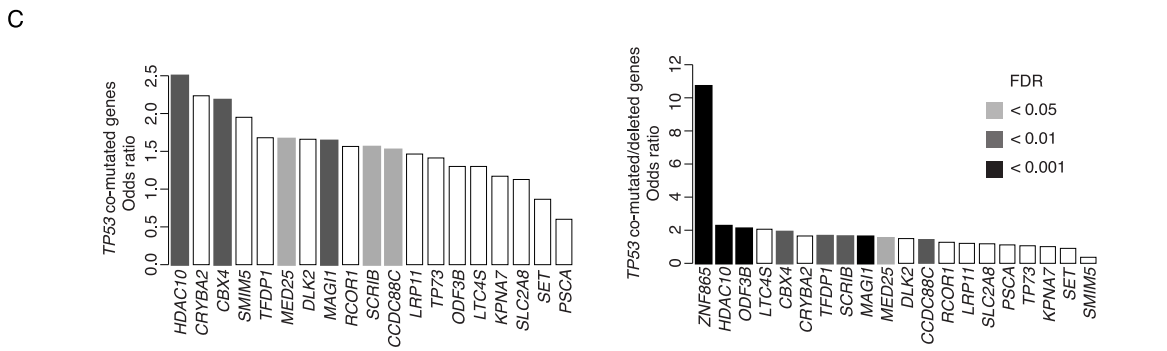

(legend on next page)

Figure S20. A relationship between ED in cancer cell lines and HAP1 genetic interactions, related to Figure 6

(A) (i) Overlap of gene pairs associated with all possible ED and qGI score combinations. (ii) Enrichment for indicated functional standards among gene pairs showing specific combinations of significant ED and qGI scores (hypergeometric test). Shaded regions indicate that gene pairs with a negative ED and positive qGI (yellow), or a positive ED and a negative qGI (blue), score combinations that share the most significant gene pair overlap.

(B) Scatterplots illustrating the relationship between *TAFFAZIN* single mutant fitness and *ABHD18* expression, *UAP1* single mutant fitness and *UAP1L1* expression, and *PELO* single mutant fitness and *FOCAD* expression, across a panel of DepMap cancer cell lines (22Q4). Regression lines (black dashed lines) indicate either a negative ED score and a positive genetic interaction score (qGI) or a positive ED score and a negative qGI score. Scatterplots illustrating significant negative and positive genetic interactions ($|qGI| > 0.3$, FDR < 0.1) for *TAFFAZIN*, *UAP1L1*, and *PELO* query genes. *TAFFAZIN-ABDH18*, *UAP1L-UAP1*, and *PELO-FOCAD* genetic interactions and qGI scores are indicated.

(C) TCGA Pan-cancer analysis of co-occurring mutations with TP53. Genes with positive interactions with TP53 and significant ED scores were evaluated for enrichment for co-occurring mutations across all tumor types in TCGA. The odds ratio reflects enrichment in co-occurrence. The left bar plot shows results based on predicted damaging mutations. The right bar plot shows results of both damaging mutations and deletion events. Shading indicates statistical significance (FDR) as tested by a Fisher exact test with Benjamini-Hochberg multiple hypothesis correction.

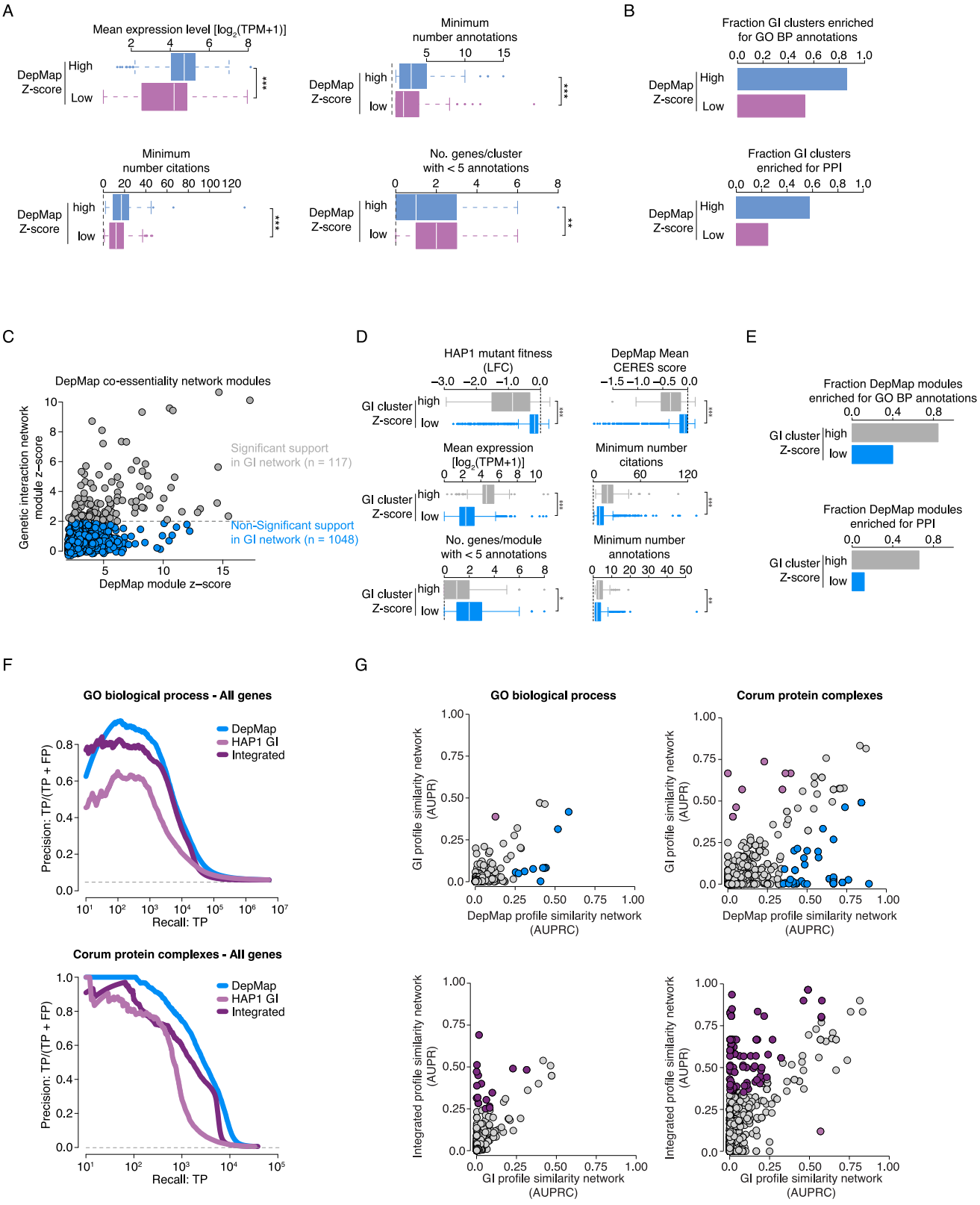

(legend on next page)

Figure S21. An integrated functional network based on genetic interaction and co-essentiality profiles, related to Figure 7

(A) Boxplots showing the relationship between features and genes in significant clusters or modules derived from the genetic interaction profile similarity network that either show highly correlated DepMap co-essentiality profiles (blue bars) or do not show highly correlated co-essentiality profiles (purple bars). ***$p < 10^{-3}$, **$p < 10^{-2}$ (Wilcoxon rank-sum test).

(B) Enrichment for GO biological process co-annotation and PPIs among genes that belong to the same genetic network-derived clusters that are also supported by modules derived from the DepMap co-essentiality network (blue bars) or among genes that cluster together to form modules based on similar genetic interaction profiles alone (purple bars).

(C) Scatterplot of *Z* scores associated with gene modules identified from the complete DepMap co-essentiality network. Modules with significant genetic interaction profile similarity in HAP1 are shown in gray, while those without significant similarity are blue. The gray dotted line indicates the *Z* score threshold for significant genetic interaction profile similarity.

(D) Boxplots showing the relationship with indicated features belonging to significant modules derived from the DepMap co-essentiality network that share similar genetic interaction profiles (gray bars) or that do not have strongly correlated genetic interaction profiles (blue bars). ***$p < 10^{-19}$, **$p < 10-5$, *$p < 10^{-3}$ (Wilcoxon rank-sum test).

(E) Bar plot illustrating the fraction of DepMap co-essentiality gene clusters whose members are enriched for GO-BP terms or PPIs. The fractions of enriched clusters uniquely identified in the DepMap co-essentiality network (blue bars) or DepMap-derived clusters comprising genes that also share highly similar genetic interaction profiles (gray bars) are shown.

(F) Precision-recall plots for genes with similar DepMap co-essentiality profiles (blue), genetic interaction profiles (light purple), or integrated profiles (dark purple). TP involves gene pairs co-annotated to a gold standard set of GO-BP terms (top panel) or CORUM complexes (bottom panel). Gray dashed lines represent background co-annotation rates. All genes, including those with mitochondrial-related functions, were included in the analyses. The performance of DepMap co-essentiality profiles (blue) is predominantly driven by profile similarity between mitochondrial genes.[26] Exclusion of genes with mitochondrial-related functions, as shown in Figure 7F and elsewhere,[26] results in decreased precision-recall of DepMap co-essentiality profiles, indicating that these mitochondrial gene relationships remain a dominant signal in this analysis.

(G) Comparison of individual GO-BPs or CORUM protein complexes captured by DepMAP (blue nodes), the genetic interaction profile similarity network (light purple nodes), or the integrated network (dark purple nodes). Nodes represent the genes annotated to a specific GO-BP term or CORUM complexes. Axes show AUPRC values (see STAR Methods). The diagonal indicates equivalent performance (gray nodes). Colored nodes above or below the diagonal represent GO-BP terms and CORUM complexes whose members show stronger profile similarity and thus cluster together more tightly in the indicated network.

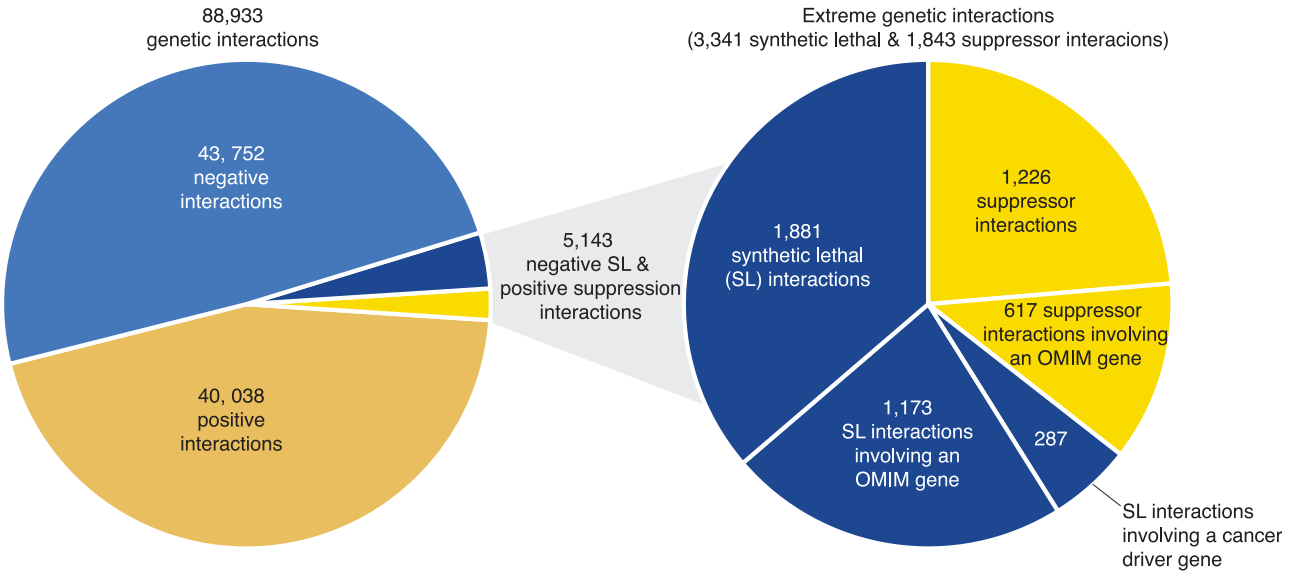

Figure S22. Extreme negative synthetic lethal and positive suppression interactions, related to STAR Methods

Summary of total negative and positive genetic interactions identified in this study and the subset of extreme synthetic lethal or genetic suppression interactions. Negative interaction portions are labeled in blue, and positive interaction portions are labeled in yellow, with the subset of extreme negative synthetic lethal interactions labeled in dark blue, and positive suppression interactions labeled in dark yellow. Extreme genetic interactions are further broken down (right pie chart) based on overlap with Mendelian disease genes (as identified in the OMIM database) or with characterized cancer driver genes (i.e., tumor suppressor genes).[119] Extreme synthetic lethal interactions correspond to HAP1-expressed, nonessential gene pairs with a negative genetic interaction (qGI < -0.6, FDR < 0.01) where the single mutant fitness of the library gene (LFC) was > -0.5 and the corresponding double-mutant fitness was < -1.0. Suppressor interactions were defined as gene pairs with a suppressor score > 0.5.